Interpreting air mass and precipitation structures from a weather-climate interface perspective: Analyses and projections

Melissa Gervais

Department of Atmospheric and Oceanic Sciences

McGill University

Montreal, Quebec

August 2015

A thesis submitted to McGill University in partial fulfillment of the requirements of the degree of Doctor of Philosophy

©Melissa Gervais 2015

ACKNOWLEDGEMENTS

A Ph.D. is a long process and there are many people who helped me get to where I am today. I would like to thank my two advisors Dr. Bruno Tremblay and Dr. John Gyakum. Bruno, thank you for teaching me to always think critically, be creative, and to look at the big picture. John, thank you for imparting you synoptic wisdom, for always challenging me, and for always supporting me.

Special thanks to Dr. Eyad Atallah for your patient advice. For teaching me synoptics and then over the course of the years helping me to apply it throughout my research. Most importantly, thank you for being my friend and sounding board.

I have been fortunate to have many fruitful discussions with various scientists throughout my Ph.D. For this I would like to thank Dr. Jaime Palter, Dr. Camille Lee, Dr. Ramon De Elia, Dr. William Gutowski, and Dr. Mike Pritchard. I would also like to thank Dr. Richard B. Neale for agreeing to be a last minute addition to Chapter 3 and providing his insights into the convective timing issue. Thanks to Line Bourdages for discussion about Arctic temperature inversions and for help with the abstract translation. I would also like to thank Michael Havas for providing invaluable technical support over the years.

Thanks to all my friends and colleagues at McGill. I have been so lucky to meet such amazing scientists and people throughout my time at McGill. I was also very fortunate to be part of two great research groups, synoptics and sea ice. I've learned so much being apart of both of these groups over the years.

Thank you to my parents, Gerry and Julie Gervais, for supporting me all of these years. Last but not least, thanks to my husband Kevin Bowley, for all the scientific discussions, the late studying, the many rounds of edits, and the endless moral support. You have been an instrumental part of my happiness and my accomplishments.

Throughout my doctorate, I have received financial support from numerous organizations. Fonds de Recherche en Science du Climat (FRSCO) from the Ouranos Consortium, the Natural Sciences and Engineering Council (NSERC) Discovery Foundation, Québec-Océan, the Canadian Sea Ice and Snow Evolution (CanSISE) Network, which is funded by the NSERC Climate Change and Atmospheric Research program, and the Canadian Network for Regional Climate and Weather Prediction. Thank you to all of these organizations for making this research possible.

This generation of this thesis also relied on numerous data sources and their providers. The NOAA Climate Prediction Center (CPC) made the UPD dataset available. The National Land and Water Information Service, Agriculture and Agri-Food, Canada, provided the GCDC dataset. The NASA/Goddard Space Flight Center's Laboratory developed the GPCP dataset as part of the GEWEX Global Precipitation Climatology Project. The NCAR Computational Information Systems Laboratory provided access to the CFSR data. The NCAR also provided access to CCSM data through the Earth System grid and produced the CESM1(CAM5) Large Ensemble Community Project with supercomputing resources provided by NSF/CISL/Yellowstone.

CONTRIBUTION OF AUTHORS

Chapters 2 and 3 are in the form of published articles, and Chapter 4 is in preparation for submission to the peer-reviewed Journal of Climate. I conducted the research and wrote the manuscripts of all three papers, as part of my Ph. D. studies. Prof. Bruno Tremblay and Prof. John Gyakum, provided supervision of the research and edited all manuscripts. Dr. Eyad Atallah also provided research guidance and editing throughout my doctorate. For Chapter 3, Dr. Richard Neale provided figure 3.10 and aided with the discussion surrounding the figure.

STATEMENT OF ORIGINALITY

The following elements of the thesis show original scholarship and represent distinct contributions to knowledge:

- The design and implementation of a station density experiment that produced an envelope of representative errors in median and extreme precipitation incurred due to station density. This was conducted for precipitation stations that were objectively analyzed to a 0.25° resolution grid as well as those subsequently remapped onto an approximately 1°grid. Error envelopes are published in Tables 2.1 and 2.2 allowing readers to apply the results to their own datasets.
- The conceptualization of two frameworks to describe how station density impacts representativeness errors. These were applied to understand the structure of the relationship between errors and station density, and how this changes by location and season.
- The application of the above conceptual frameworks and the theory of randomly correlated variables to explain discrepancies between previous studies. In particular, Kursinski and Zeng (2006) and Osborn and Hulme (1997), versus Hofstra and New (2009).
- I created the North American Amalgamated Precipitation (NAAP) through re-interpolation of a Canadian gridded station product, the 10km Gridded Climate Datasets for Canada, and merging it with the Unified Precipitation Dataset from the United States. This daily precipitation analysis is used in Chapter 3 and can be distributed to interested parties.
- The validation of precipitation in the Community Climate System Model (CCSM) examining the full distribution including extremes. Furthermore, comparisons

against a variety of different reference products demonstrated that in several locations the model produces accurate distributions within reference product error.

- The novel manner in which self-organizing maps, a relatively new methodology to the field of climate study, was applied to the Community Earth System Model - Large Ensemble provides an exciting new way to examine internal variability changes in the future.
- The results of Chapter 4 indicate how the frequency of occurrence of archetypal patterns of air masses are predicted to change in the future. This provides important information on how the weather society will experience will change, in addition to the average climatological change.
- The two physical mechanisms proposed by which climatological changes in surface forcing may be influencing the frequency of archetypal patterns. The first being related to changes in sea ice over the western Arctic and the second related to a warming deficit in sea surface temperature over the North Atlantic.

ABSTRACT

Future Arctic air masses are likely to be altered by Arctic amplification of tropospheric warming and the declining sea ice exposing large regions of open water. These changes are expected to alter mass fields across the Northern Hemisphere and be accompanied by changes climatological storm tracks and precipitation distributions. In order to quantify future changes in precipitation, we must first understand how well precipitation variability is captured both in observations and in global climate models (GCM). An experiment is conducted to quantify the representativeness errors, the errors incurred while upscaling station precipitation measurements to a gridded product that can be employed for GCM validation. Error ranges for both median and extreme precipitation are computed by repeatedly gridding station data with subsequently fewer stations for regions in the United States. The representation of the full distribution of precipitation intensity in the Community Climate System Model (CCSM4) over the contiguous United States and southern Canada, is investigated through comparison to several observational and reanalysis reference datasets. The skewness in the precipitation intensity distributions, relative to the reference datasets, varies regionally. In particular, we found a systematic bias toward lighter precipitation occurring in the Great Plains and eastern United States in the model. The bias is towards heavier precipitation however over the Rocky Mountains and the western United States. We find that model errors in extreme precipitation are approaching the magnitude of the disparity between the reference products, likely both a reflection of both strong model performance and the existence of significant bias in some commonly used reference products.

To investigate how Arctic air masses will change across the 21^{st} century, we employ the Community Earth System model large ensemble to explore how patterns in

January-February equivalent potential temperature at 850hPa (θ_{e850}) will change. To separate change in the mean from internal variability, the large number of ensemble members is leveraged to create an anomaly θ_{e850} field computed as the daily θ_{e850} values minus the yearly January-February ensemble average. A technique of self-organizing maps is applied to the daily equivalent potential temperatures anomalies at 850hPa, producing a set of archetypes of air mass patterns across the 21^{st} century. The frequency of occurrence of each archetype changes through the period of study, where most notably there is a statistically significant decline in a pattern with low θ_{e850} over the central Arctic. This pattern, when compared with a decadal average, has a more zonal circulation at 500hPa and higher sea ice concentrations over the peripheral Arctic seas. There is also a significant increase in the frequency of patterns with both higher and lower θ_{e850} over North America, associated with an enhanced meridional circulation at 500hPa. These changes in the internal variability of air masses and of the general circulation will likely alter the climatological distribution of precipitation amongst other impactful atmospheric phenomena.

ABRÉGÉ

Les masses d'air arctiques sont susceptibles d'être modifiées par le phénomène d'Amplification Arctique et à la diminution de la glace de mer qui exposera de grandes régions d'eau libre dans le futur. Ces changements devraient modifier les champs de masse à travers l'Hémisphère Nord, résultant en des changements possibles à la trajectoire climatologique des tempêtes et à la distribution des précipitations. Afin de quantifier les changements dans les précipitations, nous devons d'abord comprendre comment la variabilité des précipitations est représentée à la fois dans les observations et les Modèles de Climat Globaux (MCG). Une expérience est menée pour quantifier les erreurs de représentativité, qui résultent de la conversion des mesures de précipitations aux stations en un produit quadrillé pouvant être utilisé pour la validation d'un MCG. Les plages d'erreur des précipitations médianes et extrêmes sont calculées en réduisant à répétition la densité des stations utilisées pour des régions aux États-Unis. La représentation de la distribution complète de l'intensité des précipitations dans le Community Climate System Model 4 (CCSM4) est étudiée sur la partie continentale des États-Unis et le sud du Canada, par comparaison avec plusieurs observations et produits de réanalyse. L'asymétrie dans les distributions de l'intensité des précipitations, par rapport aux ensembles de données de référence, varie selon les régions. En particulier, nous avons trouvé un biais systématique dans le modèle vers des précipitations plus faibles dans les Grandes Plaines et dans l'est des, mais le biais va vers les précipitations fortes dans les Montagnes Rocky et l'ouest des États-Unis. Cependant, nous constatons que les erreurs de modélisation des précipitations extrêmes sont d'amplitude similaires aux différences entre les produits de référence, ce qui peut être à la fois dû à une bonne performance du modèle ou à l'existence d'un biais important dans certains des produits de référence couramment utilisés.

Pour étudier les changements projetés pour les masses d'air arctiques à travers le 21$^{\text{ieme}}$ siècle, nous explorons les changements de patrons de température potentielle équivalente à 850hPa en Janvier-Février (θ_{e850}), modélisés par le Community Earth System Model Large Ensemble (CESM-LE). Les contributions du changement du à la moyenne et à la variabilité interne peuvent être isolées en soustrayant la moyenne d'ensemble aux données de précipitations quotidiennes pour créer un champ d'anomalie de θ_{e850}. Une technique de cartes auto-organisationnelles est appliquée à ce champ d'anomalie, produisant un ensemble d'archétypes de patrons de masse d'air arctique dans le 21$^{\text{ieme}}$ siècle. La fréquence d'apparition de chaque archétype change pendant la période d'étude. Notamment, nous notons une déclin statistiquement significatif dans un archétype à faible θ_{e850} au centre de l'Arctique. Cet archétype, en comparaison avec une moyenne décennale, a une circulation plus zonale à 500hPa. Nous notons aussi une augmentation significative de la fréquence des patrons ayant des valeurs de θ_{e850} élevées ou faibles en l'Amérique du Nord, patrons associés à une circulation méridienne à 500hPa plus forte. C'est changement dans la variabilité interne des masses d'air arctiques et de la circulation général pourrait modifier la distribution climatologique de précipitations, entre autres phénomènes atmosphériques d'importance.

Contents

List of Tables

List of Figures

Chapter 1

Introduction

1.1 Background

The weather-climate interface referred to in the title could have a variety of meanings. In this thesis, it is meant to highlight that climate is not just an average state but rather consists of daily sensible weather. For example, simultaneous increases in extreme precipitation and drought with climate change could have a significant impact on society and yet register as very little mean climatological change. To understand the impacts of climate change on society, we need to understand how the underlying weather will change. This question includes ensuring that the global climate models (GCMs) used to study climate change are able to represent sensible weather, as well as investigating the changes they predict.

Global climate change is expected to have wide societal consequences in terms of changes in sensible weather. Large changes in the hydrological cycle are expected with generally fewer light and more heavy precipitation events, increased drought, and more intense extreme precipitation (Trenberth et al., 2003; Sun et al., 2007). These impacts can already be seen in observations and reanalysis products of the historical period (Groisman et al., 2005; Shiu et al., 2012). Results from the Intergovernmental Panel on Climate Change (IPCC) Fifth assessment report, predict an average increase in global surface temperature between 1.0-3.7°C by the end of the 21st century, depending on the emission scenario chosen (Collins et al., 2013) (Fig. 1.1).

Future predictions of precipitation can be difficult to trust because precipitation has been a historically difficult variable for models to predict (Dai et al., 1999; Iorio et al., 2004; Sun et al., 2006). GCMs tend to produce too much light and too little heavy precipitation, even in models that reproduce the mean precipitation well (Chen et al., 1996; DeMott et al., 2007). Precipitation is also sensitive to errors in the representation of the large-scale flow, mid-latitude and tropical storms, and topography. Model orography tends to be simplified due to resolution constraints resulting in errors in the simulation of orographic precipitation (Gent et al., 2010; Iorio et al., 2004). In addition, there are many sub-grid scale processes involved in the generation of precipitation that must be parameterized. This is of particular importance for convective precipitation, which tends to occur too frequently and at too low an intensity owing to issues with the build up of convective available potential energy (Dai and Trenberth, 2004; DeMott et al., 2007). Furthermore, propagating mesoscale convective systems, which often result in extreme precipitation events, are difficult for GCMs to replicate (Pritchard et al., 2011; Dirmeyer et al., 2012). These issues are of particular relevance for the distributions of precipitation and extreme precipitation values. The newest generation of GCMs have undergone many improvements both in term of parameterizations and resolution. Validation of these new model versions within the historical period provides an indication of their ability to predict future changes.

There are several globally available reference products that are used to validate model precipitation. The global precipitation climatology product (GPCP) produces a pentad precipitation product that merges station observations and satellite precipitation (Xie et al., 2003). For daily analysis however, there is only one satellite product that is available globally, the GPCP 1DD (Huffman et al., 2001). This is produced without any merging with station observations, using satellite estimates of cloud top temperatures to infer precipitation occurrence (Huffman et al., 2001). Reanalysis products such as the National Centers for Environmental Prediction (NCEP) Climate Forecast System Reanalysis (CFSR) (Saha et al., 2010) assimilate meteorological variables and produce precipitation using a regional climate model. These two types of products are often employed as observations to conduct GCM model validation of precipitation, although they themselves may have large biases.

Direct measurements of precipitation are conducted using rain and snow gauges (Adam and Lettenmaier, 2003), which especially for snow gauges can have large measurement biases (Goodison et al., 1998). These measurements are taken at a point locations, but for model validation must be compared against the gridded climate model output (Chen et al., 2008). During the gridding process many errors may be introduced, known as representativeness errors (Tustison et al., 2001). The density of observations can also have a large impact on gridded station analyses (Osborn and Hulme, 1997; Kursinski and Zeng, 2006; Hofstra et al., 2010; Chen et al., 2008), since precipitation is discontinuous and can be very small in length scale (Hewitson and Crane, 2005). As a result, model precipitation validation using station observations should be conducted in regions with dense gauge networks. This is particularly problematic as there are few regions of the world where these station observations networks are very dense. Furthermore, station measurements are only available over the continents resulting in expansive ocean regions without station measurements. In the validation of GCM precipitation it is important to consider where the GCM fits in the span of observational and reanalysis product errors.

In contrast to precipitation, temperature is more spatially uniform and thus easier to represent in observations and models. The most prominent feature in the pattern of future temperature change is a larger increase in temperatures over the Arctic than the midlatitudes, known as Arctic amplification (Kay et al., 2012). In the most aggressive IPCC scenario, the projected increase in Arctic temperature in an ensemble of GCMs is 8.3°C compared to the global average of 3.7°C (Collins et al., 2013). Such changes are already being exhibited in the observations (Serreze et al., 2009). The enhanced heating is greatest at the surface and reduces with height in the troposphere (Serreze et al., 2009).

Arctic amplification is produced by positive feedbacks, such as the lapse rate and sea ice albedo feedbacks (Pithan and Mauritsen, 2014; Graversen et al., 2014). Graversen et al. (2014) found that these two feedbacks cannot be considered to be fully independent of one another. The temperature structure of the atmosphere overlying the Arctic sea ice and snow covered landmass area, is that of a strong temperature inversion (Curry, 1983). The stability associated with the temperature inversion confines the Arctic warming to lower levels, as opposed to the tropics where convection allows this warming to penetrate higher up in the atmosphere (Manabe and Wetherald, 1975). In the Arctic, a greater surface warming is thus necessary to balance the top of the atmosphere radiation changes owing to global climate change, resulting in a positive lapse rate feedback (Pithan and Mauritsen, 2014).

In the sea ice albedo feedback, a reduction in sea ice leads to an increase in open ocean with a lower surface albedo and an increase in the absorption of incoming solar radiation (Manabe and Wetherald, 1975). The increased storage of heat in the ocean leads to a delay in the onset of ice formation in the fall, thus completing the positive feedback loop. Arctic sea ice has been steadily declining, with projections of summer ice free conditions by the mid-21st century (Collins et al., 2013; Wang and Overland, 2012). The decline is occurring throughout the entire year, with the greatest losses occurring in the fall (Fig. 1.2). The area of winter sea ice loss is smaller, however owing to the higher temperature contrasts and thus increased heat flux from the ocean to the atmosphere, the impact of the atmosphere is greater in this season (Deser et al., 2010; Singarayer et al., 2006).

The decrease in meridional temperature gradient associated with Arctic amplification and declining sea ice may lead to changes in the location and intensity of storm tracks and the mid-latitude jet stream. Some studies suggest that sea ice loss has already induced changes in the mid-latitude circulation (Francis and Vavrus, 2012; Liu et al., 2012), however whether observed changes can be detected or attributed to sea ice loss is debatable (Barnes, 2013; Screen et al., 2013). This has become the subject of a growing body of research, which has been summarized by Cohen et al. (2014).

Future climate change studies with more significant sea ice loss are more likely to identify potential sea ice impacts on the atmosphere. There have been several studies examining the impact of future sea ice loss on the atmosphere using atmosphere only experiments with prescribed sea ice and sea surface temperatures (Honda et al., 1999; Deser et al., 2004; Alexander et al., 2004; Magnusdottir et al., 2004; Singarayer et al., 2006; Seierstad and Bader, 2008). The impact of winter sea ice loss in these studies is dependent on the region and extent of the sea ice loss. In general, studies that prescribed sea ice loss in the Sea of Okhotsk produced a Rossby wave response with impacts stretching across North America (Honda et al., 1999; Alexander et al., 2004). Deser et al. (2004) decomposed the impact of sea ice loss in the north Atlantic into a direct response consisting of Rossby wave development over the sea ice anomaly and an indirect response that projects onto the North Atlantic Oscillation. Other studies with prescribed sea ice loss in the North Atlantic, exhibited responses that fell into one of these two categories (Alexander et al., 2004; Magnusdottir et al., 2004; Singarayer et al., 2006; Seierstad and Bader, 2008).

Part of understanding changes in sensible weather owing to climate change involves separating forced and internal variability. There are many climate modes that operate on long timescales, such as the Pacific Decadal Oscillation and the Atlantic Multidecadal Oscillation, which can have large impacts on temperature and precipitation on a local scale (Deser et al., 2014). Separating the internal variability from the forced global warming response is highly important to the detection, attribution, and prediction of climate change. To study these issues, large ensemble prediction experiments have recently been produced, where a single model is used to generate a large number of realization with the same model physics (Kay et al., 2014). Deser et al. (2014) used a large ensemble of the Community Climate System Model 3 (CCSM3) and showed widely varying trends in North American surface air temperature and precipitation between ensemble members over a 51-year period. Deser et al. (2014) was able to leverage the ensemble size to separate trends due to internal and forced variability in each of the ensemble members. The introduction of such large repositories of climate model data presents a great opportunity for studying the underlying sensible weather of climate models and will require new and innovative approaches for climate studies.

1.2 Research Questions

The objective of this thesis is to understand air masses and precipitation within the context of climate change. There are three important aspects of modeling future climate that are studied in this thesis. The first is ensuring that observations are transformed appropriately for validation against global climate models and that these observations are adequate representations of reality. The second, is validating global climate models in the historical period with observations. Finally, investigations of future climate model predictions and the mechanisms responsible for these changes can be conducted.

This thesis addresses the most pertinent of these aspects of future climate modeling for either precipitation or air masses. There is also a focus on using novel methods or datasets in order to understand the higher-order variability, a part of viewing climate from a weather perspective. The structure of the remaining portions of the thesis are as follows:

- In Chapter 2 precipitation is studied across all seasons and over North America, where there is a high station density and thus confidence in the observations. The chapter addresses how to produce accurate representations of station data for comparison against global climate model output. Furthermore, a station density experiment is conducted to quantify errors in the representation of precipitation, resulting from limited gauge network density.

- In Chapter 3, a validation study of precipitation in a GCM compared to gridded gauge observations, reanalysis, and satellite products is conducted. The chapter focuses on how the full distribution of precipitation, including extreme, are represented in regions with differing climatologies. An emphasis is also placed on understanding some underlying causes of errors in the model representation of precipitation.

- Chapter 4 is focused on Arctic air masses in the winter, which are likely to experience large changes due to Arctic amplifications. A technique of self-organizing maps is used to identify patterns of air masses that occur throughout the 21st century and how they will change in the future, relative to the average climatic change. Surface forcing features and the mechanisms by which they may induce these changes in air mass patterns are also discussed.

- Chapter 5 provides a summary of the results presented in the thesis.

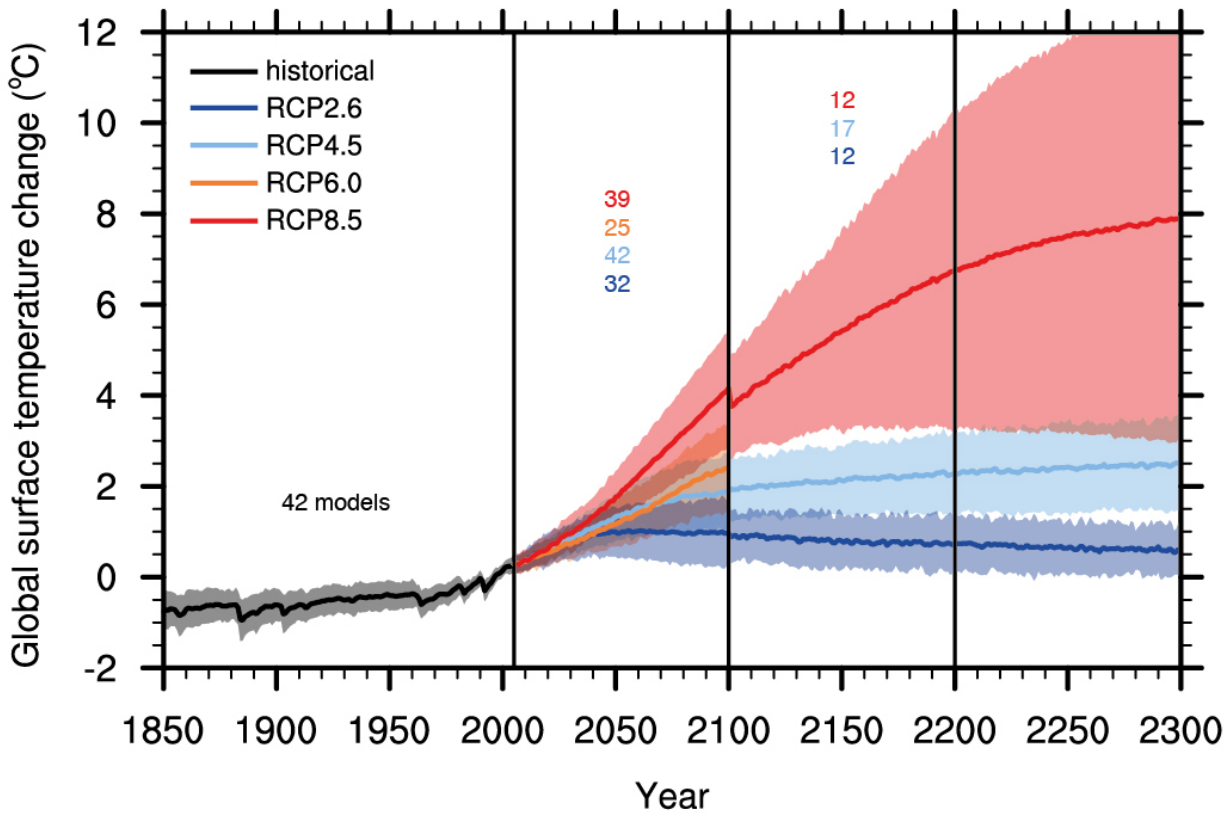

Figure 1.1: Time series of global annual mean surface air temperature anomalies (relative to 1986-2005) from CMIP5 concentration-driven experiments. Projections are shown for each RCP for the multi-model mean (solid lines) and the 5 to 95% range (±1.64 standard deviation) across the distribution of individual models (shading). Discontinuities at 2100 are due to different numbers of models performing the extension runs beyond the 21st century and have no physical meaning. Only one ensemble member is used from each model and numbers in the figure indicate the number of different models contributing to the different time periods. No ranges are given for the RCP6.0 projections beyond 2100 as only two models are available. Figure, including caption, from Collins et al. (2013), Fig. 12.5.

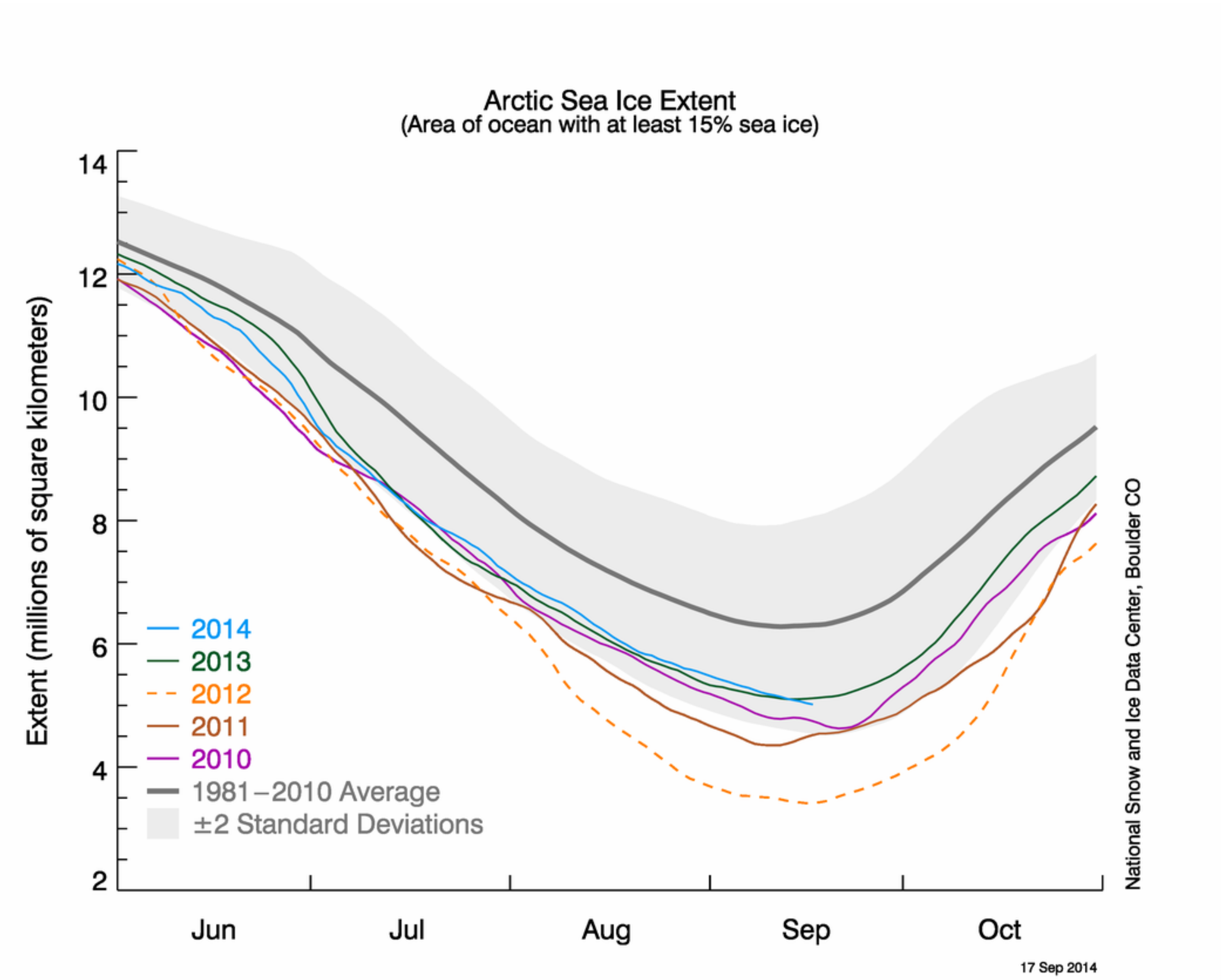

FIGURE 1.2: Arctic sea ice extent, with climatological average and individual and the past 5 individual years. The average from 1981-2010 is in dark gray with shading denoting ±2 standard deviations. Individual years are shown in purple for 2010, brown for 2011, orange for 2012, green for 2013, and blue for 2014 up until September 17$^{\text{th}}$. Credit: National Snow and Ice Data Center

Chapter 2

Representing Extremes in a Daily Gridded Precipitation Analysis

This chapter investigates the representation of precipitation in gridded observational data, specifically addressing the impacts of the methodology utilised to grid station measurements and the impact of station density of representativeness errors. This chapter consists of a paper published in the Journal of Climate: Gervais, M., L. B. Tremblay, J. R. Gyakum, and E. Atallah, 2014b: Representing Extremes in a Daily Gridded Precipitation Analysis over the United States: Impacts of Station Density, Resolution, and Gridding Methods. *Journal of Climate*, **27 (14)**, 5201–5218, doi: 10.1175/JCLI-D-13-00319.1.

Representing Extremes in a Daily Gridded Precipitation Analysis over the United States: Impacts of Station Density, Resolution, and Gridding Methods

Melissa Gervais, L. Bruno Tremblay, John R. Gyakum, and Eyad Atallah

Department of Atmospheric and Oceanic Science, McGill University, Montreal, Quebec

©American Meteorological Society. Used with permission.

The original publication is available at http://journals.ametsoc.org. The article is reproduced here with kind permission from the Journal of Climate: Gervais, M., L. B. Tremblay, J. R. Gyakum, and E. Atallah, 2014b: Representing Extremes in a Daily Gridded Precipitation Analysis over the United States: Impacts of Station Density, Resolution, and Gridding Methods. *Journal of Climate*, **27 (14)**, 5201–5218, doi: 10.1175/JCLI-D-13-00319.1.

Abstract

This study focuses on errors in extreme precipitation in gridded station products incurred during the upscaling of station measurements to a grid, referred to as representativeness errors. Gridded precipitation station analyses are valuable observational data sources with a wide variety of applications, including model validation. The representativeness errors associated with two gridding methods are presented, consistent with either a point or areal average interpretation of model output, and it is shown that they differ significantly (up to 30%). An experiment is conducted to determine the errors associated with station density, through repeated gridding of station data within the United States (US) using subsequently fewer stations. Two distinct error responses to reduced station density are found, which are attributed to differences in the spatial homogeneity of precipitation distributions. The error responses characterize the eastern and western US, which are more and less homogeneous respectively. As the station density decreases, the influence of stations further from the analysis point increases, and therefore if the distributions are inhomogeneous in space the analysis point is influenced by stations with very different precipitation distributions. Finally, ranges of potential percent representativeness errors of the median and extreme precipitation across the US are created for high resolution (0.25° lat-lon) and low resolution areal averaged (0.9x1.25° lat-lon) precipitation fields. For example, the range of the representativeness errors is estimated, for annual extreme precipitation, to be +16% to -12% in the low resolution data, when station density is 5 stations per 0.9x1.25° lat-lon grid box.

2.1 Introduction

The impact of climate change on precipitation is of great interest to society given the socio-economic implications of changes in the distribution of precipitation. It has been theorized that future increases in the Earth's temperature will result in a general change in the distribution of precipitation amounts towards fewer lighter precipitation events, more droughts, and more heavy precipitation events (Trenberth et al., 2003). This idea is supported by observations and reanalyses for the historical period (Groisman et al., 2005; Shiu et al., 2012), as well as in predictions of future climate using Global Climate Models (GCMs) (Groisman et al., 2005; Sun et al., 2007). The ability of GCMs to accurately predict future changes in precipitation is crucial for the development of measures associated with adaptation to climate change. Fundamental to the improvement of GCM prediction is the validation against observational data.

In order to conduct a fair comparison between simulated and observed precipitation, errors in the observed precipitation field must be quantified. When the observations consist of precipitation station data gridded to the model resolution, there are two main sources of error that must be considered: measurement error and representativeness error due to gridding (Tustison et al., 2001). Several studies have examined errors associated with precipitation gauge measurements, and found systematic biases in precipitation of the order of 10% for liquid precipitation (Adam and Lettenmaier, 2003) and one order of magnitude larger for solid precipitation (Goodison et al., 1998; Cherry et al., 2007). Representativeness error is defined by Tustison et al. (2001) as "the errors in representing data (i.e. either model output or observations) at a scale other than their own inherent scale". For gridded station data, the representativeness error can be impacted by the method of gridding employed and the density of stations.

The method used to grid precipitation station data depends on how GCM simulated precipitation is interpreted, whether it is considered as an areal average over a grid box or as a point estimate (Osborn and Hulme, 1997; Chen and Knutson, 2008a). If grid resolution is high relative to the scale of precipitation features, the two interpretations are identical. However, unlike many other climate variables, precipitation consists of small scale structures that are discontinuous in nature (Hewitson and Crane, 2005). This can result in significant difference between the areal average and point estimate interpretations, which leads to large differences in inferred precipitation statistics (e.g. median and extremes, Accadia et al., 2003; Chen and Knutson, 2008a). Specifically, Chen and Knutson (2008a) found that interpreting precipitation as an area average, resulted in generally lower extreme precipitation values and a higher number of wet days than the point value interpretation.

Furthermore, precipitation in GCMs is parameterized (i.e. not explicitly resolved). This parameterization represents smaller scale structures, such as updrafts and downdrafts, by a single area averaged output (Osborn and Hulme, 1997; Chen and Knutson, 2008a). We thus consider precipitation as an area averaged quantity over a model grid cell similar to previous modeling studies using regional climate models (RCM) and GCMs (Osborn and Hulme, 1997; Tustison et al., 2001; Hewitson and Crane, 2005; Chen and Knutson, 2008a; Gober et al., 2008; Hofstra et al., 2010).

When using station observations for model validation, the method employed to upscale the station data should reflect the consideration of model precipitation as an area average within a grid box. To this end, Hewitson and Crane (2005) and Chen and Knutson (2008a) recommend gridding station data to a higher resolution than the model grid using an objective analysis (OA), and subsequently using an area weighted averaging procedure to remap onto the model grid. The purpose of the OA is to create a set of regularly spaced point observations (Hewitson and Crane, 2005). This reduces the impact of irregular spacing of station observations, and may be necessary to bridge gaps between locations where the station density is low. These OAs are typically conducted using distance weighted methods, which inherently include some smoothing, even in regions with a high density of observations (Ensor and Robeson, 2008; Chen and Knutson, 2008a). The amount of smoothing that occurs during the OA stage generally affects extremes in precipitation more than the means (Ensor and Robeson, 2008; Hofstra et al., 2010). The area weighted averaging procedure takes the area of overlap between the high resolution OA grid boxes and the model grid box into account, while conducting the remapping. This results in further smoothing of precipitation, especially extreme events (Chen and Knutson, 2008a).

In addition to the method of gridding utilized, the density of station measurements can have a large effect on precipitation analyses. In a discussion by Daly (2006), various factors such as elevation, terrain induced climate transitions, and coastal zones are identified that may influence the ability of objective analysis schemes to accurately portray precipitation. They suggest that regions further than 100km from coastlines are easier to represent, whereas regions with significant coastal influence on precipitation or terrain features are more difficult for objective analyses. As such they would require lower or higher station densities respectively, to accurately represent precipitation.

The impacts of changing station density on gridded precipitation have been studied for different resolution and using different gridding methods (Osborn and Hulme, 1997; Kursinski and Zeng, 2006; Hofstra et al., 2010; Chen and Knutson, 2008b). Hofstra et al. (2010) examined the impact of reducing station density in regions over western Europe for a sample of 10 grid points. They first grid the data onto a higher resolution 0.1° lat-lon grid using an OA and then remap to a lower resolution, either a 0.22° or 0.44° grid. They conducted repeated gridding of station data for their selected grid points, with decreasing input stations and for many combinations of stations removed. They found that the variance and mean of precipitation typically decreased with reduced station density. Chen and Knutson (2008b) conduct an intercomparison of objective analyses of station data within the US onto a 0.5°lat-lon grid using several objective analysis methods. They also examine the impacts of reducing the percent of input stations employed in the analysis. They find an increase in errors in the aggregate statistics across the US, with decreased percent station inclusion, that is higher in the summer than the winter.

Osborn and Hulme (1997) and Kursinski and Zeng (2006) conducted similar studies but at a lower resolutions (ex. 2.5°lat-lon in Kursinski and Zeng, 2006) and using a simple average of stations within the grid box to compute the area average. Using this method, Osborn and Hulme (1997) found that the variance of daily precipitation in western Europe, China, and Zimbabwe increases with decreased input stations. Kursinski and Zeng (2006) used hourly station data in Ohio, and found similar results to Osborn and Hulme (1997). They observed that the average precipitation amount per hour varied more widely and with generally higher precipitation rates, as the number of input stations decreases. The reduction of station density in these studies thus had the opposite effect than in Hofstra et al. (2010), who conducted their study at both a different resolution and using a different gridding method. These studies leave open questions of how gridding method, resolution, and region of study could impact the relationship between precipitation statistics and station density.

The central purpose of this study is to provide a quantitative assessment of the representativeness errors associated with gridded station data, used in particular for the validation of GCMs. The United States (US) provides a useful test bed for such studies as it has a high density of stations and encompasses a wide range of climate regimes. Station data within the US is used to examine precipitation statistics at several scales, from point measurements, to OA high resolution grids, to area averaged low resolution grids. This repeats the experiment conducted by Chen and Knutson (2008a) but at a higher resolution for the area average grid, typical of the current generation of GCMs, and including the representativeness error during the transition from station to OA data. Furthermore, the impact of station density is assessed for both the high resolution OA and low resolution areal-average precipitation data. This is accomplished by conducting an experiment of successively gridding station data within the US with a decreasing number of input stations. The purpose of this experiment is to provide a measure of the potential representativeness errors due to station density. We will investigate how the relationship between station density and precipitation errors depends on seasonality, characteristics length scales of precipitation, and geographic location. The methodology in this study is specifically geared towards examining the representativeness errors in gridded precipitation data for the purpose of model validation, however the results may be used to understand the impact of gridding methods and station density for any application of OA or areal-averaged precipitation. In another study, we follow up on this work with an application of these results in a study on errors in the distribution and extremes of precipitation in a GCM (Gervais et al., 2014a).

2.2 Data

We use daily precipitation station data from the Global Historical Climatology Network - Daily version 1.0 (GHCN) dataset, from the National Climatic Data Center. This dataset consists of over 30,000 stations worldwide, recording temperature and precipitation.

Extensive quality control procedures have been applied to the data to address issues such as formatting, duplicate stations, and outliers (Menne et al., 2012), and no further quality controls are applied in this study. For our analysis, stations from the contiguous US are used (over 10,000 stations) over the time period of 1979-2003. The reporting times of each station vary depending on the data source (Menne et al., 2012). All stations are used regardless of their reporting rates in order to maximize the information ingested. On average, 41% of the total number of stations are reporting daily, where the percentage of time in which each station is reporting over the period of study is shown in Fig. 2.1.

2.3 Methodology

2.3.1 Station Decorrelation Lengths

The decorrelation length is used in this study to provide a measure of the length scale of precipitation processes. Specifically, it is defined as the distance at which the correlation between a given location and those at this distance away falls to $1/e$ (Osborn and Hulme, 1997). It is produced for each station by computing the distance and correlation with all other stations using a Kendall's Tau rank method, which is valid for non-normally distributed fields (Wilks, 2006). Following Osborn and Hulme (1997), an exponential of the form:

$$r = e^{-\frac{x}{x_0}}$$

is then fit to the correlation versus distance data for each station, where r is the interstation correlation, x is the distance between the stations, and x_0 is the decorrelation length. Maps of the decorrelation lengths of all stations are then created to demonstrate how the decorrelation length varies geographically.

2.3.2 Gridding Methods

The GHCN station data are first gridded to a 0.25° lat-lon grid. This grid is chosen to be consistent with the Climate Prediction Center's Daily Unified Precipitation Data (UPD) (Chen and Knutson, 2008b), a widely used gridded station precipitation product for the US created using a more sophisticate OA method. This high resolution gridded GHCN precipitation field (HRES) is constructed by conducting an OA on the GHCN station data using a three pass Cressman scheme (Cressman, 1959), with smaller radii of influence and successive corrections at each pass. The three radii of influence in the Cresmann scheme are 6, 3, 1.5 times the average minimum station distance or on average 120km, 60km, and 30km when all available stations are employed. This method was chosen over the optimal interpolation scheme used in the creation of the UPD in an effort to reduce computational costs. For reasons discussed in Section 3c the interpolation is conducted numerous times, so a more simple method is preferred. The Cressman scheme, however, is less accurate than the optimal interpolation method (Chen and Knutson, 2008b) and does not include orographic adjustments. Precipitation stations tend to be located at lower elevations and precipitation tends to increase with elevation. This typically results in a bias towards lower precipitation amounts in mountainous regions, and so many gridded gauge analyses conduct an orographic adjustment to account for this effect (ex. Xie et al., 2007; Hutchinson et al., 2009). The spatial patterns in precipitation statistics are similar between the HRES gridded precipitation and UPD datasets (not shown), implying that the Cressman OA scheme is adequate for our purposes.

The HRES data is used to create low resolution precipitation fields on a 0.9x1.25° lat-lon grid, a common resolution for current GCMs, consistent with the treatment of precipitation data for GCM validation. Two methods of transformation of the HRES data are utilized to be consistent with either the point or area average interpretation of precipitation. For the point interpretation, a simple bilinear interpolation is applied to the grid nodes of the HRES data to produce a low resolution product (LRES-interp). For the area average interpretation, the HRES data is remapped using the Spherical Coordinate Remapping and Interpolation Package (SCRIP) from the Los Alamos National Laboratory (Jones, 1999). SCRIP is a flux conserving method that computes weights for each input grid based on the area overlap between the input grid and the output grid. As discussed in the introduction, the area average interpretation of GCM precipitation is considered to be the most appropriate. The low resolution gridded GHCN precipitation created through remapping, which is hereafter called LRES, is thus considered the better product for GCM validation. A schematic diagram of the transformation of the data from station, to HRES, to LRES and LRES-interp products is shown in Fig. 2.2.

Following Chen and Knutson (2008a), precipitation statistics are computed after the OA and remapping procedures are applied. All statistics are calculated bimonthly and annually, then averaged over all years. The bimonthly periods used are January-February (JF), March-April (MA), May-June (MJ), July-August (JA), September-October (SO), and November-December (ND). We define precipitating days as those with >1mm day^{-1} of precipitation, consistent with the World Climate Research Programme/Climate Variability and Predictability (WCRP/CLIVAR) Expert Team on Climate Change Detection, Monitoring, and Indices (ETCCDMI) group. This value is arbitrary and is larger than the minimum detectability threshold of a rain gauge, however it is employed in many other studies (ex. in Dai, 2006; Sun et al., 2006; Chen and Knutson, 2008a). Some results using 0.25mm day^{-1} as the threshold to define precipitating days are discussed for comparison, however results are shown using the 1mm day^{-1} threshold unless otherwise specified. We compute the median and the 97^{th} percentile (herein referred to as extreme) of precipitating days as metrics of the non-gaussian distribution of precipitation.

2.3.3 Station Density Experiment

An experiment is conducted to determine the impact of reducing station density on the statistics of gridded precipitation products. The experiment consists of producing HRES and LRES fields for the entire time period (following the methodology in Section 3b) and calculating the statistics of these fields (median and extreme), using subsequently fewer input stations. The initial number of input stations is shown in Fig. 2.3. This reduction process is repeated 20 times, each successively removing a randomly chosen set of stations, amounting to 5% of the initial number of stations. Assuming the distribution of precipitation is well-represented during the first step of the experiment, utilizing 100% of the total stations, then any deviation from the initial value of a precipitation metric (median or extreme) during subsequent steps represents a climatological error in the precipitation metric resulting from a change in station density.

We are interested in characterizing the representativeness errors associated with a given station density. To this end, we represent the station density for the LRES data as simply the number of stations within the LRES grid box. For the HRES data however, the radii of influence of the OA is larger than HRES grid boxes, implying that stations outside of a grid box influence the analysis. Furthermore, a large portion of HRES grid boxes contain few or no input stations. Consequently, a larger area is chosen for the calculation of the HRES station density. We defined the HRES data density as the number of stations within a box of the same dimension as an LRES grid box (0.9°x1.25° lat-lon), but centered on the HRES grid points. Choosing the same area as the LRES density calculations allows for direct comparison between impacts of station density on the HRES and LRES fields. To take station reporting rates into consideration, the density of stations reporting each day are calculated, averaged over the time period of interest (bimonthly or annually), and then averaged climatologically.

Since station density is highly variable throughout the domain, the change in station density for each percent removal step varies considerably across the US. Therefore, results are presented as a function of the station density at each grid box, as opposed to the percentage of stations removed. This allows for the association of climatological errors at a given removal step, for all grid points, with their station density.

In studies on the impact of reduced station density on gridded precipitation, Osborn and Hulme (1997); Kursinski and Zeng (2006); Hofstra and New (2009) found that errors are dependent on the combination of stations removed, in other words, there is a spread in the distribution of errors when various combinations of station removals are conducted. Unlike these studies who conducted station density experiments within a small sample of grid boxes, our study is conducted using an OA technique over a large domain. This method is more computationally intensive, and therefore the experiment here is not repeated for the many possible combinations of station removals, as done in Osborn and Hulme (1997); Kursinski and Zeng (2006); Hofstra and New (2009). Instead, we define the percent climatological errors of each grid point as the percent difference between the initial value of a precipitation metric and the value at subsequent steps. This normalized measure of climatological error allows for the inter-comparison of grid boxes across a region, which is used to create a distribution of errors analogous to one produced when varying combinations of stations removed are compared. This method implicitly assumes that error structures are similar between grid boxes, which is not necessarily true. However, if we are concerned with a general definition of climatological errors that can be applied to the entire domain, then it is advantageous to take into account all of the potential error responses within a given region.

Distributions of errors with respect to station density are produced by employing all grid boxes within the US, or different sub-regions of the US, to create scatter plots of percent climatological error. This is repeated for the median and extreme precipitation, the LRES and the HRES datasets, and for different periods. The domain was separated into regions with similar precipitation climatologies (Fig. 2.4), assuming that the dependence of the errors on station removal is similar within a climatological region. Climatological errors are included for all grid points regardless of the initial station density to maximize the information that is being ingested and to avoid biasing the results to more populated regions. The concentration of computed climatological percent error points is represented by coloring each error point to correspond to the number of points occurring within 1% error bins. There is a high density of points at 0% climatological error, even at low station density; this is due to grid boxes with lower station density being normalized, and then only accruing errors slowly with further removal of stations. This could also imply that in regions with low station density, such as the Rockies, the climatological percent errors may be underestimated. Upper and lower bounds on the climatological percent error for the US are defined by exponential curves of the form:

$$y = ae^{bx} + ce^{dx}$$

fitted to the 99^{th} and 1^{st} percentiles of the error distribution. These percentiles and fits were chosen to best represent the outer limits of the climatological error distribution, while also excluding outliers. The coefficient of determination (R^2) of these fits are very high (typically R^2 >0.9), supporting the use of the exponential fit.

2.4 Results

2.4.1 Impacts of Gridding on Precipitation Statistics

In this section, we investigate how the gridding of station data onto a high resolution grid and remapping onto a lower resolution grid (typical of a GCM) alters the statistics of precipitation. In addition, we quantify the impact of interpreting model precipitation as an area average versus a point estimate. This is accomplished through the inter-comparison of the median and extreme precipitation of GHCN data in various forms, from original station data through to various gridded products (HRES, LRES-interp, and LRES).

Annual station precipitation climatologies show a wide range of median (4-15mm day^{-1}) and extreme (25-80mm day^{-1}) values across the US (Fig. 2.5 a-b). Regions with heavy precipitation are present along the West Coast as well as in the Cascade and Sierra Nevada mountain ranges. In the Rocky Mountains lower median and extreme precipitation are recorded. A large area of high precipitation in the South-East US and the Eastern Seaboard is seen in both the median and extreme precipitation. There is a defined region of high precipitation East of the Appalachian mountains, especially in the extreme precipitation. When the threshold used to define a precipitating day is reduced from 1mm day^{-1} to 0.25mm day^{-1}, the median value of precipitation is reduced at all resolutions (by approximately 30%) but the impact on the extreme precipitation is minimal (not shown).

The HRES data has a marked decrease both in the median and extreme precipitation values at nearly all locations in comparison to the station data (Fig. 2.5 a-d). This decrease in extreme precipitation with objective analysis is consistent with the results of Ensor and Robeson (2008). However, Ensor and Robeson (2008) did not find significant differences in the mean precipitation between the selected stations and their closest analyzed point. We find that the mean precipitation (not shown) behaves similarly to the median precipitation (Fig. 2.5 a,c), suggesting that use of the median instead of the mean is not the cause of the discrepancy between our study and that of Ensor and Robeson (2008). One explanation is that Ensor and Robeson (2008) only compared stations that were in close proximity to grid points, and consequently measured the smallest errors possible between a station and an analyzed point. Their study also only included the Midwest, which our results show has smaller changes in the median than other regions of the US.

In general, median and extreme precipitation are higher in the LRES-interp than in the LRES (Fig. 2.5 e,f,g,h), with differences ranging from 0 to 30% (Fig. 2.6). These differences are solely attributed to the interpretation of a model grid box being a point estimate or area average respectively, since both low resolution fields are derived from the same HRES data. These results are in agreement with Chen and Knutson (2008a), who also examined the impact of interpolation and remapping on extreme values but at a lower resolution. They show that the 5 and 50 year return period values of daily precipitation were smaller when using an interpolation method as opposed to a remapping method, where the return period is defined here as the daily amount of precipitation that is expected to occur only once every 5 and 50 number of years.

These results are important to consider when validating GCM output against station observations. Differences between the station value and the LRES median and extreme precipitation can be as large as 50%. This exemplifies why direct comparison between station data and GCM output is inappropriate due to the smoothing that occurs during the spatial transformation. The minimum value to define a precipitating day is also an issue across scales, as it is easier to attain at the station level than averaged over an entire grid box. Furthermore, any change in precipitation in a GCM could represent a much larger change at a point location. We also show the importance of the interpretation of model data as either a point value or an area average. In our subsequent analysis we will use the area averaged interpretation. As discussed previously, model precipitation is often parameterized and dependent on fluxes across grid boundaries, and as such we believe it is best represented as an area average within a grid box, in keeping with Chen and Knutson (2008a).

2.4.2 Impacts of Station Density

In this section, we present the results of our experiment on the impact of reducing station density on the statistics of HRES and LRES precipitation fields. Distributions of climatological errors with respect to station density are produced by creating scatter plots of the percent climatological errors of all the stations within various regions of the US. Climatological errors in the HRES and LRES data exhibit similar behavior, but in general the HRES data (Fig. 2.7) exhibits larger percent errors than the LRES data (Fig. 2.8), as evidenced for the extreme precipitation errors. Unlike the errors in the LRES data, the HRES errors are often large even when the initial station density is high. This implies that there are many locations where the GHCN data does not have an adequate station density to represent extreme precipitation with the HRES product. The LRES gridded data however, is less sensitive to data density due to area averaging. Results are similar for the median precipitation, however the climatological errors are smaller than in the extreme precipitation for both HRES and LRES fields (not shown). The larger impact of station density on extreme precipitation than on median precipitation seen here is in keeping with observations in other studies that smoothing has a large impact on extreme values (Ensor and Robeson, 2008), Hofstra et al. (2010), and Chen and Knutson (2008a).

The shapes of the climatological error distributions can be broadly separated into two categories. The first is characterized by errors that initially grow at higher station density but remain bounded at lower station density, hereinafter referred to as a bounded response to decreasing station density. This distribution shape is found in the central and eastern US consisting of the Northern Plains, Southern Plains, Great Lakes, Gulf, and East Coast regions (Figs. 2.7-2.8). The second distribution shape is an exponential increase with decreasing station density (exponential response), which is found in the western US consisting of the West Coast, Rockies, and North American Monsoon regions (Figs. 2.7-2.8). These responses to decreased station density are both prominent in the HRES (Fig. 2.7) and LRES (Fig. 2.8) data even with the smoothing involved in the LRES data. These results are consistent with Daly (2006), who suggests that regions, such as the western US where the coast or complex terrain influence precipitation will be more difficult to represent with objective analysis schemes. The two type of error distributions also have different seasonalities. For instance, the Gulf region has larger percent errors in the JA than the JF period, while the Rockies region show the opposite seasonality (Fig. 2.9). The Gulf and Rockies regions are representative of all regions in the western and eastern US respectively (not shown).

The shape and seasonality of the error distribution is further investigated using the decorrelation length scale of precipitation. The decorrelation lengths are longer in JF than in JA (Fig. 2.10). In the JF period, the decorrelation lengths are longer in the East and along the West Coast than in the central US, ranging from approximately 500 to 200 km respectively. The longer decorrelation lengths coincide with regions that experience more synoptic-scale winter precipitation systems. The decorrelation lengths are generally shorter in the summer with longer lengths to the North ($\approx$250 km) than the South ($\approx$100 km). This is consistent with the northward movement of the storm track in the summer, resulting in more synoptic-scale systems to the north while the south is more prone to air mass convection. In general, the difference in spatial gradient in decorrelation lengths is smaller in JA than in JF.

Geographic differences in the decorrelation length scale were also noted by Osborn and Hulme (1997) in western Europe. For instance, they show that the decorrelation length scale in France (400-480m) were 4 times that in northern Italy (80-160m). Decorrelation lengths were found to be longer in the winter compared to the summer across all of Europe (Osborn and Hulme, 1997; Hofstra and New, 2009), which is in accord with results presented here for the eastern US. This was attributed to the predominance of larger scale precipitation systems in the winter and smaller-scale convective systems in the summer (Osborn and Hulme, 1997; Hofstra and New, 2009). Furthermore, Hofstra and New (2009) examined the relationship between synoptic typing and decorrelation length, which further demonstrated that the presence of synoptic scale forcing leads to longer decorrelation lengths, consistent with this seasonal dependence.

Chen and Knutson (2008b) examined the impact of station density on the relative biases in correlations between a set of withheld stations and gridded station datasets, using different objective analysis methods. They withheld 10% of the initial number of input stations for cross-comparison, while the remaining stations were gridded several times with systematic removals of input stations, using the different objective analysis methods. Each withheld station was then cross-compared to the nearest grid point in the analyses with decreasing input stations. They found that their biases increased as station density decreased, and that this effect was highest in the summer season. In our study, we see two different seasonal responses in precipitation statistics depending on the region of study, whereas they examine an average over the entire US. Since their withheld stations are randomly chosen and there are significantly more stations located in the eastern US, their verification set is likely biased towards the eastern US. This would explain the agreement with our results for the eastern US, as they likely saw a predominantly eastern US response. Our results are also independent of the large differences in station density across the US because we examine errors with respect to station density as opposed to percent input stations.

The central goal of the station density experiment was to determine the range of potential representativeness errors in gridded station data related to station density. Considering the more general case of the annual climatological error over the entire US, we use exponential fits applied to the 1st and 99th percentiles of the error distributions (red line in Figs. 2.7-2.8, produced as described in Section 3c) to obtain an estimate of the lower and upper error bounds versus station density respectively. A table of these values of the upper and lower bounds of percent error for given station density is provided for median and extreme precipitation, and for the HRES and LRES grids (Table 2.1). These results were duplica

ted using a lower minimum threshold to define a precipitating day of 0.25mm day^{-1}. There are relatively small differences when using the 0.25mm day^{-1} instead of the 1mm day^{-1} threshold, with somewhat larger magnitudes of errors and similar behaviors of representativeness errors with respect to station density (Table 2.2).

Using the initial station density across the US (Fig. 2.3), maps of the upper and lower error bounds at each grid box are created (Figs. 2.11-2.12). The median climatological errors, in both the HRES (Fig. 2.11a,b) and the LRES fields (Fig. 2.12a,b), are typically lower than the extreme climatological errors (Figs.2.11c,d and 2.12c,d, respectively). In general, climatological errors in median and extreme precipitation are higher in the HRES (Fig. 2.11) than the LRES (Fig. 2.12) data. This is expected as the area averaging in the LRES data tends to reduce climatological errors. The magnitude of the upper bound of climatological errors (Figs. 2.11a,c and 2.12a,c) tends to be higher than the lower bound of climatological errors (Figs. 2.11b,d and 2.12b,d) at all resolutions and for both the median and extreme precipitation, indicating a tendency towards positive climatological errors in precipitation. Biases in LRES precipitation due to inadequate station density for the median (Fig. 2.12a,b) and extreme (Fig. 2.12c,d) precipitation can range from as low as 0% in well sampled regions in the East, to as high as 50% in the poorly sampled Rocky Mountains. The lower and upper error bounds tend to be dominated by the larger errors found in the western US at lower station density, however this has a small impact on the results because the initial station density is higher in the eastern US.

2.5 Discussion and Conclusions

This study explores the representativeness errors of gridded precipitation data through the changes in precipitation statistics as station data is gridded. We observe a dramatic decrease in median and extreme precipitation as station data is upscaled to the high resolution (HRES) objectively analyzed (OA), low resolution interpolated (LRES-interp), and low resolution remapped (LRES) fields. This implies that even if a GCM were to perfectly represent areal averaged precipitation within model grid boxes, its median and extreme precipitation would be lower than that of a station measurement due to representativeness errrors. This is an important factor when using future climate predictions from GCMs to determine the societal implications of climate change, as society experiences precipitation at a point location as opposed to an area averaged region.

The interpretation of a model grid as a point value or an area average across a GCM grid box can have large impacts on the resulting precipitation statistics. The point value assumption generally leads to larger median and extreme values than the area average assumption, with differences reaching 30%. These results are consistent with Chen and Knutson (2008a), but in this analysis it is repeated at a resolution typical of the current generation of GCMs. This has significant consequences for GCM validation, demonstrating the importance of the methods used to upscale station data to GCM resolutions. We advocate objectively analyzing to a higher resolution followed by remapping to a lower resolution, to upscale station data for comparison with model output, in agreement with others (Hewitson and Crane, 2005; Chen and Knutson, 2008a). This is consistent with the area average view of a GCM precipitation output.

An examination of climatological errors resulting from low station density are examined for different regions of the US. Two characteristic climatological error responses to decreasing station density depending on the homogeneity of station precipitation distributions within the radius of influence are identified and can be broadly geographically separated into the eastern and western US. Climatological errors in the eastern US begin at higher station densities but do not grow exponentially and in general have a small negative bias. The error structure and seasonality in the western US is different from that of the eastern US. As station density decreases the upper and lower bounds on climatological errors grow exponentially in both positive and negative directions. Furthermore, these two error responses exhibit differing seasonalities, in the eastern US percent error is greater in the JA period and in the western US in the JF period.

In a previous study by Bussières and Hogg (1989), it has been shown that decreased distance between stations and OA grid points results in decreased OA errors. How this translates to climatological errors in precipitation distribution however, is not straightforward. In an OA scheme there will always be an element of smoothing due to the influence of neighboring points. This smoothing is reduced as the proximity of stations to the analysis point increases and the OA point is closer to the true precipitation field. We propose two conceptual frameworks to explain the observed impact of station density on the climatological average of OA precipitation statistics. The first will be applicable to the entire US and the second solely for the western US.

In the first conceptual framework, we assume that the distribution of precipitation is relatively homogeneous. This is the case in the eastern US, as evidenced by the homogeneity in the median and extreme precipitation value in the east (Fig. 2.5a,b). The higher the station density the closer the analysis is to the truth, and the lower the station density the greater the influence of more distant stations on the analysis point. In the case of homogeneous distributions, this implies that we will have a greater influence of stations with less shared variance (ie. less correlated), but which have a similar distribution. As a result, the averaging of less shared variance biases the OA of precipitation towards lower climatological median and extreme values, as station density is decreased. This explains the small bias towards negative climatological errors observed in many of the eastern regions at both the annual and bimonthly averaging periods, for HRES and LRES fields (Figs. 2.7,2.8,2.9). The seasonality of climatological errors in this framework is impacted by the decorrelation length. As the decorrelation length decreases the impact of stations with less shared variance on the analysis points will increase for the same search radius. This is consistent with the observation that climatological errors are higher when decorrelation lengths are shorter in JA relative to JF, in the eastern US (Fig. 2.9).

These results are consistent with those found by Hofstra and New (2009) in western Europe, and disagree with those of Osborn and Hulme (1997) and Kursinski and Zeng (2006). We assert that the disparity between these sets of studies is due to differences in the gridding methods used and can be described within the first conceptual framework. The current study and that of Hofstra and New (2009) conduct an OA on the station data and then perform an area average. In Osborn and Hulme (1997) and Kursinski and Zeng (2006), a simple averaging of station data is applied to achieve a grid box averaged value. As discussed in Osborn and Hulme (1997), the method of simple station averaging allows for the application of the theory of randomly correlated variables to explain the impact of stations density on grid averaged variance. The theory relates grid averaged variance (S_n^2), averaged station variance (s_i^2), average correlation between stations ($\bar{r}$), and number of stations (n), through the following relationship:

$$S_n^2 = s_i^2[\frac{1 + (n-1)\bar{r}}{n}]$$

(Osborn and Hulme, 1997). The premise is that S_n^2 decreases as n increases because stations with less shared variance are averaged. In our method, it is the areal-averaging procedure that is analogous to an average of randomly correlated variables. The number of OA grid points are constant, so this is not where we see a dependence on station density. It is instead the OA step that depends on the station density, and the areal-averaging step simply perpetuates these errors with some smoothing due to averaging. This implies that the simple averaging method is not expected to follow the first conceptual framework. We in fact expect the opposite response, which explains the disparity.

The second conceptual framework applies when the distribution of precipitation is inhomogeneous. In this case, as station density decreases, more distant stations with substantially different precipitation distributions have a larger impact on the OA point, resulting in large climatological errors. In the western US, there is a predominance of orographically-forced precipitation. This results in preferred regions for higher amounts of precipitation, as well as large contrasts between precipitation median and extreme depending on the specific location

(Fig. 2.5a,b). Systematic errors in precipitation metrics can then result depending on the specific stations employed to conduct the analysis, making these regions more sensitive to station loss.

In the second framework, we may expect a similar relationship between the decorrelation length and errors that was seen in the first framework. However, the seasonality in the steepness of the inhomogeneity must be considered. We argue that in the western US the preferred wet/dry season of heavy precipitation, driven by a stronger jet stream and more intense storm track in the winter, steepens the gradient in climatological median (not shown) and extreme precipitation (Fig. 2.13). This effect will not be apparent in the decorrelation length as the Kendall's tau rank method employed does not assume a linear relationship for the correlation. As such, a change in the steepness of the gradient in precipitation statistics will not necessitate a change in decorrelation length. The decorrelation lengths in the western US are also longer in the winter than in the summer. This is more pronounced on the West Coast than in the Rockies or North American Monsoon regions (Fig. 2.10). Although there are also some increases in the errors at higher station densities in JA compared to JF in the Rockies regions, consistent with the first conceptual framework, the overriding signal is an exponential increase in errors at lower station density that is higher in JF than in JA (Figs. 2.13). In the context of the second conceptual framework, this is thus explained based on the seasonality in the magnitude of the homogeneity in the western US.

An envelope of potential upper and lower bounds of errors for all station densities are computed. Applying these boundaries to the actual station density at each grid point provides an estimate of the representativeness error, due to station density, across the US. These climatological errors are higher for the HRES field than the LRES field, and for extremes than median precipitation. Even within the US, which is known for having a relatively dense network of stations, there are wide regions with the potential for large climatological errors in median and extreme precipitation. For the LRES field, much of the eastern US has low values of potential errors, with upper bounds of 10-15%, whereas in the western US, these climatological errors are often around 35-45% (Fig. 2.12). When using the LRES field to validate a GCM, consideration of these errors is important for the interpretation of the model's ability to represent precipitation in the historical period.

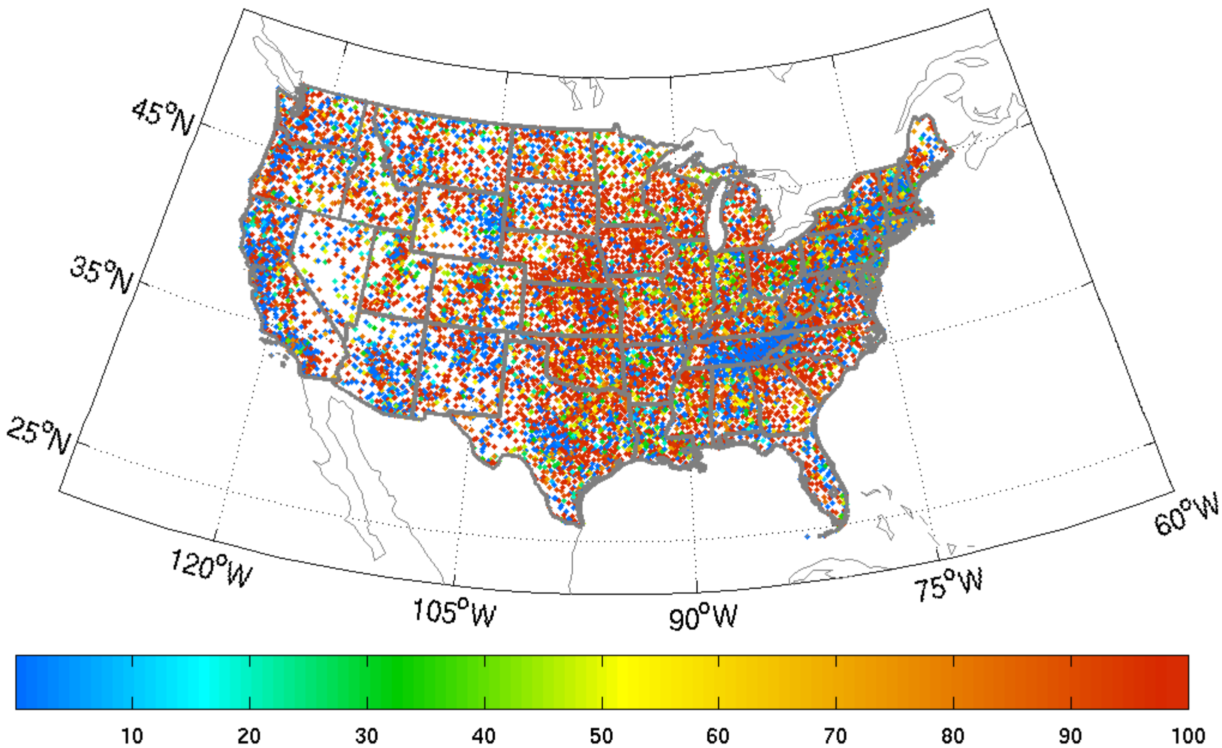

FIGURE 2.1: Average reporting rate (%) for each GHCN station.

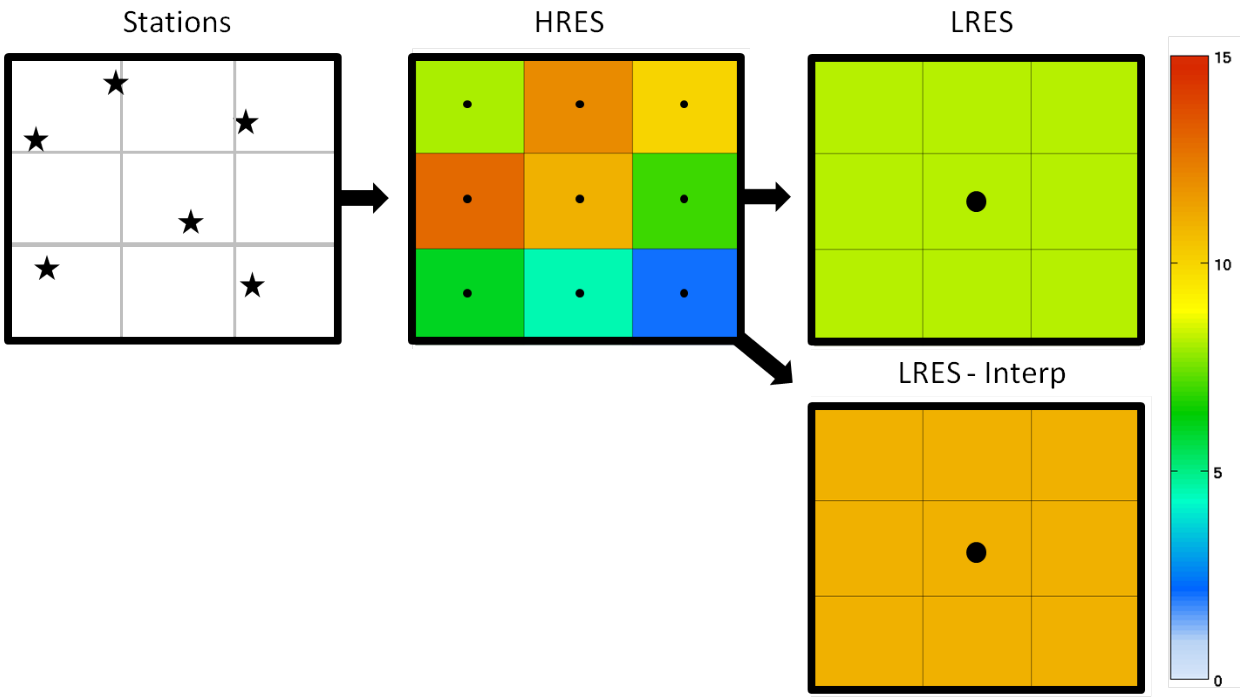

Figure 2.2: Schematic diagram displaying a simplified view of the grid transformation between station, HRES, LRES, and LRES-interp grids. Stations are shown as stars, HRES grid boxes as gray lines, HRES grid points as small black circles, LRES/LRES-interp grid boxes as thick lined boxes, and LRES/LRES-interp grid points as larger black circles. Grid box precipitation amounts are shown in color and are taken from a sample of actual data during a precipitation event. Note that in this simplified example the HRES and LRES grid points are collocated and 9 HRES grid boxes fit inside 1 LRES grid box. The LRES procedure therefore consists of averaging the HRES grid values. The LRES-interp method therefore simplifies to assuming the value of the middle HRES grid node.

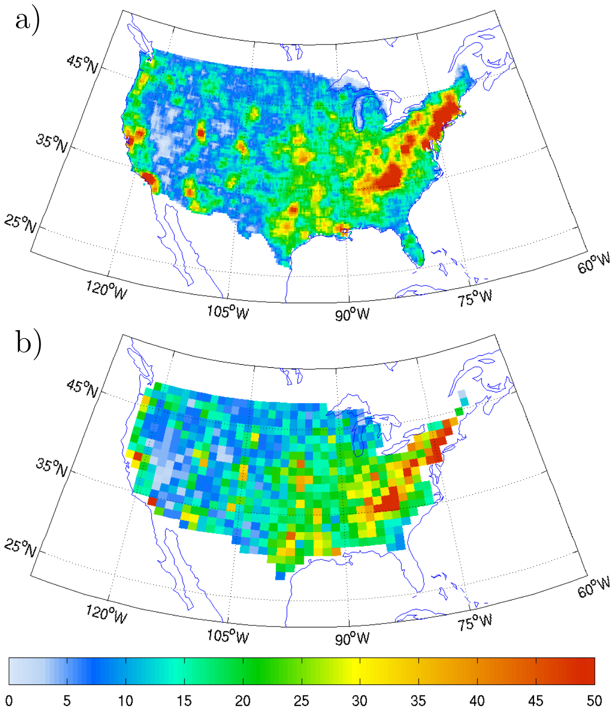

FIGURE 2.3: Initial number of stations per grid box for the HRES (a) and LRES (b) data.

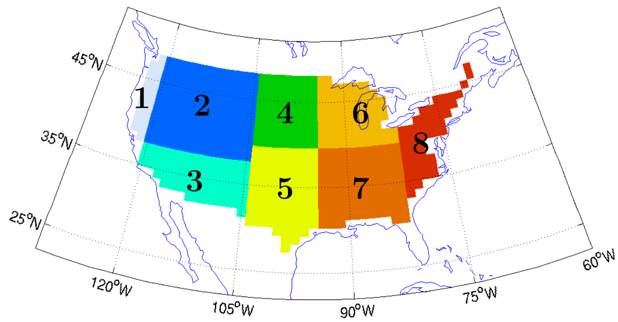

Figure 2.4: Map of regions in the US, 1) West Coast, 2) Rockies, 3) North American Monsoon, 4) Northern Plains, 5) Southern Plains, 6) Great Lakes, 7) Gulf, and 8) East Coast

Table 2.1: Table of upper and lower bounds of percent errors in median and extreme precipitation due to station density, over the entire US. Values are taken from exponential fits applied to the outer limits of the distribution of errors with decreasing station density, for both the HRES and LRES grids. The fits for the extreme precipitation are shown as red curves in Figs. 2.7 and 2.8, for the HRES and LRES fields respectively. Station density is defined as the number of stations within a 0.9x1.25° grid box.

	HRES Error (%)				LRES Error (%)			
	Median		Extreme		Median		Extreme	
Station Density	Upper	Lower	Upper	Lower	Upper	Lower	Upper	Lower
0	79	-34	135	-49	87	-18	164	-33
1	37	-30	54	-39	28	-14	36	-21
2	27	-28	36	-34	21	-12	25	-15
3	24	-26	31	-30	18	-10	21	-12
4	23	-25	30	-28	16	-8	18	-10
5	22	-24	28	-26	14	-7	15	-9
6	22	-22	27	-25	13	-6	13	-8
7	21	-21	26	-23	11	-5	11	-7
8	21	-20	25	-22	10	-5	9	-6
9	20	-19	24	-21	9	-4	8	-6
10	19	-18	23	-20	8	-4	7	-5
15	17	-14	18	-15	4	-2	3	-3
20	15	-11	15	-12	2	-1	1	-2
25	13	-8	12	-9	1	-1	1	-1
30	12	-7	10	-7	1	0	0	-1

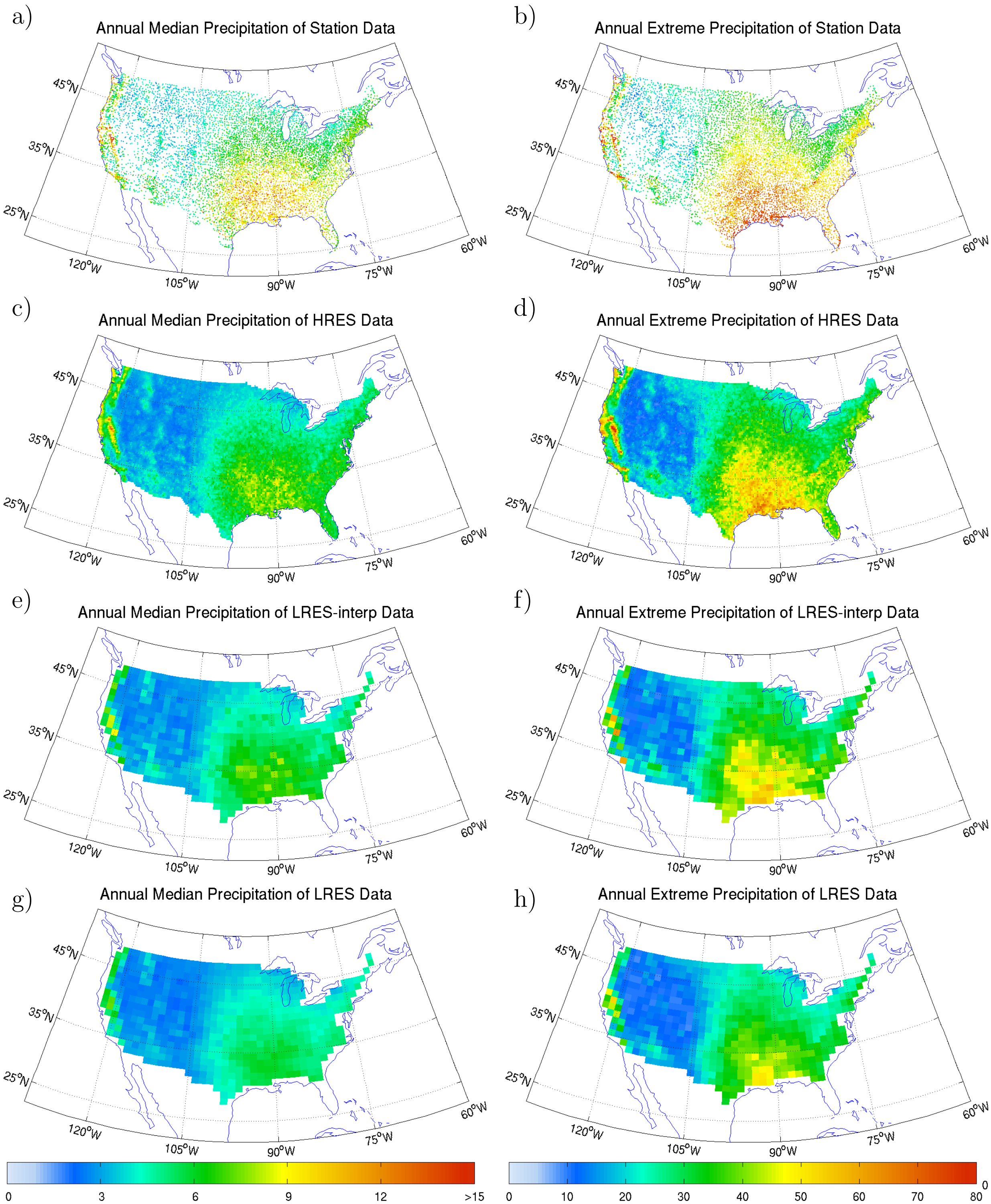

Figure 2.5: Average annual median (a,c,e,g) and extreme (b,d,f,h) precipitation (mm day^{-1}) calculated at each station or grid box for the GHCN station (a,b), HRES (c,d), LRES-interp (e,f), and LRES (g,h) data.

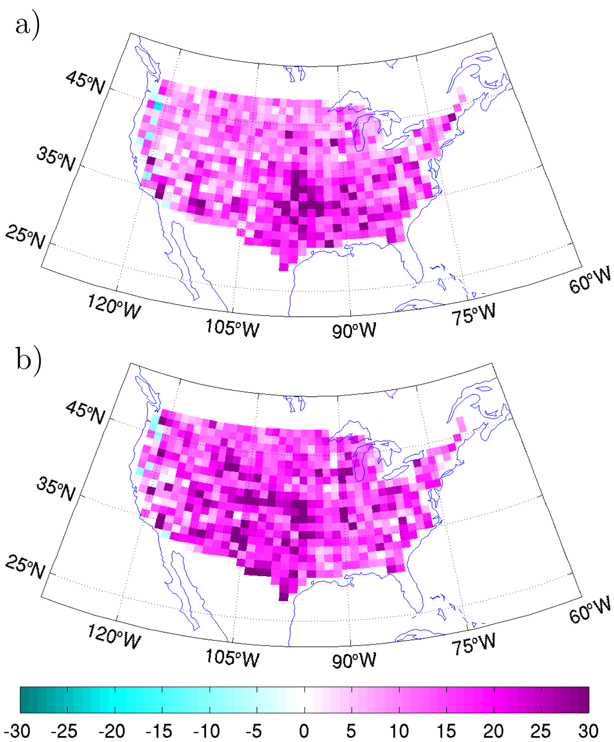

Figure 2.6: Percent difference in the average annual median a) and extreme b) precipitation between the LRES-interp and LRES fields.

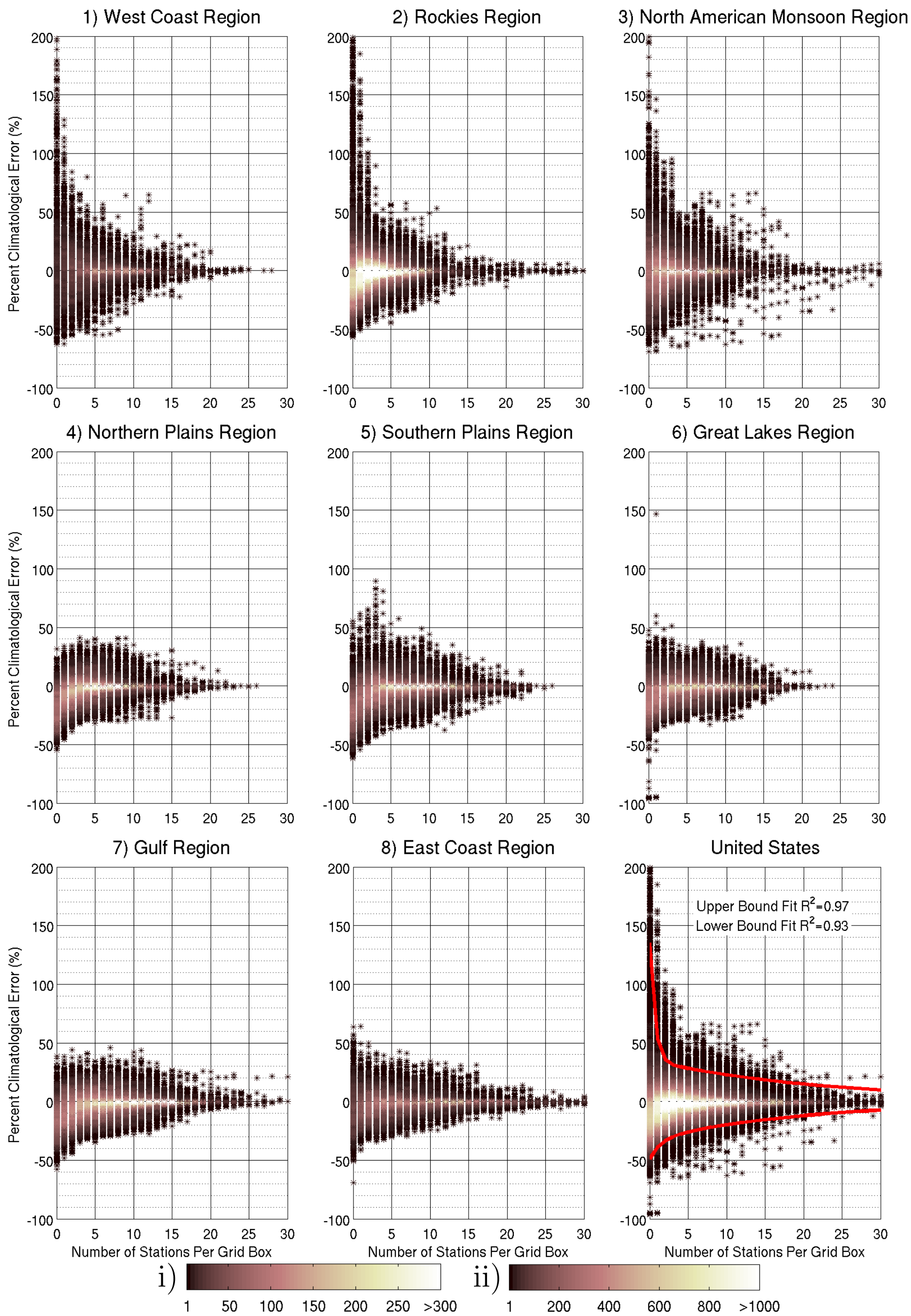

Figure 2.7: Percent climatological error of annual extreme precipitation (1979-2003) for all HRES grid boxes in a region and removal steps, as a function of station density (number of stations per 0.9°x1.25° box). The color of the symbols represents the concentration of climatological error points within 1% error bins, for a given station density. The corresponding colorbars are for the regions i) and the US ii). Exponential fits are applied to the 1st and 99th percentiles of the US distributions (red lines) and the coefficients of determination (R^2) of the fits are displayed.

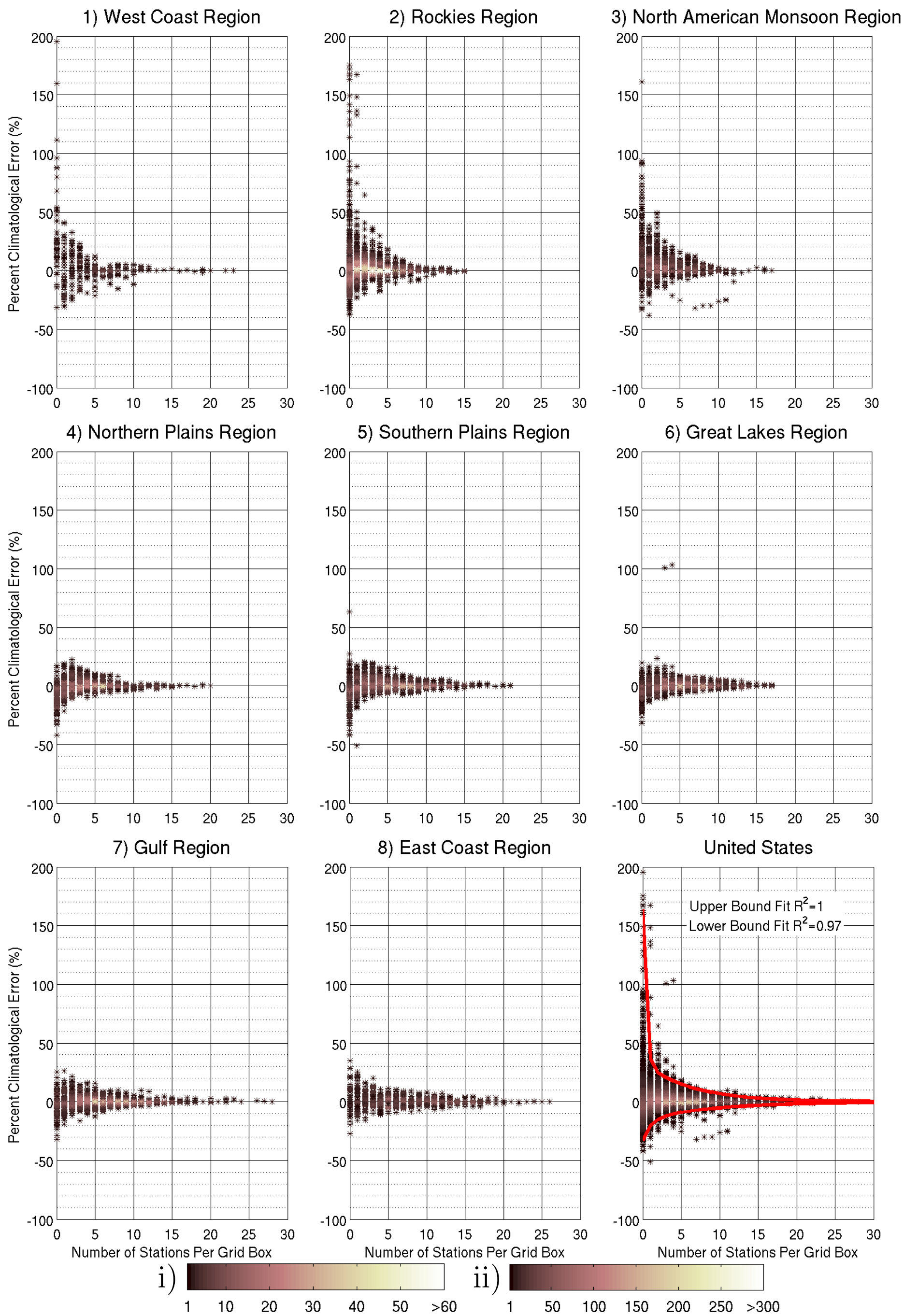

Figure 2.8: Percent climatological error of annual extreme precipitation (1979-2003) for all LRES grid boxes in a region and removal steps, as a function of station density (number of stations per 0.9°x1.25° box). The color of the symbols represents the concentration of climatological error points within 1% error bins, for a given station density. The corresponding colorbars are for the regions i) and the US ii). Exponential fits are applied to the 1st and 99th percentiles of the US distributions (red lines) and the coefficients of determination (R^2) of the fits are displayed.

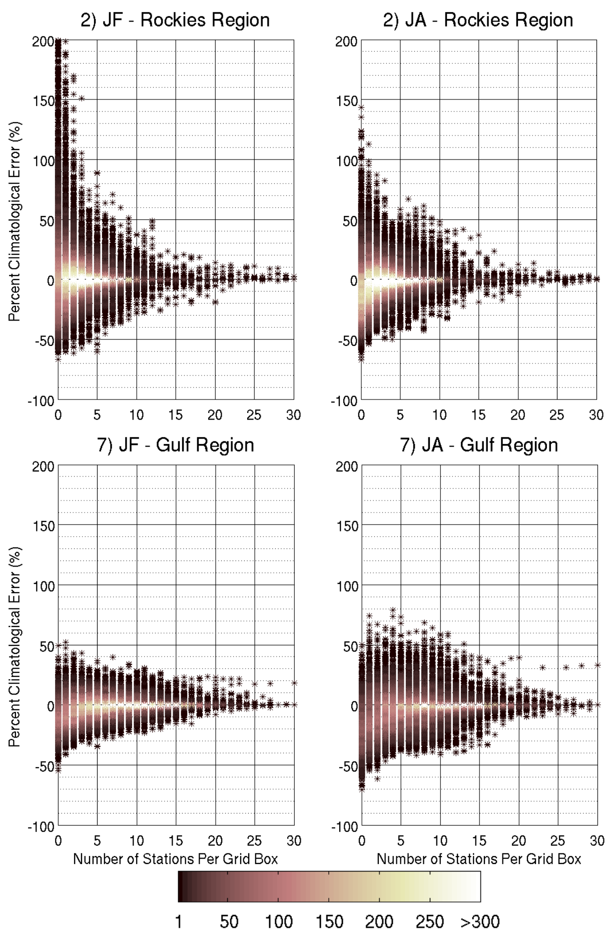

Figure 2.9: Percent climatological error of JA and JF extreme precipitation (1979-2003) in the Rockies and Gulf regions, for all HRES grid boxes in a region and removal steps, as a function of station density (number of stations per 0.9°x1.25° box). The color of the symbols represents the concentration of climatological error points within 1% error bins, for a given station density.

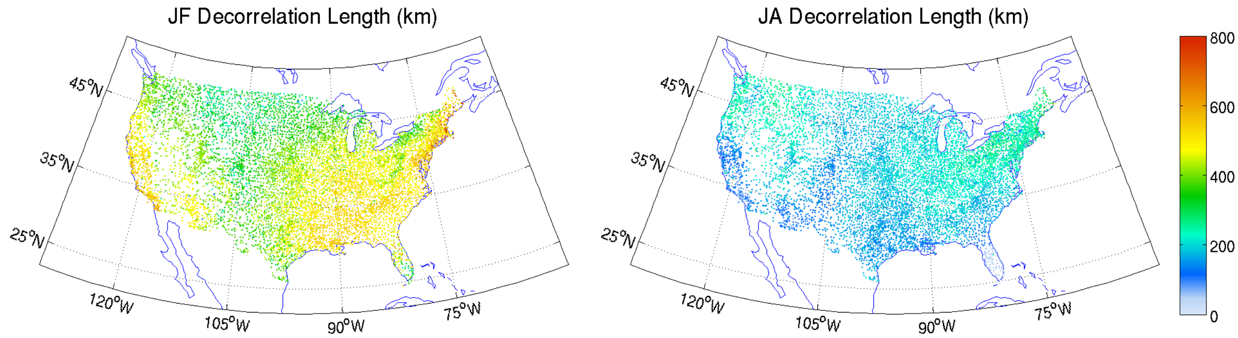

FIGURE 2.10: Station decorrelation lengths (km) for all stations within the US for both the JF and JA periods.

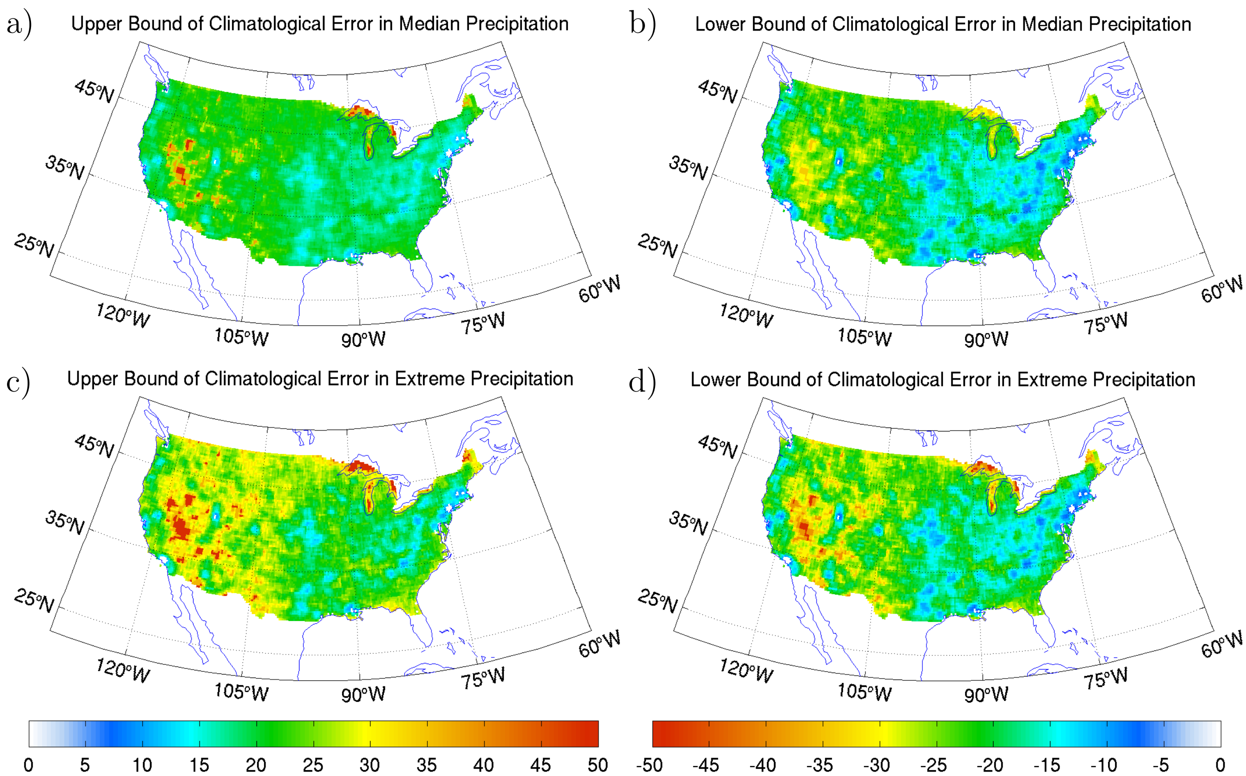

FIGURE 2.11: Upper (left) and lower (right) bound on the percent climatological error in average annual median (a,b) and extreme (c,d) of precipitation (1979-2005) for HRES data using the exponential fits of the 99^{th} and 1^{st} percentiles. Note that the color scales are reversed between the upper and low bound maps such that the magnitude of the color schemes are identical but in opposing directions.

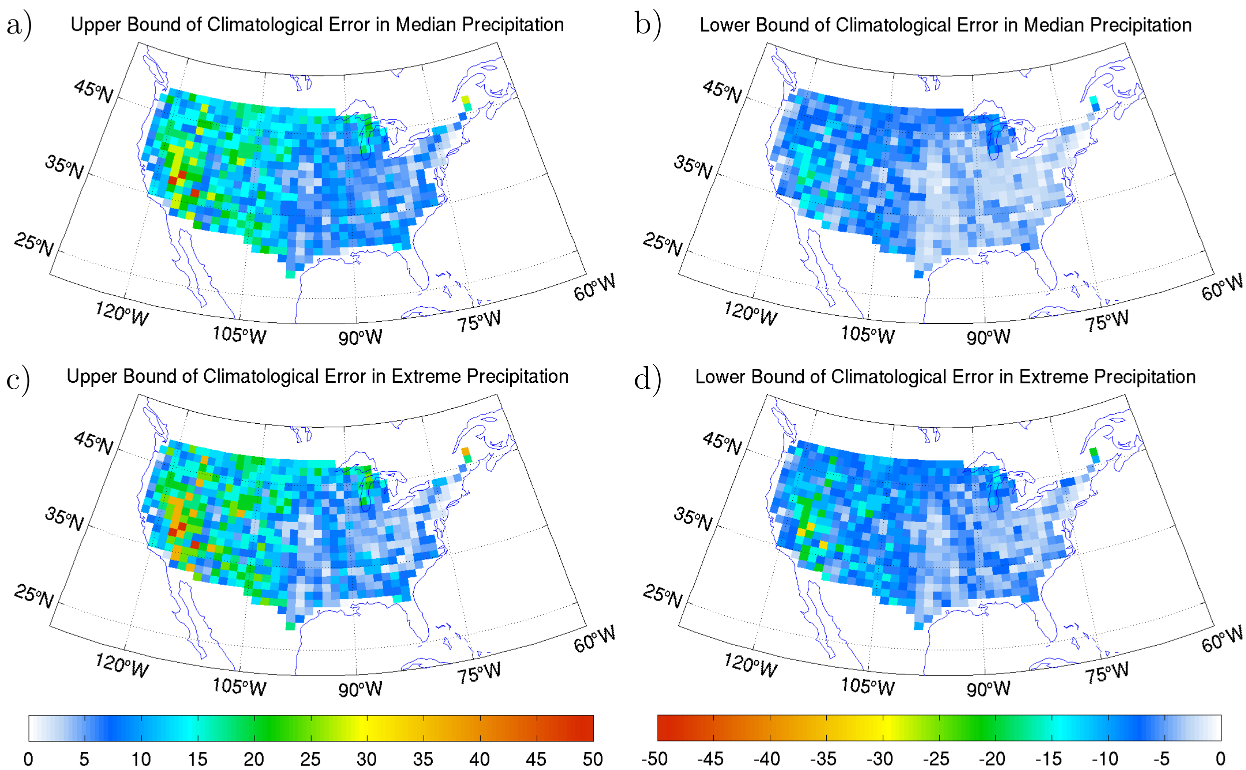

Figure 2.12: Upper (left) and lower (right) bound on the percent climatological error in average annual median (a,b) and extreme (c,d) of precipitation (1979-2005) for LRES data using the exponential fits of the 99$^{\mathrm{th}}$ and 1$^{\mathrm{st}}$ percentiles. Note that the color scales are reversed between the upper and low bound maps such that the magnitude of the color schemes are identical but in opposing directions.

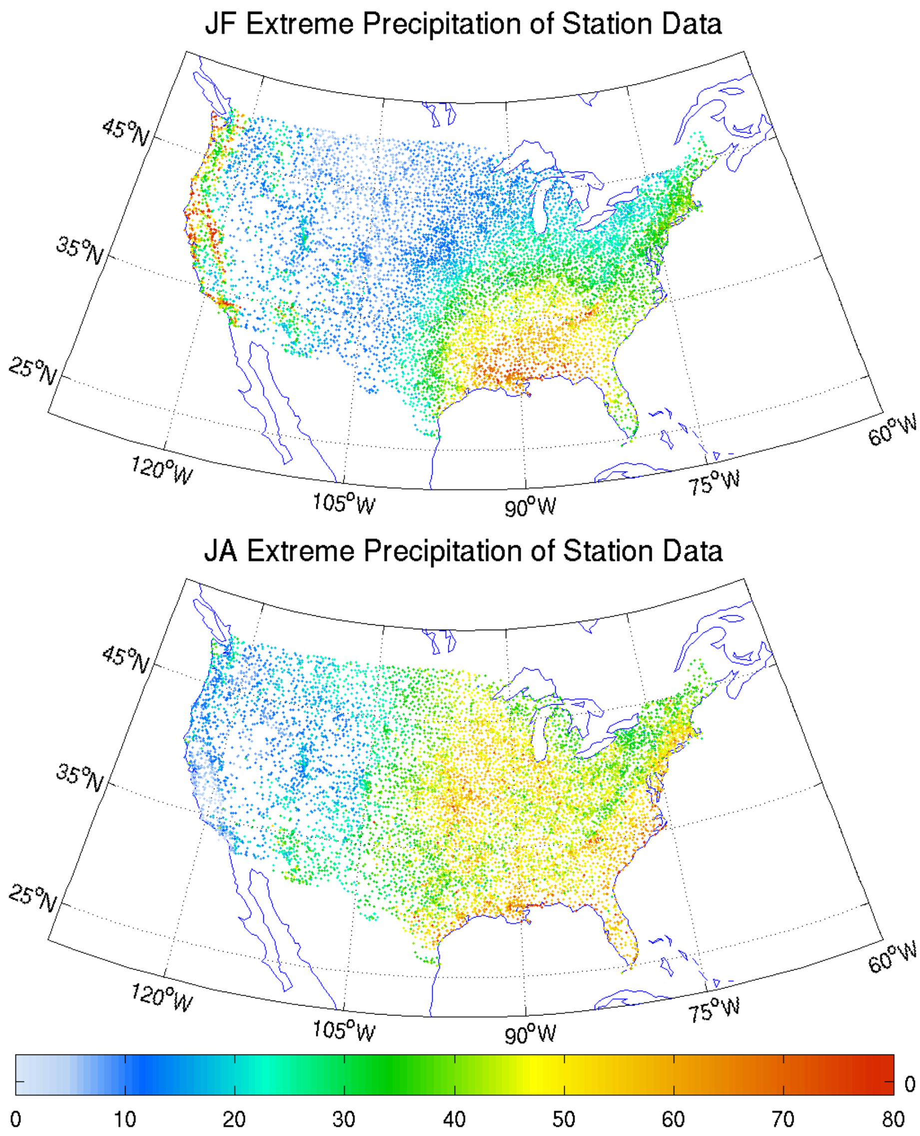

FIGURE 2.13: Climatological station extreme precipitation (mm day^{-1}) for both the JF and JA periods.

Table 2.2: Same as Table 2.1 but using a smaller threshold of 0.25mm day^{-1} to define a precipitating day.

	HRES Error (%)				LRES Error (%)			
	Median		Extreme		Median		Extreme	
Station Density	Upper	Lower	Upper	Lower	Upper	Lower	Upper	Lower
0	99	-41	153	-50	99	-23	178	-34
1	51	-37	59	-40	39	-17	45	-21
2	37	-35	39	-35	31	-14	27	-15
3	33	-34	33	-31	27	-11	22	-12
4	31	-32	31	-29	24	-9	19	-10
5	30	-30	30	-27	21	-8	16	-9
6	29	-29	28	-26	19	-7	14	-8
7	28	-28	27	-24	17	-6	12	-7
8	27	-26	26	-23	15	-5	10	-7
9	27	-25	25	-22	13	-5	9	-6
10	26	-24	24	-21	11	-4	8	-5
15	22	-19	19	-16	6	-2	4	-3
20	19	-15	16	-12	3	-1	2	-2
25	16	-11	13	-9	2	-1	1	-1
30	14	-9	10	-7	1	-0	0	-1

Chapter 3

Intercomparison of Extreme Values and Precipitation Distributions

This chapter is focused on evaluating the ability of the Community Climate System Model to represent the full distribution of precipitation including extreme values. The study highlights biases in reference datasets and places model errors within the context of these biases. This chapter consists of a paper published in the Journal of Climate: Gervais, M., J. R. Gyakum, E. Atallah, L. B. Tremblay, and R. B. Neale, 2014a: How Well Are the Distribution and Extreme Values of Daily Precipitation over North America Represented in the Community Climate System Model? A Comparison to Reanalysis, Satellite, and Gridded Station Data. *Journal of Climate*, **27 (14)**, 5219–5239, doi: 10.1175/JCLI-D-13-00320.1.

How Well Are the Distribution and Extreme Values of Daily Precipitation over North America Represented in the Community Climate System Model? A Comparison to Reanalysis, Satellite, and Gridded Station Data

Melissa Gervais, John R. Gyakum, Eyad Atallah, and L. Bruno Tremblay

Department of Atmospheric and Oceanic Science, McGill University, Montreal, Quebec

Richard B. Neale

National Center for Atmospheric Research, Boulder, Colorado

©American Meteorological Society. Used with permission.

The original publication is available at http://journals.ametsoc.org. The article is reproduced here with kind permission from the Journal of Climate: Gervais, M., J. R. Gyakum, E. Atallah, L. B. Tremblay, and R. B. Neale, 2014a: How Well Are the Distribution and Extreme Values of Daily Precipitation over North America Represented in the Community Climate System Model? A Comparison to Reanalysis, Satellite, and Gridded Station Data. *Journal of Climate*, **27 (14)**, 5219–5239, doi: 10.1175/JCLI-D-13-00320.1.

Abstract

An intercomparison of the distribution and extreme values of daily precipitation between the National Center for Atmospheric Research Community Climate System Model 4 (CCSM4) and several observational/reanalysis data sources is conducted over the contiguous United States and southern Canada. The use of several data sources, from gridded station, satellite, and reanalysis products provides a measure of errors in the reference datasets. An examination of specific locations shows that the global climate model (GCM) distributions closely match the observations along the East and West Coasts, with larger discrepancies in the Great Plains and Rockies. In general, the distribution of model precipitation is more positively skewed (more light and less heavy precipitation) in the Great Plains and the eastern United States compared to gridded station observations, a recurring error in GCMs. In the Rocky Mountains the GCMs generally overproduce precipitation relative to the observations, and furthermore have a more negatively skewed distribution, with less lower relative to higher daily precipitation values. Extreme precipitation tends to be underestimated in regions and time periods typically characterized by large amounts of convective precipitation. This is shown to be the result of errors in the parametrization of convective precipitation that have been seen in previous model versions. However, comparison against several data sources reveals that model errors in extreme precipitation are approaching the magnitude of the disparity between the reference products. This highlights the existence of large errors in some of the products employed as observations for validation purposes.

3.1 Introduction

From a socio-economic perspective, precipitation is one of the most important variables to predict in future climate, owing to its implications for water resources and natural disasters. For these purposes, it is not simply the average precipitation that is important, but rather the spatial and temporal distribution of precipitation intensities. One aspect of this distribution of crucial importance to society is extreme precipitation. For example, heavy precipitation can have large impacts on crops both due to the direct impact of flooding as well as the negative consequences of excess soil moisture (Rosenzweig et al., 2002; Gornall et al., 2010). A recent study by Scoccimarro et al. (2013) showed a 2-5% increase in the intensity of extreme events over land in the future, using an ensemble average of Coupled Model Intercomparison Project Phase 5 models. The use of global climate models (GCM) for prediction of changes in the distribution of precipitation requires continual assessment of the ability of these GCMs to represent the distribution in the current and historical climate. GCMs are well known to have significant errors in the distribution of precipitation, historically precipitating too frequently and with too low of an intensity when compared to observations (Dai et al., 1999; Iorio et al., 2004; Sun et al., 2006), even when the mean precipitation is well-represented (Chen et al., 1996; DeMott et al., 2007).

The convective parameterizations in GCMs tend to be associated with large errors in model precipitation, in particular in the extreme precipitation. Several studies have been conducted examining the diurnal cycle of precipitation in previous versions of the National Center for Atmospheric Research (NCAR) Community Climate System Model 3 (CCSM3) and have shown that the convective parametrization triggers convection too early and frequently, which does not allow for the build up of convective available potential energy (CAPE) necessary for heavier rainfall events (Dai and Trenberth, 2004; DeMott et al., 2007). Although increasing resolution does aid in many aspects of the representation of precipitation, it is improvements to the parametrization that are necessary to solve this problem of timing and consequently intensity (Iorio et al., 2004; Dirmeyer et al., 2012). In the Community Climate System Model 4 (CCSM4), a more recent version of the NCAR GCM, improvements have been made to the parametrization of deep convection to include convective momentum transport and dilution due to entrainment in the calculation of CAPE (Gent et al., 2011; Neale et al., 2013). Gent et al. (2011) compared the simulation of daily precipitation frequency over land between 20°N and 20°S in the CCSM4 model to the CCSM3 model. The CCSM4 showed significant improvement, even when run at the CCSM3's lower resolution, which they attribute to improvements to the deep convection scheme (Gent et al., 2011). However, there are significant differences in the convection that occurs in the tropics versus that which occurs in the midlatitudes.

In this study, we conduct a validation of the precipitation distribution and extreme values in the more recent versions of the NCAR GCM, the fully coupled CCSM4, the Community Atmosphere Model 4 (CAM4) and the Community Atmospheric Model 5 (CAM5). Since these newer versions of the NCAR GCM are improved over the previous version (CCSM3) both in terms of their parameterizations and resolution, their representation may be closer to observations than previous versions. As the ability of GCMs to produce accurate precipitation fields increases, we need to consider the validity of the common assumption used in the validation of GCMs, that observational errors are smaller than model errors. It is therefore important to consider the errors within the reference datasets used for validation, as well as the methods used to compare models to reference data. To this end, the validation will be made against three observational or reanalysis products to help constrain the extent of observational errors, which we may think of as the disparity between various reference data sources. A remapping method is used to re-grid between various resolutions instead of an interpolation to be consistent with the interpretation of a GCM being an area average of precipitation (Chen and Knutson, 2008a; Gervais et al., 2014b). Furthermore, all statistics are computed after the remapping procedure to ensure that there are no mismatches in scales as can occur when an index at a point location is remapped to a different resolution (Kursinski and Zeng, 2006), an issue that Sillmann et al. (2013) cited in their analysis. Focusing on the CCSM model allows for more detailed error analysis both spatially and seasonally, which helps to elucidate the abilities and limitations of the models in their representation of various precipitation mechanisms.

3.2 Data

3.2.1 North American Amalgamated Precipitation

We employ two currently available datasets: the Climate Prediction Center's Daily Unified Precipitation Dataset (UPD), provided by the National Oceanic and Atmospheric Administration/Earth System Research Laboratory (Xie et al., 2007), and the Daily 10km Gridded Climate Dataset for Canada (GCDC), provided by the National Land and Water Service (Hutchinson et al., 2009), to create a gridded precipitation data set over a contiguous region in North America. The native grid types and spacings of the two datasets differ, with the UPD grid being on a 0.25° lat-lon grid and the GCDC being on a 10x10 km Cartesian grid. We amalgamate these two datasets over their common time period of 1961-2006 to create the North American Amalgamated Precipitation Dataset (NAAP), where the UPD covers the contiguous US and the GCDC covers Canada south of 60°N.

The methods used to grid station data differed between the UPD and the GCDC. For the reader's reference, we will briefly outline these gridding methods used by the data creators of the UPD and the GCDC. The UPD was created through the optimal interpolation of 24 hour precipitation accumulations from gauge-based measurements in the continental US (Xie et al., 2007). The method of interpolation was conducted in two steps. First, a daily precipitation climatology was created by summing the first 6 harmonics of station data time-series for stations with reporting rates over 80% during the period from 1978-1997 (Xie et al., 2007). This daily precipitation climatology was then interpolated using the Shepard (1968) method, onto the 0.25° lat-lon analysis grid (Xie et al., 2007). An orographic correction was conducted on the daily climatology due to a general bias towards lower precipitation in mountainous regions, which results from a bias in station locations towards lower elevations in these regions (Xie et al., 2007). The Parameter-Elevation Regressions on Independent Slopes Model (PRISM) monthly precipitation climatology (Daly et al., 2002), which is adjusted for orographic effects using empirical relationships that are established locally and are available over the continental US, was used to conduct an orographic adjustment of the daily climatology. The correction to the daily UPD climatology was done by scaling the daily climatology so that its monthly accumulations closely match that of the PRISM monthly accumulations, while preserving the variability of the daily climatology (Xie et al., 2007). In the second step, the ratio of the daily station data over the un-corrected gridded daily climatology was calculated at each station location (Xie et al., 2007). Using the interpolated climatological field for the ratio allows stations to be used even if their observation length is too low to be included in the climatology (Xie et al., 2007). This ratio was then interpolated using the optimal interpolation of Gandin (1965) to the analysis grid (Xie et al., 2007). The interpolation of this ratio was conducted as this field is smoother in space than the daily station data itself and thus results in less errors when interpolated (Xie et al., 2007). Multiplying the interpolation ratio by the orographically adjusted daily climatology at each analysis grid point then yields the desired interpolated daily precipitation field (Xie et al., 2007).

The GCDC used a trivariate thin-plate smoothing spline (Hutchinson, 1995) to interpolate 24 hour precipitation accumulations from Environment Canada, creating a 10x10 km gridded precipitation dataset for Canada south of 60°N. In this method, the elevation was defined using a digital elevation model and a scaling factor was applied to increase precipitation with elevation. First, a binary field of precipitation occurrence was created from which grid points with and without precipitation were determined. Second, a precipitation surface was created through the interpolation of station data that had precipitation. In this step, the square root of the precipitation value was interpolated instead of the full value as it is more normally distributed. The final interpolated precipitation field was equal to the precipitation surface for grid points that were determined to be precipitating and zero where it was deemed non-precipitating. Hutchinson et al. (2009) find that the errors in the GCDC dataset are modest for seasonal and annual averages, but are relatively large for daily precipitation and extremes, even in the southern portion of the data where the station density is highest. This was attributed in part to the high spatial variability and low data coverage. (Hutchinson et al., 2009)

To combine the UPD and the GCDC into a single dataset we linearly interpolate the GCDC from a 10x10 km grid to a 0.25° lat-lon grid. The grid spacing of the GCDC is much higher than the UPD (>2.5 times) and so the distances over which the interpolation is conducted are short and as a result we expect that additional errors associated with using a simple linear interpolation over a more complex method should be small. The two datasets are then combined for the years 1961-2006 (when both datasets are available), where the GCDC covers Canada and the UPD covers the US. In the Great Lakes regions, the coverage is split between the GCDC and UPD datasets. Attempts were not made to smooth the boundary between the two datasets, as this could introduce errors in the higher order statistics of the combined dataset. The NAAP is the final product of this merger between the GCDC and the UPD.

3.2.2 Global Precipitation Climatology Project One-Degree Daily

The Global Precipitation Climatology Project One-Degree Daily (GPCP 1DD) is a satellite derived precipitation dataset at 1° lat-lon resolution from 1997 to 2008. This dataset should not be confused with the two other GPCP products, the GPCP version 2 satellite-gauge monthly precipitation dataset or the GPCP satellite-gauge pentad dataset. The GPCP 1DD is based on two satellite products, namely the Threshold-Matched Precipitation Index (TMPI) for the regions between 40°N and 40°S, and the Television and Infrared Observation Satellite Operational Vertical Sounder (TOVS) Pathfinder Path A outside of this region (Huffman et al., 2001). The GPCP 1DD will subsequently be referred to as the GPCP.

The TMPI uses 3-hourly brightness temperatures determined from infrared radiometers mounted on geosynchronous satellites, where precipitation is deemed to be occurring if the brightness temperature is below a threshold value and it is assumed to occur at a constant specified rainrate. Low brightness temperatures are indicative of ice particles in clouds, which has a relatively weak relationship to precipitation occurrence (Huffman et al., 1997). This method is mostly useful in regions of deep convection between 40°N and 40°S (Huffman et al., 2001). The threshold brightness temperature and conditional rainrates vary on a monthly basis, and are calculated using information from the Special Sensor Microwave/Imager and the GPCP version 2 satellite-gauge monthly precipitation dataset (Huffman et al., 1997).

The TOVS dataset is based on a relationship between cloud-top pressure, fractional cloud cover, a profile of relative humidity, and precipitation that is empirically determined using collocated gauge measurements (Susskind et al., 1997). The TOVS data goes through several processing steps to remove biases relative to the TMPI at the border between the two datasets. The TOVS data is re-scaled by setting low values of precipitation to zero so that the value of the total number of rainy days at the border with the TMPI are equal (Huffman et al., 2001). The precipitation amounts are rescaled during precipitating days so that the total amounts match the GPCP version 2 satellite-gauge dataset (Huffman et al., 2001). Finally, a smooth transition is created at the border of the TMPI and the TOVS on a daily basis by calculating the difference between the TOVS and TMPI data at the border, then adding a function to the TOVS that is this difference at the 40°N and 40°S border decreased linearly to 0 at 50°N and 50°S respectively (Huffman et al., 2001).

There are many known issues with satellite data in reproducing accurate daily values, in particular with respect to the frequency of events and the magnitude of extremes (Sun and Barros, 2010). Global daily precipitation products are rare and so the GPCP is an appealing dataset and has been used in numerous studies as a source of daily precipitation observations for the validation of GCM output (ex. Emori et al., 2005; DeMott et al., 2007; Scoccimarro et al., 2013). The creators of the GPCP however, suggest that the data only be used for time mean calculations due to errors in the daily amounts (Huffman et al., 2001). The GPCP will be included in this analysis since it often employed in the literature. However, the potential for errors will be indicated through comparison with the NAAP data, since it will be used without the spatial or temporal averaging advised by the data creators.

3.2.3 Climate Forecast System Reanalysis

The Climate Forecast System Reanalysis (CFSR) is a coupled global reanalysis spanning the period from 1979-2010 at 0.5° lat-lon grid resolution (Saha et al., 2010). In this analysis, 6-hourly precipitation totals are summed into daily precipitation totals to be consistent with the NAAP dataset. The precipitation output from the CFSR is produced solely by the CFSR background precipitation model, and does not directly include any precipitation observations (Personal Communications, the CFS team). Consequently it is likely to suffer from similar types of issues in the production of precipitation as GCMs, although its assimilation of other atmospheric variables and higher resolution should improve its performance. Furthermore, regions with a dense sounding network, such as the United States, are likely to be more well represented in the CFSR.

3.2.4 Community Climate System Model 3 and 4

The CCSM4 consists of four component models, the Community Atmosphere Model 4 (CAM4), the Community Land Model 4, the Parallel Ocean Program version 2, and the Los Alamos sea ice model (CICE). The component models are coupled at every atmospheric time step, except the ocean component model which is coupled once per day. We use a pre-industrial control run of the CCSM4 with additional output (MOAR), forced with historical international panel on climate change (IPCC) values for incoming solar radiation, carbon dioxide, and aerosols. The resolution of the atmosphere component model CAM4 in the CCSM4 control run is 0.9°x1.25° lat-lon and it has 26 levels in the vertical using hybrid sigma-pressure coordinates (similar to CCSM3). (Gent et al., 2011)

For comparison with the CCSM4 we also use a CCSM3 pre-industrial control run from the CMIP3 experiment. The resolution of the CCSM3 T85 model run is approximately 1.4°

lat-lon and also has 26 levels in the vertical. More details regarding this version of the model can be found in Collins et al. (2006).

The deep convection scheme in the model follows Zhang and Mcfarlane (1995), consisting in general of an ensemble of entraining plumes and compensating downdrafts at various heights that occur when the atmosphere is unstable. In CAM4 this scheme was revised to include impacts of convective momentum transport and the calculation of convective available potential energy (CAPE) to now be diluted through entrainment (Neale et al., 2013). The closure assumption of the deep convection scheme is that CAPE is consumed at an exponential rate. The inclusion of entrainment in the calculation of CAPE can reduce its value and improve the vertical moisture structure. The land model also received improvements that could aid in the representation of precipitation (Gent et al., 2011). More details on the physics, parametrization, and their improvements in this model version can be found in Gent et al. (2011) and Neale et al. (2013).

3.2.5 Community Atmosphere Model 4 and 5

To evaluate the ability of the atmosphere only model, output from an atmospheric model intercomparison project (AMIP) style control run of CAM4 and CAM5 will be used. These runs are conducted at the same resolution as the CCSM4 run, but using time-varying SSTs and sea ice in addition to the IPCC forcings. Although the CAM5 was produced shortly after the CAM4, there are changes to the shallow convection scheme and in the representation of aerosol indirect effects. Further details can be found in Neale et al. (2010).

3.3 Methods

Following Chen and Knutson (2008a), model output precipitation is interpreted in this study as an area average of precipitation within a model grid box. To make consistent comparisons between the various gridded observational, reanalysis, and model data, we ensure that all datasets are remapped from their native resolutions (Table 2.1) to the grid size of the lowest resolution data used in the comparison, in a manner that is consistent with the area average view point of a grid box. In this study, unless the 1.4°lat-lon CCSM3 is also being compared, the lowest resolution data is the CCSM4, CAM4, and CAM5 model output, which are all on a 0.9°x1.25° lat-lon grid, referred to as 1°. The resolution change is accomplished here using a first order conservative remapping method from the Spherical Coordinate Remapping and Interpolation Package (SCRIP) from the Los Alamos Laboratory (Jones, 1999). The method computes weights for each input grid point based on the area-overlap between the input grid boxes and the output grid boxes. Multiplication of the input grid precipitation field by these weights re-grids the dataset while conserving the total amount of precipitation.

Several metrics for the distribution of precipitation are utilized. Kursinski and Zeng (2006) showed that the order of operations of the computation of precipitation indices versus spatial averaging is important. In all cases, the statistics are calculated on the specified grid after the interpolation or remapping procedure, which is consistent with the method in Chen and Knutson (2008a). If the order of this operation is reversed, results of errors in GCMs may be ambiguous, as was found for example in Sillmann et al. (2013). All statistics are calculated during the time period of interest (annual or bimonthly) for a single year, then the value of each year in the time period is averaged. This climatological averaging time period is 1979-2005 for all datasets, except for any computation involving the GPCP where it is 1997-2005. There are small changes when all results are averaged over the 1997-2005 period, however they do not impact the interpretation of our results. The bimonthly periods used are January-February (JF), March-April (MA), May-June (MJ), July-August (JA), September-October (SO), and November-December (ND). Given the non-Gaussian distribution of precipitation, median and percentile values will be used as metrics of precipitation. The 97th percentile of precipitation in a given period for each year averaged over all years (1979-2005 or 1997-2005) will subsequently be referred to as the climatological extreme precipitation.

The full distribution of precipitation is represented using two metrics. First, the empirical cumulative distribution function (CDF) for all days is computed for each year, then climatologically averaged. The CDF is a common metric used for validation of GCMs, which shows the cummulative probabilities of increasing daily precipitation amounts. The significance of differences between CDFs is determined using the Kolmogorov-Smirnov (KS) (Massey, 1951; Stephens, 1970) and Cramer-Von Mises tests (CvM) (Anderson and Darling, 1952; Anderson, 1962). These two tests check the null hypothesis that the CDF of the test data are from the same population as the NAAP using different metrics of the difference between the distributions of the full precipitation time series (not the annual distribution climatologically averaged). Second, we show the annual total precipitation versus bins of daily precipitation intensity averaged climatologically, which we call the total mass distribution (TMD). This shows the contribution that each daily intensity range has towards the total precipitation. In relation to the CDF, the TMD can be thought of as an integration, over a range of daily amounts, of the change in probability times the amount and the number of days. The TMD is a physically intuitive metric that is useful in understanding the imporance of heavy precipitation events. The probability of heavy events are low but they have higher daily amounts. This makes them more significant in terms of their contribution towards the total precipitation, although in the CDF they represent relatively small changes. The skewness of the TMDs are used to demonstrate the spatial coherence of the differences in the shape of these functions between the various precipitation datasets. Generally, the TMDs of precipitation are positively skewed, since light precipitation occurs more frequently than heavier precipitation. A more positive skewness value translates to less high and more low daily precipitation amounts. A monte carlo method is used to test the hypothesis that the skewnesses of the TMDs are the same, relative to the NAAP. The data from the NAAP and the test dataset are randomly reasigned to two new data sets, 1000 times. The difference in skewness between the NAAP and test datasets are considered significant if outside the range of 5th to 95th percentiles of differences found using the monte carlo test.

3.4 Results

The three reference products, the NAAP, GPCP, and CFSR, each have advantages and disadvantages for use in the validation of GCMs. The NAAP data is based on direct station measurements and is thus considered to be the closest to the truth. The disadvantages of gridded station datasets like the NAAP are that they can have biases when the station density is low (Gervais et al., 2014b), they can suffer from measurement error in particular for solid precipitation (Goodison et al., 1998; Cherry et al., 2007), and they are only available over continents. The GPCP and the CFSR have the advantage that they are available globally. However, these datasets have the potential for large errors as the GPCP is created using indirect measurements and the precipitation in the CFSR is produced by a model. In this study we are using all of these datasets to evaluate precipitation in the CCSM model in North America. Focusing on North America allows for analysis of regional precipitation errors in more detail. Furthermore, satellite products like the GPCP and reanalysis products such as the CFSR are commonly used to validate models in regions where station data are not available (ex. Sillmann et al., 2013; Shiu et al., 2012). Consequently, this study has the advantage of comparing these reference products for validation purposes in a region with typically good station observations.

To evaluate the potential for biases in the NAAP due to low station density, we apply results from an experiment by Gervais et al. (2014b) who examined the impact of station density on precipitation statistics in the United States. Their experiment consisted of the interpolation and remapping of station data using the same methodology as in this study, but conducting the gridding repeatedly with successively fewer stations. In doing so they are able to infer biases resulting from decreased station density. They normalize these results across a region to produce a distribution of potential biases with respect to station density. They found that the impact of station density on biases in precipitation statistics changed seasonally and regionally. In general, small (large) decorrelation length scale of station data and low (high) spatial homogeneity of station statistics result in larger (smaller) biases (Gervais et al., 2014b). Experimentally derived upper and lower bound curves of potential biases in climatological median and extreme precipitation over the entire United States are created by fitting a curve of the form:

$$y = ae^{bx} + ce^{dx} \tag{3.1}$$

to the 99^{th} and 1^{st} percentiles of this distribution (Gervais et al., 2014b). This provides a measure of the upper and lower bound of biases that takes into account the full breadth of biases across the United States.

In this study, the experimentally derived upper and lower bound curves of potential bias in climatological precipitation versus station density in gridded station data in the US of Gervais et al. (2014b) are applied to the station density of the NAAP (Fig. 3.1). This is used to produce an estimate of biases in the NAAP due to station density (Fig. 3.2). According to Hutchinson et al. (2009), the GCDC dataset is the most complete daily dataset of Canadian precipitation for this time period, though the station density is smaller than any of the non-Canadian datasets that they came across. The density of stations used in the NAAP is very heterogeneous with the most stations located in more densely populated regions, less stations in mountainous regions, and scarce stations in northern Canada (Fig. 3.1). As a result there are very large biases in much of Canada (Fig. 3.2). There are additional sources of bias in the NAAP due to station measurement error, which has been shown to be on the order of 10% for liquid (Adam and Lettenmaier, 2003) and on the order of 100% for solid precipitation (Goodison et al., 1998; Cherry et al., 2007). In this analysis the NAAP is generally considered to be the closest representation of the true precipitation field, however potential biases associated with lower station density will still be considered.

Examining the average annual median precipitation of the observational and reanalysis data provides a general idea of the magnitude and patterns of observational errors in these datasets. The GPCP has a similar pattern in the annual median precipitation as the NAAP, although there is a lack of detail in the western mountain ranges in the GPCP (Fig. 3.3b,c). The biggest difference between the GPCP and that NAAP is that generally the magnitude is higher in the GPCP and there is a discontinuous decrease in the median precipitation in the eastern US when the input data source changes from the TMPI (south) to the TOVS (north) at 40°N (Fig. 3.3b,c). At this boundary the percent errors in median precipitation in the GPCP relative to the NAAP drop from 40-60% to 0-20%. The pattern of error in the CFSR relative to the NAAP is very different than that of the GPCP (Fig. 3.3c,e). Differences in the CFSR relative to the NAAP include a reduction in area and eastward shift of the region of higher annual median precipitation in the southeastern US (Fig. 3.3d,e). However, the errors in the Eastern US and Canada are typically less than 20%. The CFSR has higher annual median precipitation in the Rocky Mountains stretching from the US to Canada and in much of Canada, than the NAAP (Fig. 3.3b,c), with percent errors up to 60%. The potential of errors due to station density in the NAAP in these regions are high for the climatological median and the extreme precipitation, however the errors in the CFSR relative to the NAAP in the Rockies are greater than the upper bound of these climatological errors (Fig. 3.2).

There are some large climatological errors in the average annual median precipitation between the models and the NAAP, however the results are generally very promising. In certain regions, such as the East Coast, the magnitude of the percent climatological error relative to the NAAP in the average annual median precipitation is lower than that of the GPCP in the eastern US and Canada (Fig. 3.3). If we consider observational error to be the difference between reference products, this implies that the models are within observational error in these regions. One area of substantial errors in all the model runs is an underestimation of the median precipitation in the Southeastern US with up to 40% difference relative to the NAAP, which is smaller in the CCSM4 than in the CAM4 (not shown) and CAM5 (Fig. 3.3f,g,h,i). There are some general biases toward higher median precipitation along the West Coast and interior mountain ranges in both models, which are higher in the CCSM4 than the CAM5 (Fig. 3.3f,g,h,i). In Canada, the CAM4 (not shown), CAM5 and CCSM4 generally perform well compared to the NAAP except for an overestimation over the Rocky Mountains and some higher values of median precipitation in the North that are similar to those of the CFSR and smaller than those of the GPCP (Fig. 3.3f,g,h,i).

In addition to errors in the median field, we are interested in how well the distribution of precipitation is represented. Specific locations are chosen to use as examples of these distributions, where the locations are geographically diverse and include sample points with different precipitation climatologies (Fig. 3.4). How representative these points are of the area around them depends on the spatial homogeneity of the precipitation distribution, which is typically higher in the East than the West (not shown). The CDFs and TMDs are shown in figures 3.5 and 3.6. For the CDF, we can apply the KS and CvM tests of significance, which are used here to determine whether products have the same distribution as the NAAP. The CDFs at these locations are significantly different for all datasets, a result that is generally true apart from some isolated locations (not shown). For the TMDs we use a monte carlo method to determine whether difference in the skewness of the TMDs, relative to the NAAP, are significant. The skewnesses of the TMDs and their significances are shown for the entire region of study in figure 3.7.

The northern and southern West Coast points are within a coastal region with predominantly orographic precipitation. The seasonality in these locations is tied to the intensity of the storm track, with higher precipitation in the winter when the storm track is more intense. The largest discrepancies in the CDFs of the nothern West Coast point are that the GPCP and the CAM5 have too many non-precipitating and light precipitation days (Fig. 3.5a). This results in the GPCP having too low of values of total precipitation throughout much of the range of daily amounts (Fig. 3.6a). For the CFSR, CCSM4, and CAM4 CDFs, we see somewhat higher probabilities begining from the 1mm day^{-1} until the 20mm day^{-1} amounts, or a shallower slope in probability over this time, which results in lower precipitation totals for these amounts compared to the NAAP (as seen in Fig. 3.6a). In general, for the northern West Coast points the TMD of the models are bracketed by reference products throughout the entire distribution, except the CAM5 for very low daily amounts (Fig. 3.6a). The southern West Coast point typically has much less precipitation compared to other locations (Fig. 3.6b). The CDFs and the TMDs show that the CCSM4 has a higher number of precipitating days resulting in a general over production across all intensities for the southern West Coast (Fig. 3.6b). The CAM5 also has some notable issues at this location with too many non-precipitating and light precipitating days until around the 5mm day^{-1} amount.

The two Rockies points (western and eastern) are inland but are similarly in a region of predominantly orographic precipitation. The precipitation intensity in the Rockies is typically lighter and the annual total is very low compared to other locations. The CDFs for the two Rockies points show that the NAAP has more rain free days than any of the other products (Fig. 3.5c,d), which results in there being more precipitation and a shift towards higher amounts in the other products (Fig. 3.6c,d). The exception is the GPCP for the Eastern Rockies point where there are less precipitating days at amounts $>$ 10mm day^{-1}, where the slope of the CDF curve levels off (Figs. 3.5d, 3.6d). For the GPCP, the western Rockies point is located south of 40°N and the eastern Rockies point is located North of 40°N (Fig. 3.4), where the data source changes from the TMPI to the TOVS respectively. The changes in the steepness of the CDF slope and the skewness of the TMD may be symptomatic of changes in data source for the GPCP, specifically since the distribution is skewed in the data processing and adjusted to produce a smoother boundary (Huffman et al., 2001). However, as discussed previously, the Rockies typically have a lower density of station observations and the NAAP precipitation is adjusted for orography. There is thus a possibility that the errors in the median and distribution in the region are related to errors in the NAAP either due to station density or to the orographic adjustment. In such regions it is difficult to determine what is observational errors and what is model error; however the general similarity between the NAAP and the GPCP for the western and the NAAP and the CFSR for the eastern Rockies points for the TMD suggests that the NAAP is performing well (Fig. 3.6c,d).

The North American Monsoon point is in a region that has low annual precipitation amounts and is named for the North American Monsoon, a period of enhanced precipitation during the late summer/early fall. The CDF reveals that there are more precipitating days in general in the models than the NAAP (Fig. 3.5e) and the opposite for the other reference products. This results in TMDs with amounts of precipitation that are consistently higher in the models than any of the reference datasets (Fig. 3.6e), where we can also see that the TMD is skewed towards higher amounts. The Great Lakes point on the other hand, is more well-represented by the models than the other CFSR or the GPCP for the CDF and the TMD (except the CAM5 for some amounts, Figs. 3.5f, 3.6f). This is particularly notable in the CDF for non-precipitating and low precipitation amounts (Fig. 3.5f). This implies that the CAM4 and CCSM4 models are within observational error at this location.

The East Coast of North America is influenced by the proximity to the Atlantic Ocean and the Appalachian mountain range. In the summer the region receives predominantly convective precipitation. During July-August and September-October, it can experience heavy precipitation from tropical cyclones that can impact anywhere along the coast. In the winter it tends to experience larger-scale precipitating systems, the most notable being Nor'Easters. The greatest difference in the CDFs of the northern East Coast point is that the GPCP has too little non-precipitating days followed by a steeply sloping probability of amounts up to 20mm day^{-1} (Fig. 3.5g), which results in an over abundance of daily amounts until the 20-25mm day^{-1} bin and an underproduction of heavier amounts (Fig. 3.6g). Similar to the eastern versus western Rockies where the two points are located on opposite sides of the 40°N change in GPCP data source, the TMD of the GPCP shows an excess of lighter and deficit of heavy events in the northern East Coast and the opposite in the southern East Coast (Fig. 3.6g,h), as well a change from an underabundance in the north to an overabundance in the south of days without rainfall (<1mm day^{-1}, Fig. (Fig. 3.5g,h)). For the model TMDs, there tends to be more higher amounts than the other reference products and for the CAM5 an underproduction of low precipitation amounts. The behaviour of the models are also the opposite for the southern East Coast relative to the northern East Coast, where we see a positively skewed TMD at the southern East Coast point for all of the models relative to the reference products (Fig. 3.6h).

The Great Plains and Gulf Coast regions experience a great deal of convection. For the Gulf Coast this is true for most of the year, whereas convection is particularly important in the spring/summer seasons in the Great Plains. The Great Plains and Gulf Coast points also have the greatest errors in their precipitation distributions. For the Great Plains point, all model-based products (CFSR and GCMs) have too much light precipitation and not enough heavy precipitation, seen both in the CDFs and the TMDs (Fig. 3.5i and 3.6i). This could be associated with the GCMs' inability to produce heavy convective precipitation events. The Gulf Coast point sees similar errors from the GCMs, but the CFSR performs much better than in the Great Plains in comparison to the NAAP (Fig. 3.5j and 3.6j). For the Gulf Coast CDFs, the GPCP has errors in the opposite direction (Fig. 3.5j), which demonstrate that if the GPCP were used solely to validate the GCMs, we would assume even larger errors in the GCMs, while the opposite would be true if the CFSR were used. These two locations highlight the importance of using several data sources for validation, and how the errors associated with reference data sources can have a large influence on the interpretation of model results.

A comparison of the skewness of the total precipitation distributions relative to the NAAP reveals spatial coherency in many of the features mentioned above for specific point locations (Fig. 3.7). There is a distinct shift in the difference in the skewness of the GPCP compared to the NAAP at 40°N, where it is less skewed south of 40°N and vice versa (Fig. 3.7a). This coincides with the change in data source from the TMPI (south) to TOVS (north) in the GPCP and is thus likely due to errors in the GPCP. This shift in the distribution was noted previously for the western versus eastern Rockies points and southern versus northern West Coast points. This seems to be a robust feature along the 40°N latitude except along the West Coast. The CFSR is negatively skewed relative to the NAAP in the West, where there is high orography, and positively skewed in the East (Fig. 3.7b). The differences in skewness between the GPCP and the CFSR relative to the NAAP are of the same magnitude but the spatial patterns differ.

The bias patterns of skewness in the GCMs are very similar to that of the CFSR, but more amplified (Fig. 3.7c,d). The CFSR, with higher resolution and mass fields based on assimilated data, is likely to have a somewhat better prediction of precipitation than the GCMs; however it is still model-based so the similar error patterns to the GCMs are expected. The skewness in the Great Plains is consistent with the idea that there is too much light and not enough heavy precipitation in the models, in particular in regions that experience convection. It is interesting to note that the error in the skewness in the Great Plains is higher in the uncoupled models (Fig. 3.7d) (CAM4 not shown) than in the fully coupled model (Fig. 3.7c), and the error in the Rockies is lower in the uncoupled models

(CAM4 not shown) and higher in the coupled model.

There are many regions in Northern Canada where the bias in the skewness with respect to the NAAP is negative for all the other reference and model products (Fig. 3.7). These regions include northern Quebec, Ontario, Manitoba, and the entire West Coast of British Columbia. It is unclear whether this is a result of a common bias in the GPCP, CFSR, CCSM4, and CAM5, or whether it is due to the sparseness of station data in these regions (Fig. 3.1) and the resulting potential for large errors in the NAAP data (Fig. 3.2).

The ability of the GCMs to reproduce observed extremes in different bimonthly periods is shown in the climatological extreme precipitation in each of these models with comparison to the NAAP (Fig. 3.8). In the NAAP, we see a maximum of extreme values along the West Coast whose seasonality is such that the extremes are greater in winter (JF, MA, and ND) and small or non-existent in the summer (MJ and JA). The models produce the higher extremes in this region as well as the seasonality; however during the bimonthly periods where this feature is largest (JF, MA, and ND), the magnitudes are on the order of 10-20 mm day^{-1} larger. Within the Rocky Mountains, the NAAP generally has finer scale structures, even though the models are remapped to the same resolution. Studies using an earlier version of the model saw that increasing the resolution resulted in much better representations of orographic precipitation (Gent et al., 2010; Iorio et al., 2004). Therefore, this may be a result of the model resolution being too coarse to fully capture details in the orography that are important for precipitation. During the JA period, the models have lower values than the NAAP in the North American Monsoon region. This may be indicative of issues representing the monsoon processes in the model. In general however, the largest errors in the climatological extreme precipitation are located east of the Rockies where heavier convective precipitation is frequent.

Focusing on errors in the Eastern US, one of the most notable features that the models are not able to produce is the heavy precipitation in the plains during the MJ and JA bimonthly periods (Fig. 3.8). During these bimonthly periods, the Great Plains experience heavy convection and propagating mesoscale convective systems (MCS), which contribute significantly to the total rainfall in these seasons (Fritsch et al., 1986). DeMott et al. (2007) discussed issues in creating heavy convection in the CAM3 model, particularly in the Great Plains. They found that the diurnal cycle in the CAM3 model was too strong and the timing of convection was too early. They used sub-daily observations and model output to identify the mechanisms involved, and found that the necessity for the model to consume CAPE within an hour long convective adjustment time-scale, as well as the condition that plumes must detrain at the level of minimum moist static energy, resulted in convective plumes that were too high and included too little entrainment. As a result, the convection occurred too quickly (DeMott et al., 2007). This then caused the model to be unable to build up moisture and larger CAPE values that would be necessary for heavy rainfall at a later time in the day (DeMott et al., 2007). The inclusion of entrainment in the calculation of CAPE in the newer model versions may have helped but not solved these issues with the parametrization scheme, resulting in an improved representation but still a continued bias in the model's heavy precipitation during the MJ and JA seasons.

To investigate whether this issue with convective parametrization is perpetuated in the newer model version, the phase and magnitude of the diurnal cycle are examined using 3-hourly precipitation from the CAM3, CAM4, and CAM5 models in comparison to 3-hourly satellite precipitation estimates from the Tropical Rainfall Measuring Mission v.7 (TRMM) from the National Aeronautics and Space Administration (Huffman et al., 2007). Results for the CAM5 model are also shown at a higher resolution, 0.23x0.31°lat-lon, referred to as

0.25°. We expect representativeness errors will only impact the magnitude of the diurnal maximum but not the timing of maximum convection, so the 0.25° data is not remapped to the 1° resolution. Results are shown for the time period of 2001-2010 except for the CAM5 0.25° model where a common time period was not available. The CAM5 0.25° model analysis is shown for 2001-2005, a time period of the same length and overlapping as many years as possible with the other products 1996-2005. We found little change to the phase and amplitude when using alternate sets of earlier 10-year analysis periods. The phase is computed as the time of the peak in the first harmonic of the diurnal variation and the magnitude is the mean precipitation over all days. Comparing the diurnal timing from CAM3 to CAM4 run on the same dynamical core as the 1° resolution shows a reduction in the magnitude of the diurnal cycle over the US, but no clear improvements in the timing of the diurnal maximum (Fig. 3.9). There are some minor improvements in the central US in the CAM5 (Fig. 3.9), but the diurnal timing issue persists.

In the CAM3 model, Dirmeyer et al. (2012) showed that increasing the resolution of the GCM did not resolve the diurnal timing problem so long as the precipitation was still parameterized. This is also seen in the CAM5, where increasing the resolution from 1° to 0.25° does not improve the timing issue over most regions, notably in the Southeast (Fig. 3.9). Over the Rocky Mountain region there is an area of later phase that develops at higher resolution, this error is found in many other orographic regions in the model at high resolution (Bacmeister et al., 2014).

Dirmeyer et al. (2012), did find that the CAM3 with an embedded two-dimensional cloud resolving model, known as the super-parameterized CAM3 model (SP-CAM), did have better timing of their diurnal precipitation maximum (Dirmeyer et al., 2012). In a newer version of the model with embedded cloud resolving model, SP-CAM3.5, Pritchard et al.

(2011) were even able to produce propagating systems in the Great Plains much like MCS's found in observations. These results are consistent with the idea that issues with heavy precipitation in the plains during the summer are due to issues with the parametrization of convection. Although the SP-CAM3.5 does have many other issues with the representation of precipitation, such as an overproduction of intense precipitation (Iorio et al., 2004) and some remaining timing issues (Dirmeyer et al., 2012), it is nonetheless illustrative and encouraging to see that a model with explicit convection has some ability to produce MCS's.

Heavy precipitation in the Gulf Coast during the JF, MA, and ND bimonthly periods is simulated in both the CAM5 and the CCSM4, but the magnitude is much too low and often displaced farther towards the East Coast (Fig. 3.8). There are many different precipitation mechanisms responsible for extreme precipitation at this time of year and so it is difficult to speculate as to the source of the error.

Another glaring issue in the model representation of extremes occurs in the SO season in the Gulf Coast and along the East Coast of the US (Fig. 3.8). Tropical cyclones are responsible for up to a quarter of September precipitation in these regions (Knight and Davis, 2007). It is well established that GCMs at standard resolutions have severe issues with the production of tropical cyclones and when they are produced, they are generally much weaker than in observations. It is possible therefore that these errors are associated with errors in the production of tropical cyclones in the model.

To put the errors in extreme precipitation in perspective, we compare climatological annual extreme precipitation in the NAAP, GPCP, CFSR, CAM4 (not shown), CAM5, and CCSM4 (Fig. 3.10). We see that errors in the CFSR are generally the smallest, for the absolute value of the percent difference they are within 0-20% in central and eastern

Canada/US, much greater (30-60%) in the US Rocky Mountains, and in some areas in the Canadian Rockies and around Hudson's Bay up to 80% (Fig. 3.10c,d). The errors in the GPCP are typically higher (0-40%) in most of the US (Fig. 3.10a,b). The GPCP has a distinct change in the errors at 40°N, where the input data for the GPCP changes from the TMPI (south) to TOVS (north). South of 40°N the GPCP, in particular in the South West, there are larger extremes with errors ranging from 10% up to 100%, while north of 40°N the extremes are generally smaller (up to 40%) except along the West Coast which approach 60%. The creators of the GPCP have noted large errors when the GPCP is used at the daily frequency provided and have suggested that the errors decrease when it is temporally averaged (Huffman et al., 2001).

The GCMs have some large errors in the Rocky Mountains and West Coast (60-100%), similar in pattern to the CFSR (Fig. 3.10). A central difference between the CFSR and the models is in the South Eastern and Central US, where there are errors between 20-60%, which as discussed previously are likely due to issues with the representation of convection. Errors in extreme precipitation in the CAM4 (not shown) are very similar to the CAM5 and CCSM4. Although the locations of the errors are different, the magnitude of errors in extreme precipitation in the GPCP and the models are on the same order which implies that the models are within observational error (Fig. 3.10). However, given the known errors in the GPCP at daily resolution and the highly visible differences in the error field at the location of the data transition in the GPCP previously discussed, these results imply that caution should be exerted when using the GPCP to evaluate extremes. It should be noted that errors in the CFSR typically have a similar pattern to those in the GCMs, as such using the CFSR for validation could result in an underestimation of errors in GCMs.

In addition to examining errors that exist in the current version of the model, it is important to determine what improvements if any there are over the previous version of the model. Gent et al. (2011) show that the distribution of precipitation is much better represented in the CCSM4 than the CCSM3 in the tropics, even when the CCSM4 is run at lower resolution, however it has not yet been shown how the distributions compare in the midlatitudes. Using the SCRIP remapping procedure once again, we remap both the NAAP and the CCSM4 data onto the lower resolution CCSM3 T85 grid (approx. 1.4°lat-lon) over the 1979-1999 period and examine similar metrics as above. Comparison between the CCSM3 and CCSM4 median precipitation errors with respect to the NAAP reveal that there is a notable reduction in excess precipitation over the northern East Coast but over much of the rest of the domain there is little to no improvement or in some cases a small increase in error in the representation of the median precipitation in the CCSM4 (Fig. 3.11). For the extreme precipitation, we do see modest improvements in the Southeastern US as well as the West Coast (Fig. 3.11).

3.5 Conclusion

Although it is well known that precipitation observations and reanalysis can have some large errors, the traditional assumption has been that these errors are small relative to those in the precipitation produced by a GCM. As the representation of precipitation in GCMs improves however, we find that errors in model precipitation are approaching these observational errors and so they must be carefully considered. Results from Gervais et al. (2014b) related station density to errors in gridded station measurements and suggest the potential for large errors in gridded precipitation station analysis when station density is low. Applying this relationship between errors and station density found in Gervais et al. (2014b) to the NAAP dataset, we find the potential for large errors exists in the mountainous regions of the Western US, as well as in the majority of Canada. A general bias in the models towards negatively skewed precipitation in Northern Canada with respect to the NAAP was interpreted as an error in the NAAP since intercomparison with the other reference sources all had the same bias. We also see large changes in the GPCP at the border of its data change. Changes in the skewness and extreme precipitation across this border can be of the same magnitude as errors in the models. This implies that the GPCP for some metrics, the extremes in particular, can be as biased as the models and thus should be used with caution. The errors in the CFSR generally have the same pattern as the GCMs and so when validating against this data you are likely to see less errors than actually exist. These results support the viewpoint that in many cases the model error is approaching observational error and thus utilising several reference products to constrain these model errors is important.

CAM4, CAM5, and CCSM4 all had very similar biases in their representation of the distribution of precipitation. In general, the well known tendency of positive skewness in climate models is present in these models but only east of the Rocky Mountains. This coincides with regions that experience a larger portion of convective precipitation. Regions within and to the west of the Rockies generally have a more negatively skewed distribution than the NAAP, indicative a shift towards higher daily precipitation rates than that found in the observations. Errors in skewness are higher in the East than the West. Several locations have distributions that are very close to or fall between the various observations and reanalysis, which is very promising.

Examining the extreme precipitation for different bimonthly periods implicates different processes as sources of bias. In particular, there is a large underestimation of extreme precipitation in the Gulf Coast region in the winter and spring months. Heavy precipitation is also underestimated in the spring and summer from the Gulf Coast through the Great

Plains. These types of errors were seen in previous versions of the model and were attributed in those cases to issues with the convective parametrization and an unrealistic representation of the build-up of CAPE. An analysis of the phase of diurnal precipitation for various version of the CAM model reveal that these issues with diurnal timing are ongoing in the newer versions of the model and are not remedied by increasing the resolution from 1° to 0.25°. A final notable issue with model's extreme precipitation is the lack of heavy precipitation in the SO period from the Gulf Coast inland and up the eastern seaboard. Although this is likely not the only source of errors in this region, this error is attributed in part to a lack of extreme precipitation from tropical systems as they are not well resolved in the model.

When errors in the CCSM3 to the CCSM4 were compared by Gent et al. (2011) in the tropical regions they found large improvements in the representation of the distribution of precipitation. However, when comparisons are made in North America using the metrics in this study we find the gains in the representation of the CCSM4 to be minimal. There are many potential reasons of which one contributing factor may be the continued issue with convective parametrization in the model.

When examining output of future climate model runs, we can use these results to inform us of which processes we can and cannot expect the CCSM model to adequately produce. This study focused on the US and Southern Canada, however this area contains a wide range of precipitation climatologies that may be useful in understanding GCM prediction of precipitation in other mid-latitude regions. Although the CCSM models are doing relatively well in producing an adequate distribution in many locations, they do have some difficulty in producing extremes with higher magnitudes. Our confidence in their abilities to represent future changes in these extremes is therefore low, but for the production of larger-scale precipitation processes it is higher.

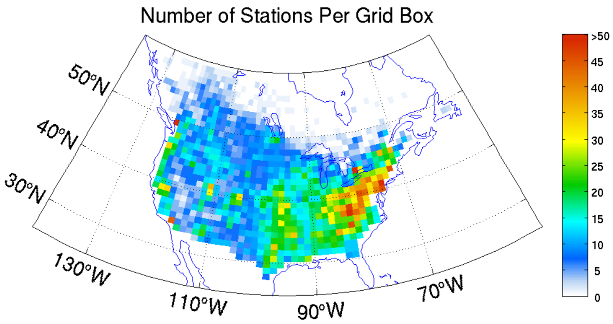

Figure 3.1: Number of stations per CCSM4 grid box (0.9°x1.25° lat-lon), averaged over the years 1975, 1985, and 1995. Values are rounded to the nearest integer.

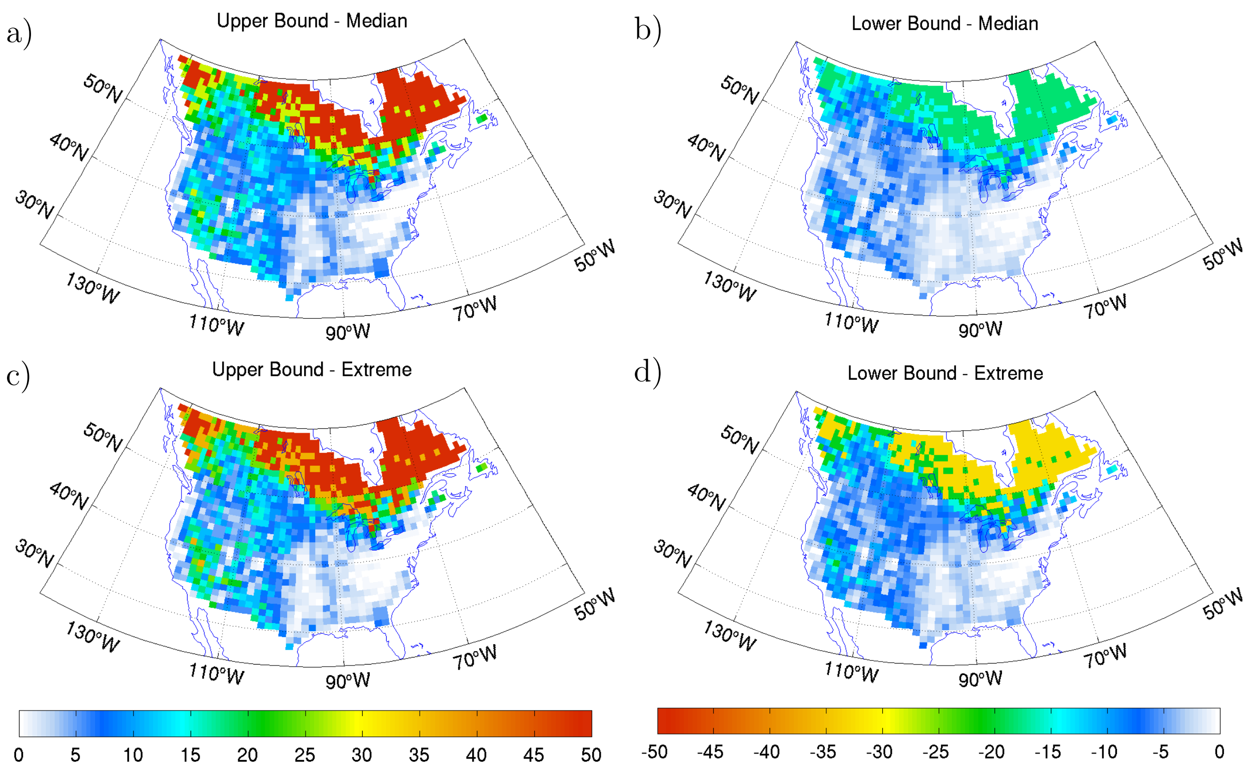

FIGURE 3.2: Upper (a,c) and lower (b,d) bound on the percent bias in climatological annual median (a,b) and extreme (c,d) precipitation for the NAAP data using an experimentally derived relationship between upper and lower errors bounds and station density found in Gervais et al. (2014b). Note that the color scales are reversed between the upper and lower bound maps such that the magnitude of the color schemes are identical but in opposing directions.

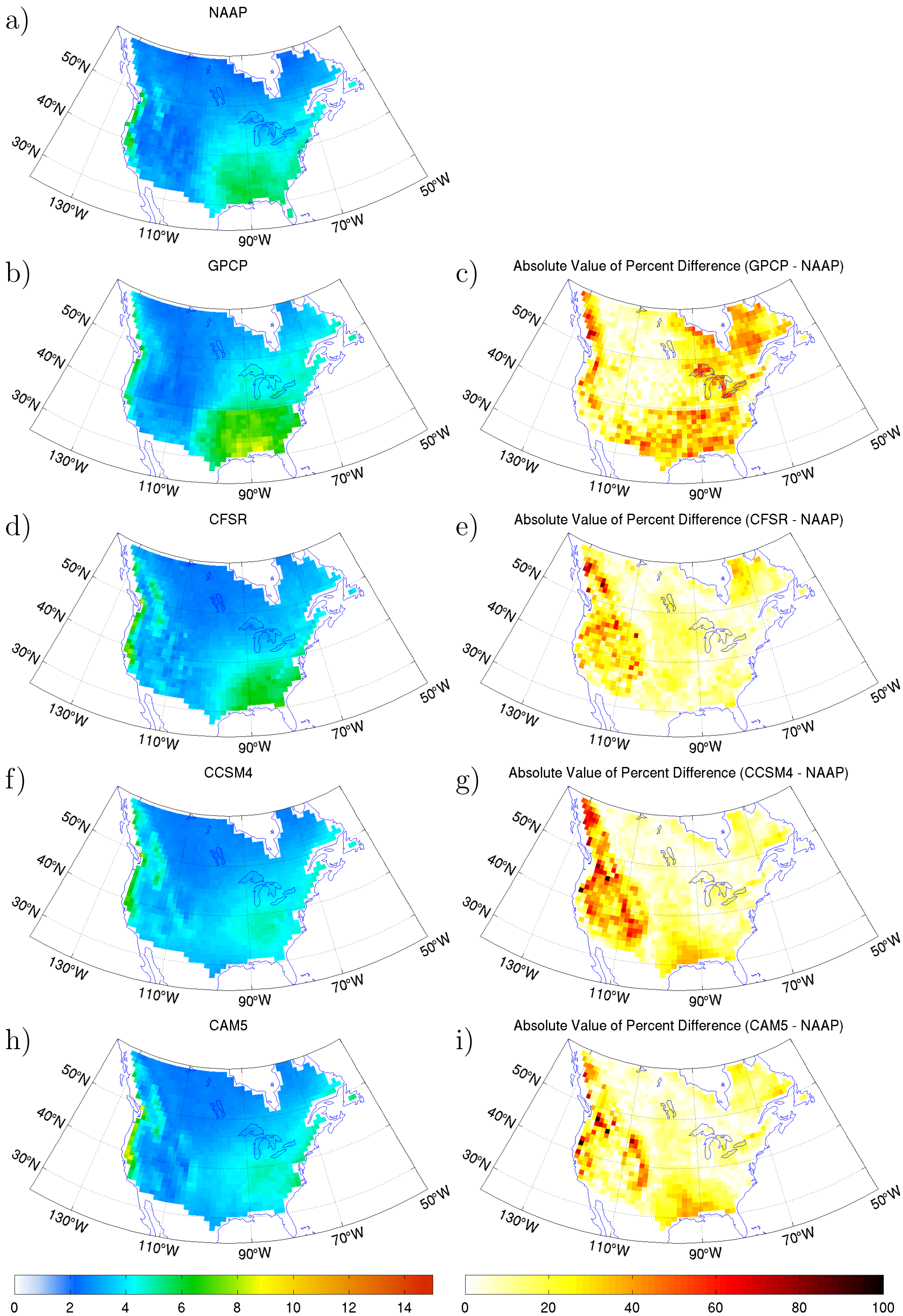

Figure 3.3: a) Climatological annual median precipitation (mm day^{-1}) for a) NAAP, b) GPCP, d) CFSR, f) CCSM4, and h) CAM5, and absolute value of percent anomaly relative to the NAAP (ex. $|[(GPCP - NAAP) \div NAAP] \times 100|$)) in climatological annual median precipitation (mm day^{-1}) for c) GPCP, e) CFSR, g) CCSM4, and i) CAM5.

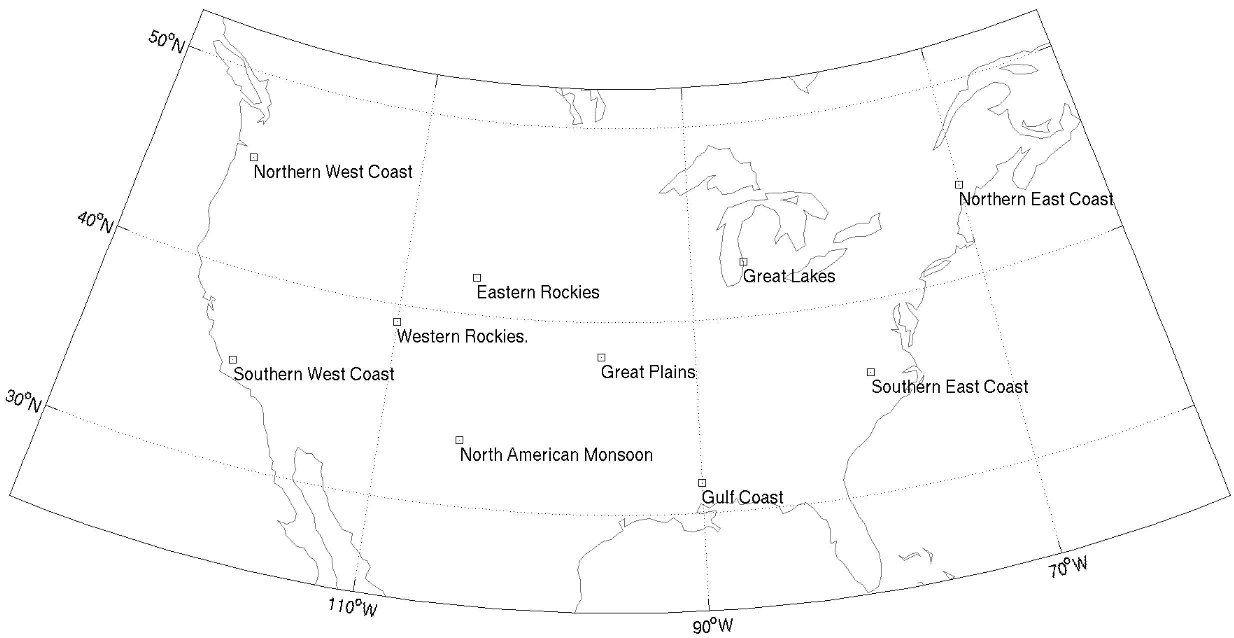

FIGURE 3.4: Location of grid points used to examine the distribution of precipitation

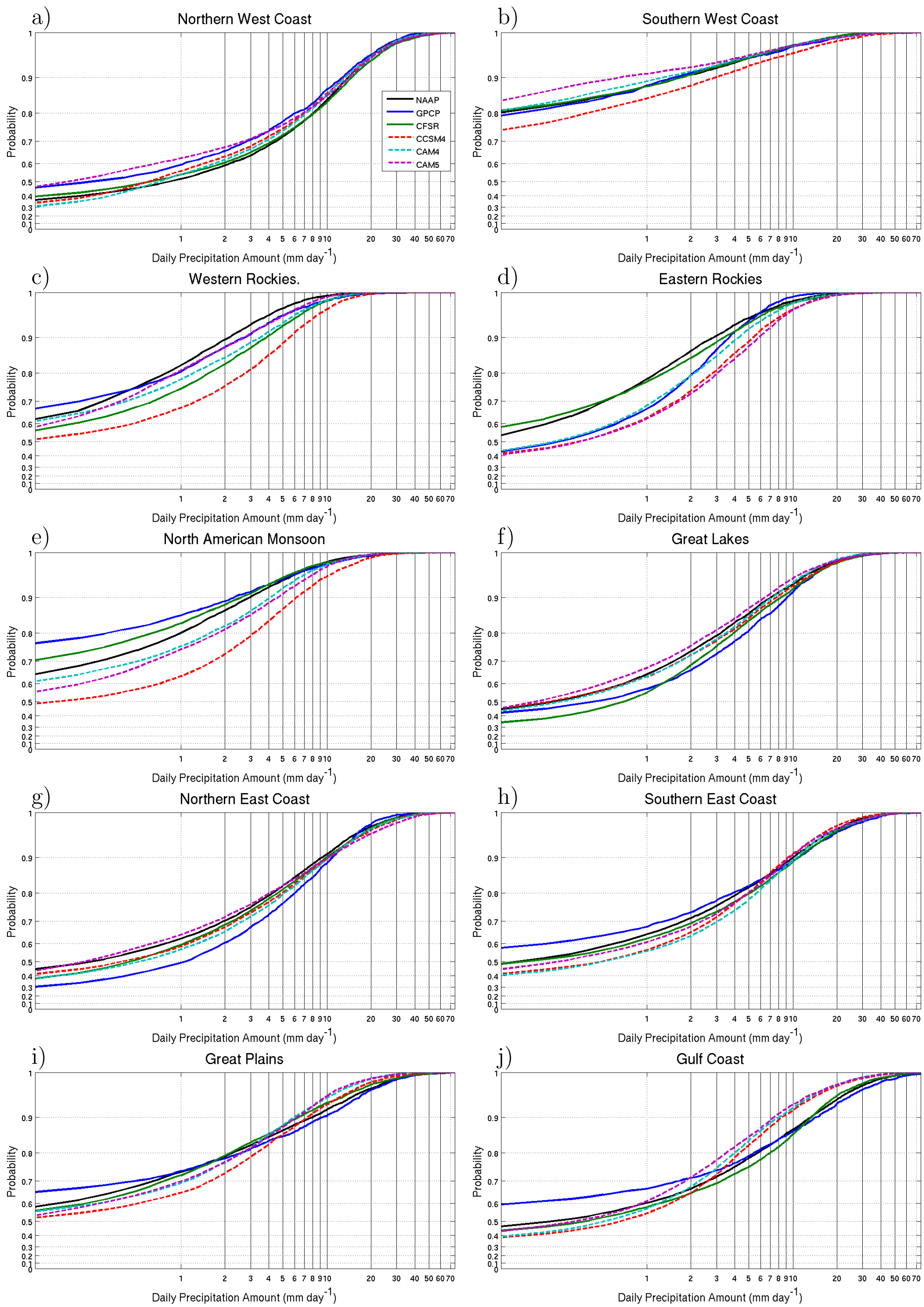

Figure 3.5: Climatologically averaged annual cumulative distribution function of precipitation frequency versus precipitation intensity (mm day^{-1}) over all days at point locations as indicated in Fig. 3.4.

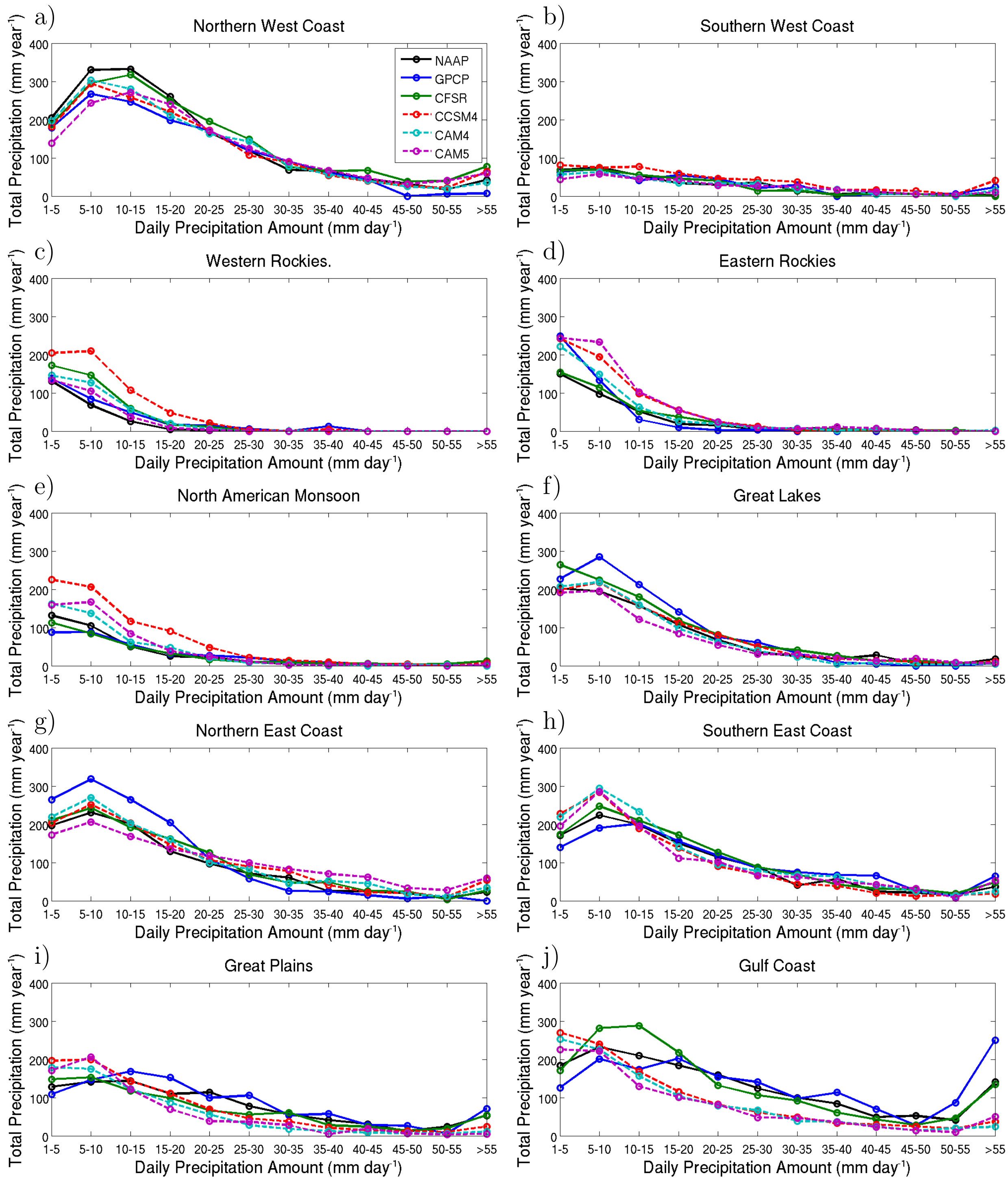

Figure 3.6: Climatological annual total precipitation (mm year^{-1}) versus precipitation intensity (mm day^{-1}) at point locations as indicated in Fig. 3.4.

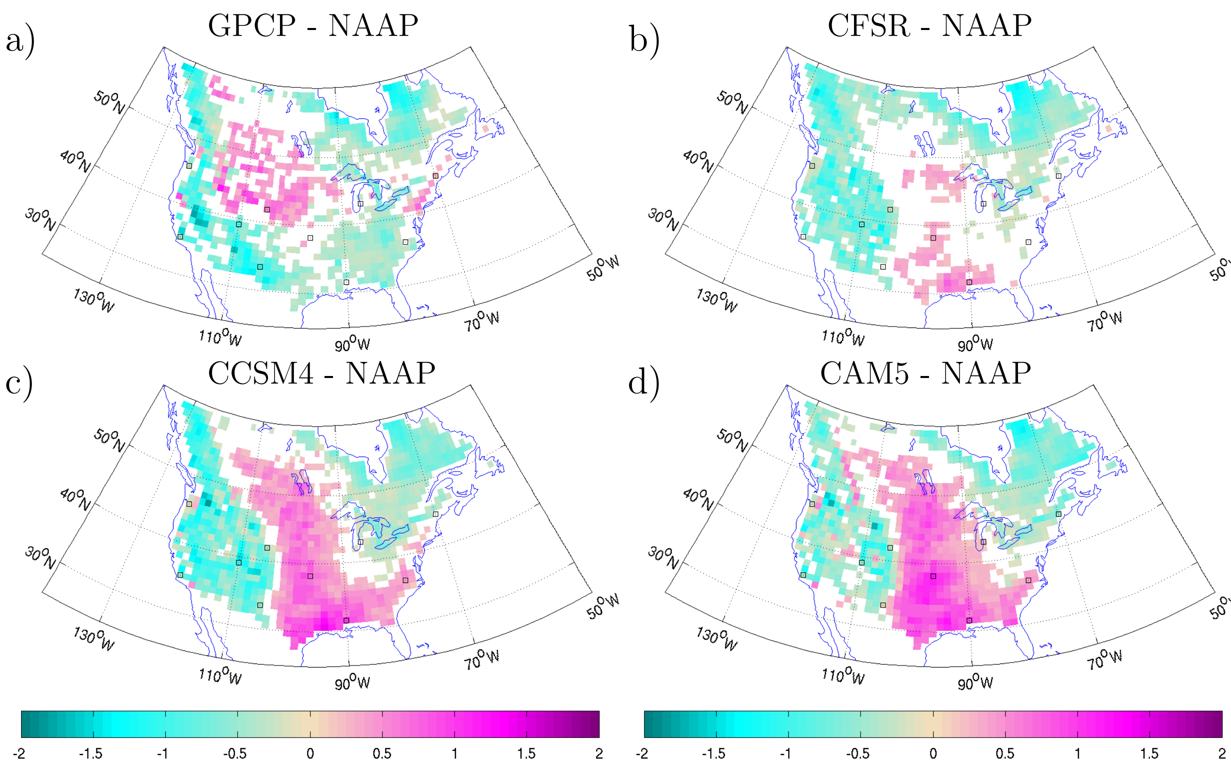

FIGURE 3.7: Anomalies relative to the NAAP (ex. GPCP - NAAP) of the skewness of the distribution of climatological annual total precipitation with respect to precipitation intensity, at each grid point, for the GPCP (a), CFSR (b), CCSM4 (c), and CAM5 (d). TMDs that are found to not be significantly different from the NAAP, using a monte carlo test, are white. Locations shown in figure 3.4 are included for reference and shown as open squares.

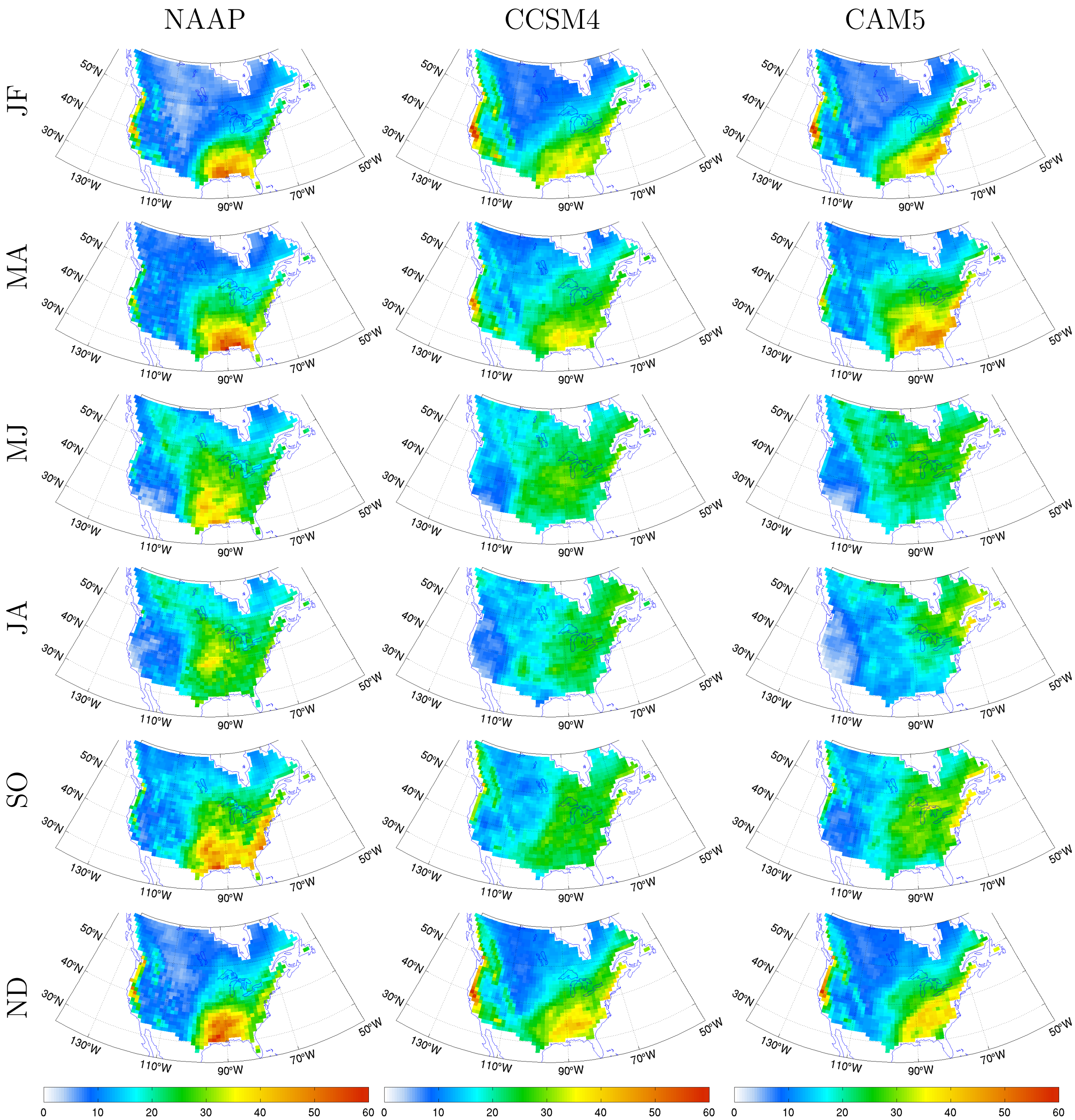

Figure 3.8: Climatological (1979-2005) extreme precipitation (mm day^{-1}) for (left) NAAP, (middle) CCSM4 and (right) CAM5 in bi-monthly periods: January and February (**J**F), March and April (**M**A), May and June (**M**J),July and August (**J**A), September and October (**S**O), and November and December (**N**D).

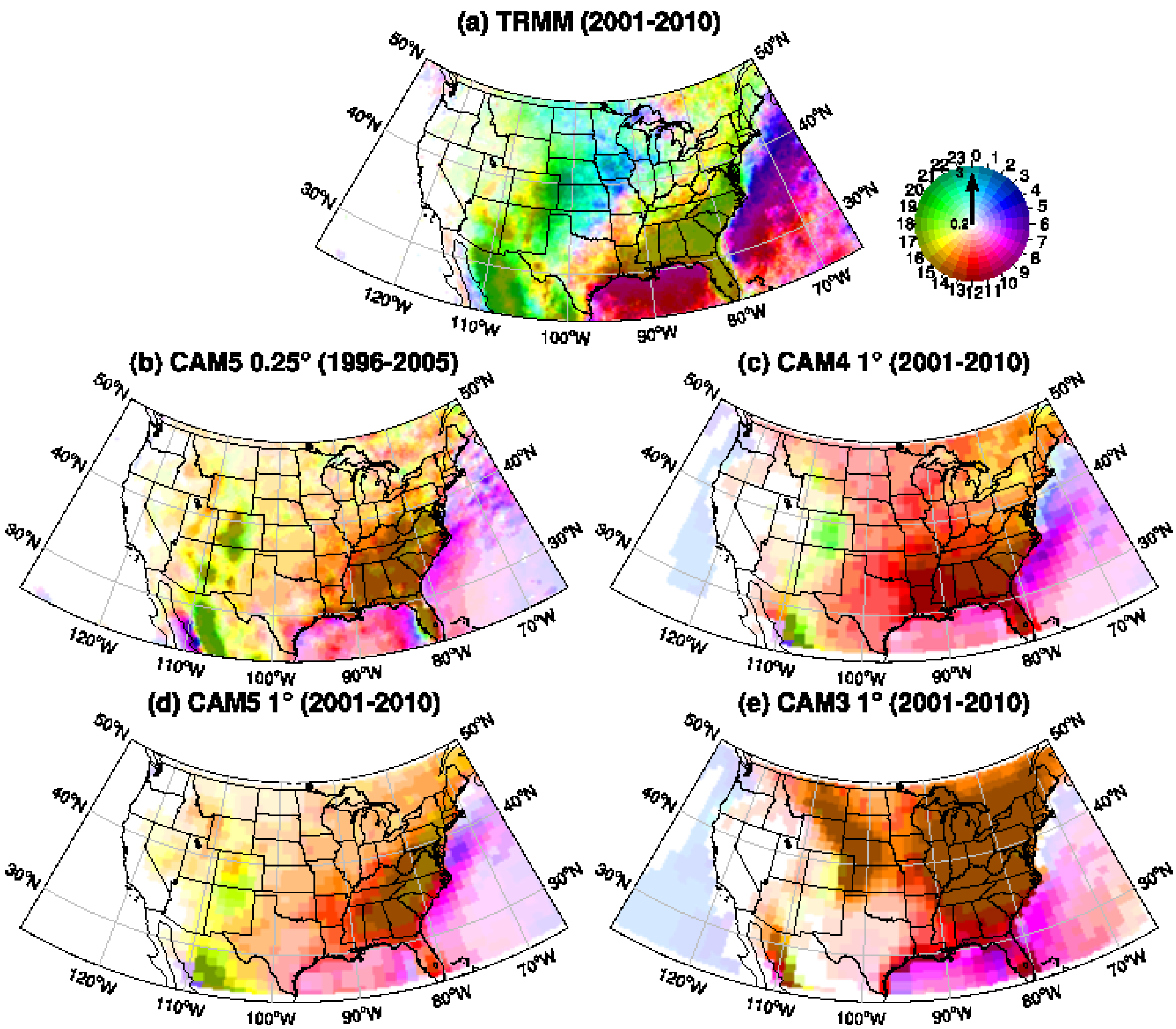

FIGURE 3.9: Local time of first harmonic of JA diurnal precipitation (color hue) in the TRMM (a), CAM5 0.25° (b), CAM4 1° (c), CAM5 1° (d), and CAM3 1° (e). Color intensity represents the mean daily precipitation (mm day^{-1}) begining at 0.2mm day^{-1}. The observation period is 2001-2010, except the CAM5 0.25° where it is 1996-2005.

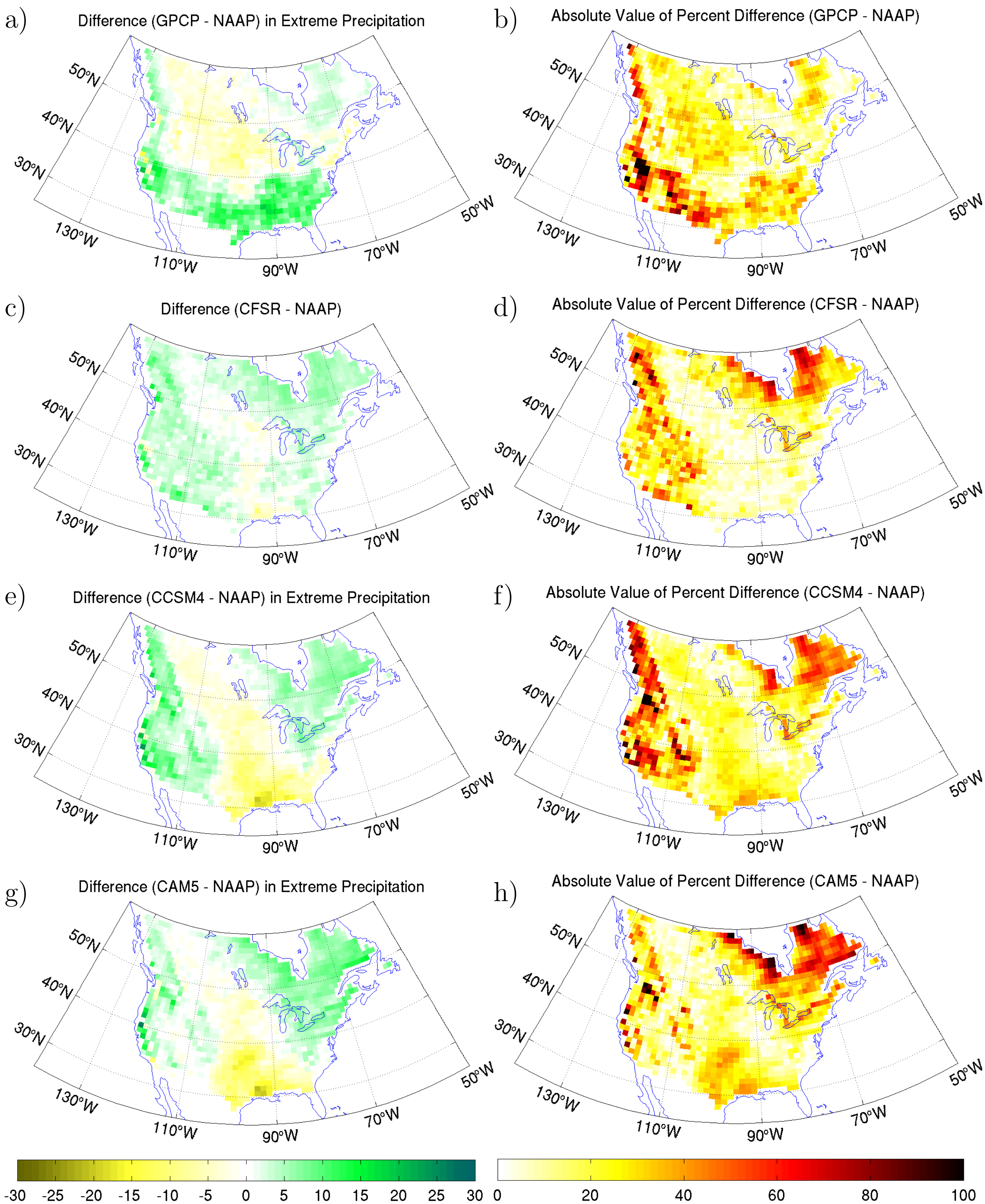

Figure 3.10: Anomalies (a,c,e,g) and absolute value of percent anomalies (b,d,f,h), relative to the NAAP, for the GPCP (a,b), CFSR (c,d), CCSM4 (e,f), and CAM5 (g,h) climatological (1979-2005) annual extreme precipitation (mm day^{-1}). Anomalies are computed, for example as (GPCP - NAAP), and absolution value of percent anomalies, for example, as $|[(GPCP - NAAP) \div NAAP] \times 100|$)

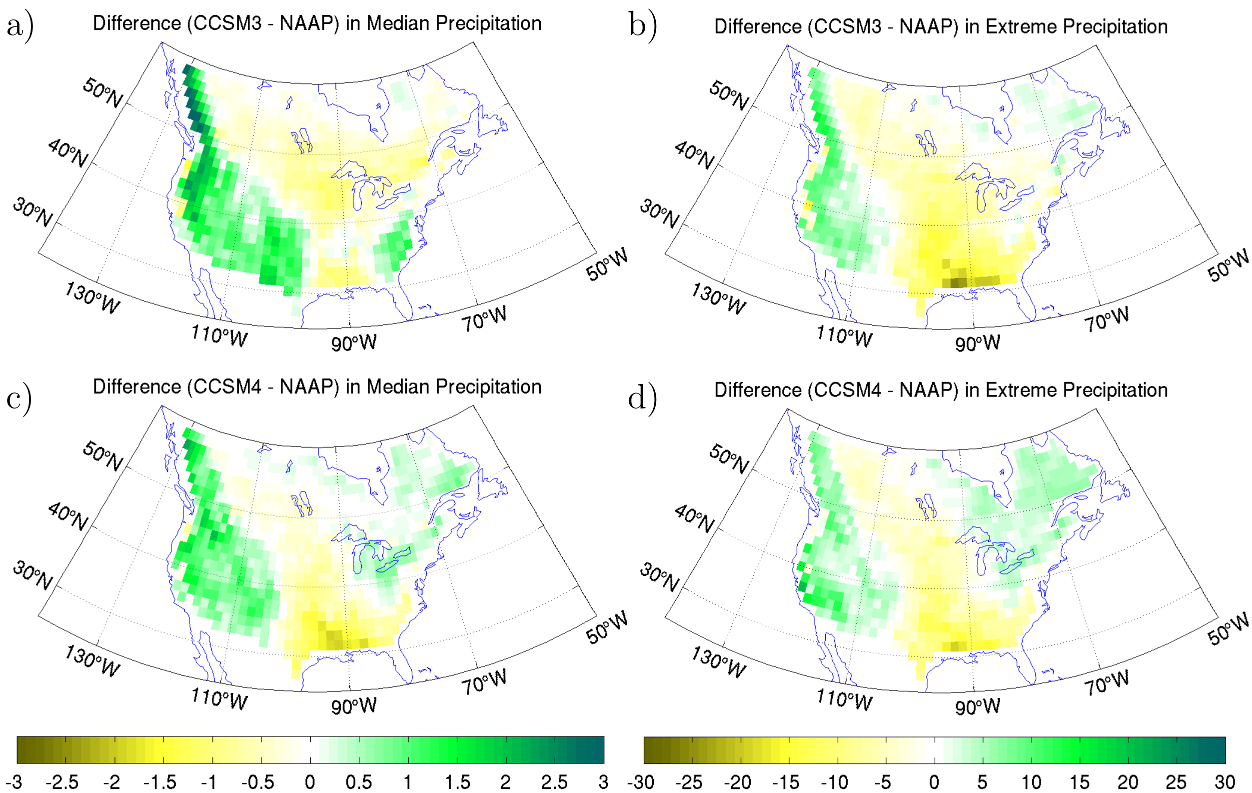

FIGURE 3.11: Anomalies relative to the NAAP, for the CCSM3 (a,b) and CCSM4 (c,d) of climatological (1979-1999) annual median (a,c) and extreme precipitation (b,d) (mm day^{-1}). All data is remapped onto the CCSM3 resolution and anomalies are computed for example as CCSM3 - NAAP.

Chapter 4

Arctic Airmasses in a Warming World

This chapter represents the beginning of a planned series of papers on how climate change will impact sensible weather, namely air masses and precipitation. The recent availability of the Community Earth System Model Large Ensemble (CESM-LE), provides 30 realizations of the future climate. This variability is vital for the measurement of changes in the distribution of daily weather. The approaches I propose for the examination of changes in variability differ between precipitation and air masses. A unifying concept for both variables is to examine higher order statistics to help define climate from a weather perspective.

This current chapter examines how patterns of winter Arctic air masses will change in the future, using output from the CESM-LE project. A method of self-organizing maps is used to identify patterns of variability and their changes. Composites of various fields atmospheric variables provides a comprehensive view of the sensible weather associated with these representative patterns. Dynamical mechanisms are then suggested to explain the changes in their frequency of occurrence.

Precipitation has a wide distribution of daily amounts that define its climatology. Since it is often a localized and discontinuous field with a wide range of spatial patterns of variability, a technique such as SOM analysis may be less appropriate for its representation. In a final planned paper, the analysis of precipitation distribution in Chapter 3 will be expanded upon to examine future changes in the distribution of daily precipitation amounts in various regions. An analysis will also be conducted to assess the impact of internal variability on extreme precipitation validation. This will be accomplished by comparing extreme precipitation between individual runs of the CESM-LE, in order to mimic issues with comparing observational data to GCM output.

The current and planned chapter together provide an account of the potential changes in sensible weather, namely precipitation and air masses. The planned chapter on changing precipitation distribution has been left as a subject for future work.

Abstract

An important aspect of understanding the impacts of climate change on society is determining how the distribution of weather regimes will change. We know that Arctic amplification results in greater warming over the Arctic compared to the midlatitudes and in this study we are further interested in how patterns of Arctic air masses will be affected. We employ the Community Earth System Model Large-Ensemble (CESM-LE) RCP 8.5, consisting of 30 ensemble members run through the 21st century. This large ensemble provides the realizations necessary to define the mean climatology for each year, from which an equivalent potential temperature at 850hPa (θ_{e850}) anomaly field with respect to a changing climate is created. Self-organizing maps are used to define archetypes of this θ_{e850} anomaly field and assess changes in their frequency of occurrence over the 21st century. Our results show a pattern with negative θ_{e850} anomalies situated over the central Arctic is becoming less frequent with time. There is an increase in the frequency of patterns with either positive or negative θ_{e850} anomalies over North America, associated with more intense ridges and troughs in the 500hPa flow. We hypothesize that the increase in frequency of such patterns is the result of enhanced forcing of baroclinic waves owing to reduced sea ice over the western Arctic. There is also a decline in patterns that have anomalously high θ_{e850} over the North Atlantic, a pattern that is associated with intense ridging in the 500hPa flow over the North Atlantic and colder θ_{e850} over Europe. We relate the decrease of these patterns to an enhancement of the North Atlantic jet induced by a warming deficit in the North Atlantic Ocean.

4.1 Introduction

With global climate change both historical observations (Serreze et al., 2009; Screen and Simmonds, 2010) and future climate modeling studies (Holland and Bitz, 2003; Kay et al., 2012) predict a rise in global temperature that is larger over the Arctic than the midlatitudes, known as Arctic amplification. However, society is not only concerned with the average future climate change, but also how this will be manifested as the daily weather people experience. Will regimes of cold temperatures over the northeastern United States and eastern Canada that typified the winters of 2013-14 and 2014-15 become more common in the future? Can we expect a cold European winter pattern similar to that of 2012-13 to occur more often in the future? These questions cannot be addressed through an examination of the average change in temperature. They require an understanding of the variability of air mass patterns and how these will change in the future. Of particular importance is the formation of Arctic air masses and their associated changes in the mid-latitude flow.

Arctic or Polar continental air masses are cold and dry air masses generally associated with deep and persistent surface inversions (Curry, 1983). These inversions are the result of effective radiative cooling over highly emissive snow and sea ice covered surfaces, and are enhanced due to radiative cooling from ice crystals through the depth of the column (Curry, 1983). In general the maximum cooling for the formation of Arctic air masses occurs over land due to ocean heat conduction through sea ice (Curry, 1983). These air masses can be advected into the midlatitudes to create cold air outbreaks (Walsh et al., 2001). For example, Walsh et al. (2001) demonstrated that cold air masses in midlatitude North America originate from Northern Canada, the Central Arctic, or Asia.

The observed (Serreze et al., 2009) and predicted (Kay et al., 2012) vertical structure of Arctic amplification has the largest increases at the surface and decreasing with height. Therefore polar amplification implies a reduction in the strength of surface inversions typical of Arctic air masses. There are several positive feedbacks responsible for Arctic amplification, the most important being surface albedo and lapse rate feedbacks (Pithan and Mauritsen, 2014; Graversen et al., 2014). As the fraction of surface area covered by highly reflective sea ice and snow declines, they are replaced by open ocean and land with a lower albedo resulting in enhanced absorption of heat at the surface and thus more melting (Manabe and Wetherald, 1975). The positive lapse-rate feedback in the atmosphere is caused by the existence of a surface temperature inversion, which confines the Arctic warming to the lower levels (Manabe and Wetherald, 1975) and requires a larger surface warming to balance changes in radiation at the top of the atmosphere (Pithan and Mauritsen, 2014).

The goal of this work is to expand upon our understanding of climatological changes in Arctic air masses owing to Arctic amplification and examine how their variability may change in the future. To address this problem, we employ a 30 member ensemble of future projections from the Community Earth System Model Large Ensemble (CESM-LE) fully coupled model. This new large ensemble allow us to examine changes in the internal variability of air mass patterns, providing the equivalent of 30 years of climatological variability for each model year. To represent Arctic air masses we use the January-February (JF) equivalent potential temperature field at 850hPa (θ_{e850}) North of 50°N, a measure of both temperature and moisture. To identify relevant patterns, we use a self-organizing maps technique, which allows us to both identify archetypes of θ_{e850} anomaly patterns and examine how their frequency of occurrence changes through time. The combination of the large ensemble data and the self-organizing maps method allows us to separate out the forced climate change signal from changes in internal variability. This allows us to answer the question of how patterns of air masses will change in the future. Furthermore, there will be implications on flow regimes such as the Arctic Oscillation and mid-latitude planetary waves, which may impact the formation and movement of these air masses and are likely to experience changes in the future.

4.2 Data and Methods

4.2.1 Data

This study utilizes data from the CESM large ensemble (CESM-LE) RCP8.5 for 2006-2080, consisting of 30 ensemble members (Kay et al., 2014). Each ensemble member represents a realization of the future climate and together the 30 members provide a wide range of potential solutions that differ only due to internal variability of the climate system. This is an advantage over multimodel ensembles where different physics are represented in addition to internal variability. Details regarding the CESM-LE experiment can be found in Kay et al. (2014).

The Community Earth System Model (CESM) is the most recent version of the National Center for Atmospheric Research's global coupled model comprised of 4 component models, the Community Atmosphere Model 5 (CAM5), the Parallel Ocean Program version 2 (POP2), the Community Ice Code (CICE4), and the Community Land Model 4 (CLM4) (Hurrell et al., 2013). The component models are identical to the previous model version, the Community Climate System Model 4 (CCSM4) (Gent et al., 2011), except for the atmospheric component (Hurrell et al., 2013). CAM5 has undergone several improvements from the previous version CAM4, including increased vertical resolution from 26 to 30 levels, new parameterization schemes for moist turbulence scheme and shallow convection, and changes to the cloud microphysics scheme (Neale et al., 2010). Of significance for the Arctic are the resulting improvements in the representation of the total cloud percentage (Barton et al., 2012; Kay et al., 2012).

A comprehensive analysis of the representation of the Arctic in CESM has yet to be conducted as it was by De Boer et al. (2012) for CCSM4. De Boer et al. (2012) find that CCSM4 generally represents the patterns of surface air temperature with a small negative bias on the order of -2K. They do find a significant negative bias in SLP over the Arctic, resulting in a weaker Beaufort High than is observed (De Boer et al., 2012). This influences the Beaufort Gyre leading to errors in sea ice motion (Jahn et al., 2012). Otherwise, the Arctic sea ice in CCSM4 compares well with observed sea ice in terms of concentration and thickness (Jahn et al., 2012). Preliminary results show that the negative SLP bias over the Arctic is corrected in CESM, however there are still issues with the Beaufort high being situated closer to the Eurasian coast than in the observations (Personal Communication with Patricia DeRepentigny). CESM has a similarly well simulated Arctic sea ice cover, but experiences more rapid sea ice loss than the previous model version, presumably as a result of improvements to the cloud parameterizations and their resulting improvement of Arctic surface temperature (Personal Communication with Alexandra Jahn).

In this study, Arctic air masses are represented by patterns of equivalent potential temperature at 850hPa (θ_{e850}) north of 50°N. θ_{e850} is the temperature an air masses would have if it were lifted to the lifting condensation level, condensing out all of its moisture, and compressed adiabatically to a reference pressure (1000hPa) (Holton, 2004, pg. 290). As such, it is conserved under adiabatic motion. It is a good metric for air masses since it integrates both temperature and specific humidity, which are used to distinguish between air mass type. The number of vertical levels in CESM-LE that are archived is limited and so θ_{e850} is estimated using a simplified form as follows:

$$\theta_e = (T + \frac{L_v}{c_{pd}} \cdot \frac{q}{1-q})(\frac{P_0}{P})^{\frac{R}{c_{pd}}} \tag{4.1}$$

where T is temperature (K) at 850hPa, P = 850hPa, q is specific humidity, the latent heat of evaporation $L_v = 2.4 \times 10^6 \mathrm{Jkg}^{-1}$, the specific heat for dry air at constant pressure c_{pd} = 1004 $\mathrm{Jkg}^{-1}\mathrm{K}^{-1}$, the specific gas content R = 287.04 $\mathrm{Jkg}^{-1}\mathrm{K}^{-1}$, and the reference pressure P_0 = 1000hPa. All analysis is conducted for the months of January-February (JF) when we have the coldest temperatures.

4.2.2 Self-Organizing Map Algorithm

The self-organizing map algorithm uses competitive machine learning to represent the probability density function of a dataset using a two dimensional grid of map nodes. The method allows for the classification of large volumes of data into a pre-determined number of archetypes that are organized based on their similarities. Since its introduction by Kohonen (1982), the SOM algorithm has been applied in a variety of different disciplines and is gaining popularity in the atmospheric sciences (Huth et al., 2008). It has been used to investigate synoptic circulations associated with extreme events, such as Cassano et al. (2006a) a study of extreme temperature and winds in Barrow Alaska and Cavazos (2000) who examined extreme precipitation in Northeastern Mexico/Southeastern Texas. The SOM algorithm can also be used as a novel method for the validation of model variability, through comparison between observation and model SOM node frequencies (Schuenemann and Cassano, 2009). In a climate change context, the method has also been applied to demonstrate changes in patterns and variability in GCMs run with future climate scenarios (Schuenemann and Cassano, 2010; Cassano et al., 2006b). An extended discussion on the application of SOMs for synoptic climatology can be found in Hewitson and Crane (2002).

The SOM algorithm is an iterative process by which input data is used to train a SOM map that represents the data's distribution. The input data are first normalized, then multiplied by the cosine of the latitude to take into account the variation in grid box size with latitude. This way grid boxes with smaller area or greater variance do not have a disproportionately larger influence on the analysis. The user defines a SOM size that determines the number of map nodes or patterns to represent the data. For example, the final SOM size chosen for this study (after various testing) is a 3x5 giving a total of 15 nodes. The SOM map nodes are then initialized with random data prior to node training.

The SOM training algorithm proceeds by repeated comparison of input data vectors to the SOM map nodes. For example, the data vectors in this study are daily maps of θ_{e850}. A best match unit (m_i) is determined to be the map node that has the smallest Euclidean distance to the input data vector (x_i). The best match unit and surrounding nodes are then updated as follows:

$$m_i(t+1) = m_i(t) + \alpha(t) \cdot h_{ci}(t) \cdot (x(t) - m_i(t)) \tag{4.2}$$

where t is the training time, α is the learning rate parameter, and h_{ci} is the neighborhood function. The learning rate parameter defines the amount by which the map is updated, which in this study is an inverse function of training time (Vesanto et al. (2000), Kohonen (2001) pg.145). The neighborhood function h_{ci} represents the shape of the influence. There are several commonly applied neighborhood functions, here we use the Epanechikov function, which was shown by Liu et al. (2006) to outperform other common radius functions in simplified tests. The Epanechikov function is:

$$h_{ci} = max(0, 1 - \frac{d^2}{r^2}) \tag{4.3}$$

The map distance to the best match unit is d, where adjacent map nodes have a distance of 1. The radius of influence (r) is the maximum distance away from the best match unit where the input data still has influence. The shape of h_{ci} is maximized at the best match unit and decreases to zeros at the radius of influence. It is good practice to begin the training with a radius of influence equal to the diameter of the SOM to ensure that all nodes are updated and decrease the value with training time (Kohonen, 2001). The SOM map may be trained in multiple training steps and it proceeds for some multiple of the total number of data vectors, which in this study is the total number of days. Further details on the SOM algorithm can be found in Kohonen (2001) and software are freely available (Vesanto et al. (2000), http://www.cis.hut.fi/research/som-research/).

The greatest advantage of using SOMs over the more traditional analysis of Empirical Orthogonal Functions (EOF), is the lack of restrictions of orthogonality and stationarity of identified patterns. Processes in the atmosphere are not always well represented by orthogonal patterns. This is the case for the θ_{e850} field, where as the first EOF represents only 7% of the variability. The use of a SOM can identify sets of non-orthogonal patterns in data that may be more physically relevant. Liu et al. (2006) demonstrated this in an idealized setting using a repeating set of non-orthogonal one-dimensional patterns. An EOF of this data produced one of the pre-defined patterns as the first EOF and a mixture of the other patterns as the second EOF. A SOM of the same data reproduced all four patterns. This blending of patterns, owing to the orthogonality constraint, has also been shown in two dimensions, both in an idealized setting (Reusch et al., 2005), and as applied to variability in the North Atlantic (Reusch et al., 2007).

Another issue that can compromise the utility of an EOF analysis is the impact of changing atmospheric patterns in time. Tremblay (2001) conducted an idealized study of the NAO with a shift in the Northern Center of action, similar to the regime shift in the mid 1970's. The results of this study showed a first EOF that was a North-South oriented dipole, consistent with the NAO, and the second EOF was an East West dipole. This study demonstrates that non-stationarity in atmospheric patterns can result in the generation of non-physical EOF modes. In contrast, Johnson et al. (2008) were able to identify the shift in centers of action of the NAO with time using SOMs. The SOM in Johnson et al. (2008) both identified NAO patterns that were N-S oriented and ones with patterns where the northern center of action was shifted to the east, as well as demonstrated the shift between the two as relative changes in the frequency of occurence of these patterns. This is an important result to consider when conducting analysis of atmospheric fields in a changing climate.

In comparison to other clustering methods, a useful trait of the SOM is the organization of the SOM map with more similar patterns being closer together. This is a product of the neighborhood function, which alters not just the winning map node but also the nodes within a given distance from the winning node. If the radius of influence in the neighborhood function were always one, there would be no topological ordering in the SOM and thus the SOM would be reduced to an adaptive K-means clustering method, as described in Murtagh and Hernández-Pajares (1995).

Although SOMs present several advantages over traditional methods, a drawback to the method is the large number of free parameters involved, which can lead to some subjectivity in producing a SOM map. The size of the SOM map is user defined and chosen so as to represent the distribution required for the study with the fewest number of patterns. Depending on the problem being studied, the SOM size could impact the patterns identified. In this study, increasing the size of the SOM maps resulted in the duplication of pre-existing patterns, indicating that the SOMs are robust with respect to size in their identification of important patterns.

There are also several tuneable parameters within the algorithm itself, such as the learning rate function, training length, and radius of influence. We conduct tests of these free parameters and choose SOMs based on measures of the quality of the SOM map produced. The Sammon maping algorithm (John, 1969) is a non-linear mapping from higher to lower dimension, which represents the euclidean distance between the map nodes onto a two dimensional field. Using this method, a Sammon map can be generated to determine topology or spatial relationship between map nodes. This provides information to how similar map nodes are to one another. A well constructed SOM should have a flat sammon map where the ordering of the map nodes is preserved (Kohonen, 2001). The quantization error (QE) is a measure of how similar the data is to the best match unit and is the average euclidean distance between a data vector and its best match unit (Vesanto et al., 2000). The topographic error (TE) is the percentage of data vectors for whom the second best match node is not adjacent to the winning node and is a measure of how well ordered the SOM map is (Vesanto et al., 2000). Gutowski (personal communication) has shown that during the training of a SOM map, over fitting of the SOM can result in lower QE at the expense of higher TE. In the creation of SOM maps in this study, the free parameters are chosen so that the resulting SOM has a balance of low QE, low TE, and a well ordered Sammon map. In such well constructed SOMs, we find that the general patterns identified by the SOMs are robust regardless of the tunable parameters chosen (not shown).

4.2.3 Creation of a Master SOM

In this study we are interested not only in the mean change in Arctic air masses, but also how the internal variability will change in the future. To isolate these changes in internal variability, we leverage the large number of ensembles to create a daily θ_{e850} anomaly field with respect to the changing climate. An annual JF ensemble average field is created to represent the changing climate. There are small year-to-year differences in the annual JF ensemble averages, indicating that internal variability has some remaining impact, even with the large ensemble. The anomaly field is computed as the daily θ_{e850} values minus the annual JF ensemble average, repeated for all years and ensemble members. A 3x5 master SOM is created using these daily θ_{e850} anomalies (Fig. 4.1). Tests with larger SOM sizes revealed similar patterns to the 3x5 but more duplicate patterns, and a reduction in the SOM size lead to the merging of patterns. Consequently, a 3x5 SOM was chosen so as to balance the need to fully represent the distribution of atmospheric patterns with the least number of maps possible.

Two sets of trainings are employed in the generation of the master SOM, the training length for each being 20 times the number of days of input data. With this training length, there is a balance between QE and TE and both are adequately small (not shown). The first and second trainings respectively, have radii of influence of 6 and 2, and alpha values of 0.5 and 0.1. The Sammon, a map is flat and its shape demonstrates that the bottom row of patterns are closer to one another and the top row are further away (Fig. 4.2). These measures of SOM quality demonstrate that the master SOM is well constructed.

It is worth noting that conducting SOMs on daily θ_{e850} anomalies relative to a decadal average for the 2010-2020, 2050-2060, and 2090-2100 time periods revealed similar patterns to the master SOM. The central differences were that the 2010-2020 SOM had some additional patterns similar to node (1,1) (Fig. 4.1) at the expense of other patterns (not shown). We will show that these additional patterns are manifested as a decrease in the frequency through time in our master SOM. This indicates that the master SOM does capture the internal variability through the changing climate and the patterns shown are not artifacts of the method of computing the θ_{e850} anomalies.

4.3 Results

4.3.1 Climatological Change

The development of the CESM large-ensemble provides the range of internal variability that is necessary to produce a climatology over a short time period. Here we conduct ensemble averages of two decades (2010-2020 and 2070-2080) to investigate how the climatology changes from the beginning to the end of the study period. For θ_{e850} we see an expected Arctic amplification signal of higher θ_{e850} over the entire central Arctic Ocean (on the order of 5K) and smaller increases over the mid-latitudes (Fig. 4.3). In general, the greatest increases in θ_{e850} occur in regions that are initially the coldest. This results in greater increases in θ_{e850} in the northeast of the continents, acting to weaken the preexisting East-West θ_{e850} gradient.

Accompanying these increases in θ_{e850} are climatological changes in related mass fields. The 500hPa geopotential height (Z_{500}) increases over the Central Arctic and Eurasia (Fig. 4.4d) by the end of the time period, with a pattern similar to the θ_{e850} increases (Fig. 4.3). This is to be expected with a general warming throughout the troposphere. Over the North Atlantic, where the θ_{e850} anomaly was smallest there is also a deficit in Z_{500} height increases. On the equatorward edge of this deficit in Z_{500} increases, we see an enhanced 200hPa wind speeds (V_{200}) up to $4ms^{-1}$, an increase on the order of 10%. This is indicative of a strengthening and eastward extension of the North Atlantic jet in the future (not shown).

At the surface, the climatological mean sea level pressure (SLP) difference between the

2070-2080 and the 2010-2020 climatologies reveals a decline in SLP over the Eastern Arctic (Barents/Kara Seas), Western Arctic (Bering/Chukchi Seas), Sea of Okhotsk, and Hudson Bay (Figs. 4.5, 4.4c). Commensurate with these regions of low pressure are enhanced turbulent heat flux and declines in sea ice concentration (SIC) 4.4c. This is suggestive of a link between sea ice and local SLP.

In the North Atlantic there is a relative cooling in SSTs (Fig. 4.4b) consistent with the North Atlantic "warming hole" discussed in Drijfhout et al. (2012). Above this warming hole region, there is decreased turbulent heat flux and smaller increases in θ_{e850} and Z_{500} heights relative to surrounding regions (Figs. 4.3,4.4d). These changes in SST and SIC may represent important changes in the surface topography with dynamic and thermodynamic impacts on the overlying atmosphere, which will be further examined in the discussion section.

4.3.2 Internal Variability

The Master SOM of θ_{e850} anomalies identifies dominant air mass patterns relative to a changing climatology (Fig. 4.1). Some of the main features of these map nodes patterns include: lower θ_{e850} over the central Arctic (nodes [1,4] and [1,5]), higher θ_{e850} over northern North America (nodes [2,5], [3,4], and [3,5]), very low θ_{e850} over central and eastern Canada (nodes [2,2], [2,3], [3,2], and [3,3]), and higher θ_{e850} values over the North Atlantic with cold anomalies over Europe (nodes [1,1], [2,1], and [3,1]).

The occurrence of these patterns and their change in time are investigated by computing a time series of best match unit frequency (BMUF) per year for each map node. The internal variability of pattern frequency is provided by the large number of ensemble members. The substantial spread between the median, quartiles, and extrema of BMUF across ensemble members demonstrates the large internal variability (Fig. 4.6).

The self-organizing maps methodology assumes a data distribution that is a continuum, such that if there are members that are very different from one another and there are no observed patterns in between, a transitional SOM map node could be generated but not found to occur. In this master SOM, all members are representative of patterns at some point in the time period and the frequencies are generally well distributed with no member grossly outweighing the rest in terms of frequency of occurrence (Fig. 4.6). With a 15 node SOM, a frequency of 6.67% for each node would represent an equal distribution across the map nodes.

The frequency of occurrence of these nodes is changing throughout the time period (Fig. 4.6). Multiple linear regression applied to the BMUF of each SOM map node reveals statistically significant trends at the 95$^{\text{th}}$ percentile in several of the map nodes. In particular, a pattern with cold θ_{e850} over the central Arctic is declining (nodes [1,5]), patterns with warm θ_{e850} over northern North America are increasing (nodes [2,5], [3,4], and [3,5]). One of the patterns with very cold θ_{e850} over central and eastern Canada is increasing (node [2,3]), and patterns with warm θ_{e850} over the North Atlantic and cold θ_{e850} over Europe are declining (nodes [2,1] and [3,1]).

The associated mass fields with each of these SOM map nodes can be used to gain further understanding into the processes involved in generating differing θ_{e850} patterns. To this end, SOM map node composites are computed for each of the map nodes by averaging days when the map node is the best match unit. Since many of the mass fields experience large changes throughout the time period, we show these results for the node composites of the 2070-2080 time period. Figure 4.7 shows composite total fields of SLP, 500hPa heights, and θ_{e850} for each of the SOM map nodes. For the fields shown in this study, the magnitudes of the variability differ depending on the decade of study chosen but the patterns are similar between decades (not shown).

SOM map nodes [1,4] and [1,5] are characterized by colder θ_{e850} over the central Arctic (Fig. 4.1). The node composite associated with node [1,5] has lower SLP and 500hPa height, as well as more zonal geostrophic upper-level flow centered over the Arctic (Fig. 4.7). These features are indicative of a well developed polar vortex and are typically associated with a positive Arctic Oscillation (AO). This node is also experiencing some of the largest trends in their frequency of occurrence at -5%/century and the median frequency of occurrence drops to drops to 0% by the year 2080 (Fig. 4.6).

The group of SOM map nodes in the bottom right all have a ridge over western North America with higher θ_{e850} anomalies centered on the ridge axis (Fig. 4.7). Node [2,5] has a small ridge and is closest to the positive AO like nodes [1,4] and [1,5] but with smaller cold anomalies over the Arctic. Node [3,5] has a moderately sized ridge, with warm θ_{e850} across North America and cold θ_{e850} over Eurasia. Node [3,4] has a highly amplified ridge and is associated with warm θ_{e850} over Alaska and the Northwest Territories on the order of 8K. Although the SOM was conducted on θ_{e850} anomalies north of 50°N, the composite of node [3,4] also exhibits cold θ_{e850} anomalies south of 50°N in the northeastern US. The geostrophic wind associated with the SLP and 500hPa height fields are veering with height between the upstream trough and amplified western North American ridge in nodes [2,4], [3,4], and [3,5]. This layer mean warm air advection is responsible for the amplification of the ridge. All of these map nodes are experiencing statistically significant increases in the future (Fig. 4.6).

There are four SOM map nodes with very cold θ_{e850} anomalies over northern North America, namely nodes [2,2], [2,3], [3,2], and [3,3] (Fig. 4.1). In each of these patterns there is a trough over central North America and ridging upstream over the Beaufort/Chukchi Seas, Alaska, and/or Eastern Russia (Fig. 4.7). The specific location of the ridge axis and the tilt of the trough distinguishes the locations of maximum cold θ_{e850} anomalies in these patterns, all of which are on the order of -8K. For each of these, the maximum cold anomaly is located a quarter wavelength upstream of the trough, where you would expect the maximum anti-cyclonic vorticity advection and cold air advection to occur. Similar to nodes [2,4], [3,4], and [3,5] with ridges located over western North America, these patterns are all consistent with a baroclinic waves over North America. This is evidenced in the relative locations of the upper-level ridge/trough to the lower level SLP, where we can see that troughs are tilted westward with height. Of these nodes, [2,3] is the only one that has significant trends and it is increasing in the future (Fig. 4.6). In this pattern the ridge is located over the Chukchi Sea and greatest θ_{e850} anomalies occurring over British Columbia, the Canadian Prairies and the Northwest Territories. The other three patterns with negative θ_{e850} anomalies over northern North America have no significant trend, so the trend in pattern [2,3] implies that there is a total increase in cold anomalies over Canada through the period.

The three nodes on the left hand side of the SOM map (nodes [1,1], [2,1], and [3,1]) are characterized by warm θ_{e850} anomalies over the North Atlantic or Central Arctic and cold anomalies over Europe (Fig. 4.1). Nodes [1,1] and [2,1] have a dipole in SLP anomalies across the North Atlantic, with a positive anomaly over Northern Europe and negative anomaly over Greenland (Fig. 4.8). This would favor the southerly advection of warm air from the Atlantic into the Eastern Arctic, consistent with the existence of a warm anomaly in the North Atlantic. In the upper-levels, these patterns are associated with enhanced ridging in the 500hPa flow over the Barents and Kara seas (Fig. 4.7). Node [3,1] is also associated with a positive SLP anomaly, however it is centered over the North Atlantic and instead of being accompanied by a negative anomaly over Greenland, there is a negative SLP anomaly over Eastern Russia (Fig. 4.7). This would imply anomalous southerly advection from the Pacific, over Alaska, and into the central Arctic. This would explain why the warm anomaly in this pattern is centered over the central Arctic as opposed to nodes [1,1] and [2,1] where it is located more towards the Eastern Arctic and North Atlantic. There are significant declines in the frequency of occurrence in nodes [2,1] and [3,1] in the future (Fig. 4.6).

4.4 Discussion

In this section we put forth hypotheses for the causes of trends in the frequency of occurence of SOM map nodes and highlight their relationships to known modes of climate variability. A particular emphasis is placed on climatological changes in surface boundary conditions that may alter planetary scale circulations associated with these SOM node patterns.

4.4.1 Implications for the AO / NAO

Node [1,5] is characterized by cold θ_{e850} anomalies over the central Arctic compared to the mid-latitudes, lower SLP, and lower 500hPa geopotential heights (Fig. 4.7 and 4.8). This node is also experiencing significant declines in the future. The erosion of the Arctic inversion layer may lead to reduced cold air generation over the central Arctic relative to the midlatitudes and be responsible for this change in the frequency of Node [1,5].

This pattern is also typical of the surface temperature and upper-level exhibition of the positive phase of the AO, which could have implications for future changes in the AO. However, this study is not conducted on SLP, which is used to define the AO. The AO is typically defined as the first EOF of SLP over the Arctic, with a positive phase consisting of SLP anomalies that are negative over the central Arctic and positive over the North Atlantic and North Pacific (Thompson and Wallace, 1998). It is also generally associated with more zonal upper-level flow, enhanced contrast in upper-level heights between the Arctic and midlatitudes, and a strong polar vortex (Thompson and Wallace, 1998).

In the climatology, there is an apparent contradiction in the climate change impact on the AO at the surface versus the upper-level flow. There are local decreases in SLP concentrated over the eastern and western Arctic that extend into the central Arctic in the climatology (Fig. 4.4). These would project onto the EOF loading pattern of the AO and manifest as a positive trend in the AO index. Several authors have cited increases in the AO or closely related NAO with global warming when examining the SLP field in observations (Fyfe et al., 1999) and future climate modeling studies (Gillett, 2002; Bader et al., 2011). In the upper-levels, there is a greater increase in the 500hPa geopotential heights over the central Arctic than over the midlatitudes, which act to decrease the N-S gradient in geopotential heights. From the upper-level perspective, this would signify a decline in the Arctic Oscillation. This finding brings forth an interesting question of whether the equivalent barotropic structure through the depth of the atmosphere that characterizes the AO will break down in the future and how this will manifest itself in terms of the AO phase.

An alternative hypothesis put forth by Ambaum et al. (2001), is that the AO is itself not a physical mode but rather the co-variability of the NAO and the Aleutian low, which is manifested as the first EOF of the Northern Hemisphere SLP. A more positive NAO, and weaker Aleutian low results in more zonally symetric surface and upper-level flow. From this perspective, the contradiction ceases to exist, as the NAO and Aleutian low may vary independently, both becoming stronger in the future. This would result in an apparent increase in the AO without the constraint of more zonal flow.

Regardless of the interpretation of the AO mode, the traditional method of computing the AO index using EOFs requires stationarity in the time series, which is not the case given global climate change. A technique such as self-organizing maps applied to variables that represent the upper and lower level manifestations of the AO may prove useful in addressing these questions.

4.4.2 Role of the North Atlantic Warming Hole

Amidst the increase in global sea surface temperature (SST), the North Atlantic has experienced a warming deficit (Drijfhout et al., 2012). This "North Atlantic warming hole" has been related to a slowing of the Atlantic meridional overturning circulation (MOC) (Rahmstorf et al., 2015; Drijfhout et al., 2012; Woollings et al., 2012), which is expected to continue to slow in the future (Collins et al., 2013). In the historical period, the MOC has been shown to drive the internal variability of the North Atlantic through its impacts on the Atlantic Multidecadal Oscillation (AMO). Phases of the AMO have in turn been related to storm tracks (Yamamoto and Palter, personal communication), atmospheric circulation patterns (Alexander et al., 2014; Ting et al., 2014), and precipitation (Alexander et al., 2014; Ting et al., 2014) over the North Atlantic. We may therefore expect that the North Atlantic warming hole may have significant consequences for the atmospheric circulation in the future. For example, Woollings et al. (2012) associated the North Atlantic warming hole with an eastward extension of the North Atlantic storm track.

In the CESM-LE, this SST feature is seen in the climatological difference between the 2070-2080 and 2010-2020 decadal averages, as a region of smaller temperature increase compared to the surroundings (Fig. 4.4). The lack of warming extends into the atmosphere, where we can see less θ_{e850} increases and consequently lower 500hPa heights (Fig. 4.4) consistent with lower column thicknesses over this region. The geostrophic wind associated with this relative lack of 500hPa height increase implies enhanced cyclonic circulation over the eastern North Atlantic, resulting in a strengthening and extension of the North Atlantic jet. The configuration resembles a shift towards a more positive NAO phase. This is a dynamically consistent mechanism by which the SSTs may be impacting the atmospheric circulations and is consistent with the results of Woollings et al. (2012) indicating an extension of the North Atlantic storm track.

We hypothesize that this climatological forcing decreases the probability of occurrence of nodes [2,1] and [3,1]. The strengthening and extension of the jet over Europe shifts the poleward jet exit region over the Barents-Kara Seas. The upper-level forcing of the poleward jet exit region would act to inhibit the formation of the large anticyclones over the North Atlantic, typical of nodes [2,1] and [3,1] (Fig. 4.8). Although there have been suggestions that reduced sea ice in the Barents-Kara Seas would increase the production of anticyclones in the region (Liu et al., 2012; Petoukhov and Semenov, 2010), this SST anomaly associated with the North Atlantic warming hole may act to dampen the sea ice signal in the future.

4.4.3 Role of Sea Ice Loss

The presence of sea ice insulates the cold overlying atmosphere from the warmer ocean below. This sea ice cover is declining rapidly, with projections indicating the likelihood of a purely seasonal ice cover prior to the mid 21st century (Collins et al., 2013; Wang and Overland, 2012). Although sea ice losses are greatest in the summer, winter sea ice loss has a larger impact on the atmosphere with greater heat fluxes and consequently larger increases in air temperature (Deser et al., 2010; Singarayer et al., 2006). Several global climate modeling studies have been conducted to study the atmospheric response to sea ice loss using prescribed sea ice and SST boundary conditions that either represent interannual variability in the historical period (Honda et al., 1999; Deser et al., 2000; Alexander et al., 2004; Kvamstøet al., 2004) or future projected sea ice loss (Magnusdottir et al., 2004; Deser et al., 2004; Singarayer et al., 2006; Seierstad and Bader, 2008; Deser et al., 2010). A comprehensive review of the topic was conducted by Budikova (2009), although many studies have been published since then. In a 20th century GCM modeling study with prescribed sea ice loss from the end of the 21st century, Deser et al. (2010) show that sea ice loss in January-February results in an average increase in temperature, with the warming concentrated North of 65°N and vertically to 800hPa and accompanied by an increase in 500hPa heights over the central Arctic. This mean change is consistent with the declining frequency of pattern [1,5] (Fig. 4.1), which is characterized by low θ_{e850} and lower geopotential heights over the central Arctic (Fig. 4.6).

In addition to local impacts on air temperature, many modeling studies have addressed the impact of sea ice loss on the midlatitude flow in the winter (Honda et al., 1999; Deser et al., 2004; Alexander et al., 2004; Magnusdottir et al., 2004; Singarayer et al., 2006; Seierstad and Bader, 2008). The mid-latitude response to sea ice loss varies depending on the specifics of the experiment, such as region of sea ice loss and month of study. Deser et al. (2004) decomposed the sea ice response to North Atlantic loss into an indirect response that projected onto the NAO and a direct response consisting of the remainder. They found that the indirect response was a negative NAO and the direct response was a surface low pressure system over the sea ice anomaly and downstream baroclinic wave. Seierstad and Bader (2008) attributed the incongruities between the response to North Atlantic sea ice loss in various studies to the amount of indirect versus direct response. Many studies suggest a large indirect response where North Atlantic sea ice loss projects strongly onto the NAO, where low sea ice is related to a negative NAO pattern (Deser et al., 2004; Seierstad and Bader, 2008; Alexander et al., 2004; Magnusdottir et al., 2004). Whereas Singarayer et al. (2006) noted a decrease in sea level pressure over the region of sea ice loss, similar to the direct response of Deser et al. (2004).

Though there are fewer studies that focus on the response to sea ice loss in the Western Arctic, the results are consistent. In experiments with prescribed interannual variability in the Sea of Okhotsk, both Honda et al. (1999) and Alexander et al. (2004) found a stationary Rossby wave response to reduced sea ice that extended across the Pacific and into North America. Honda et al. (1999) corroborated these results in the observations looking at differences between high and low sea ice years. In these studies, there is a localized low SLP anomaly above the region of sea ice loss and a downstream ridge in the upper-levels (Honda et al., 1999; Alexander et al., 2004), as was found in the direct response of Deser et al. (2004).

We hypothesize that on a climatological timescale, sea ice reduction may result in the generation of a localized thermal low, which provides enhanced forcing to passing upper-level baroclinic waves. Localized maxima in diabatic heating can result in the formation of surface cyclone (Bluestein, 1993, ch. 1). Since sea ice in the Sea of Okhotsk, Bering Sea, and Chukchi Sea is bounded by the land (Fig. 4.5), the climatological loss of sea ice and the resulting enhanced turbulent heat fluxes will be localized anomalies. This is seen in the climatological differences between the 2070-2080 and 2010-2020 ensemble decadal averages, where there is increased turbulent heat fluxes and decreased SLP above regions of sea ice loss (Fig. 4.4). The localized low pressure systems represent an increase in potential vorticity and result in enhanced surface temperature advections. In a dynamically coupled atmosphere, such temperature advections can feedback onto the upper-levels through impacts on the height tendencies. As such, a thermal low at the surface could amplify upper-level baroclinic waves passing over the thermal anomaly, provided that it is downstream (upstream) of an upper-level trough (ridge). This is consistent with the direct response to sea ice loss identified by Deser et al. (2004) and the response to anomalous sea ice in the Sea of Okhotsk in Honda et al. (1999); Alexander et al. (2004).

An analogy of this mechanism can be made to the presence of high orography of the Rocky Mountain range on the west coast of North America. In the lee of the mountain range, a surface trough is formed as a result of subsidence heating (Bluestein, 1993). In addition to generating a climatological surface pressure feature, the presence of the mountains and the lee cyclogenesis associated with them also enhances the development of baroclinic disturbances in the upper levels (Bluestein, 1993). In the context of this work, the climatological change in sea ice would be analagous to the development of a region of downsloping, which has an expression as a surface climatological feature and will also impact the development of baroclinic waves.

In the context of the SOM analysis, increased baroclinic wave development resulting from sea ice loss in the western Arctic would be manifested as an increase in the frequency of SOM nodes with baroclinic upper-level waves situated over North America. This is the case for patterns [2,2], [2,3], [2,4], [2,5], [3,2], [3,3], [3,4], and [3,5], all of which are associated with amplified 500hPa flow and consequently have large θ_{e850} anomalies over parts North America (Fig. 4.7). All of these patterns are either experiencing no significant change in frequency or a significant increase in frequency (Fig. 4.6). Over Eurasia, this type of forcing due to sea ice loss also exists, however we suggest that the existence of a North Atlantic warming hole may be acting to strengthen the jet and oppose the sea ice impact.

4.5 Conclusions

In this study, we apply a technique of self-organizing maps to the new state of the art CESM-LE to identify archetypical Arctic air mass patterns and associated circulation structures that will be present through the 21st century. We have shown that in the future, there will be changes in the frequency of θ_{e850} anomaly patterns relative to the ensemble mean climatic change, indicating a change in the internal variability.

In particular, there is a decline in patterns associated with amplified flow over Europe associated with warm θ_{e850} over the North Atlantic / Eastern Arctic and cold θ_{e850} over Eurasia. These patterns are reminescent of the cold European winter of 2012-13. Over North America, there is an increase in patterns with more amplified upper-level flow, resulting in an increased frequency of patterns exhibiting warmer air masses and colder air masses. The 2014-15 cold winter over the northeastern is similar to one of these nodes, which is also expected to become more frequent in the future. A pattern with an anomalously cold air mass over the central Arctic, associated with a well developed polar vortex typical of the positive phase of the Arctic Oscillation, will be less important in the future. These results imply that during the next century, there will be a transition from a state where cold air is built up over the central Arctic to one in which cold air generation over the North American landmass is more important.

We hypothesize that changes in the surface forcing by sea ice and SSTs could lead to changes in boundary conditions that alter the frequency of occurrence of these patterns. In particular, the change in the frequency of patterns of amplified flow may be related to surface forcing from declining sea ice and resulting enhanced forcing of baroclinic waves over North America. For the Eurasian sector, the existence of a warming hole in SSTs, shown in Drijfhout et al. (2012) to be related to the meridional overturning circulation, may play a role in the decline of this pattern by enhancing the North Atlantic jet. Further research would be required to explore the causality of these mechanisms.

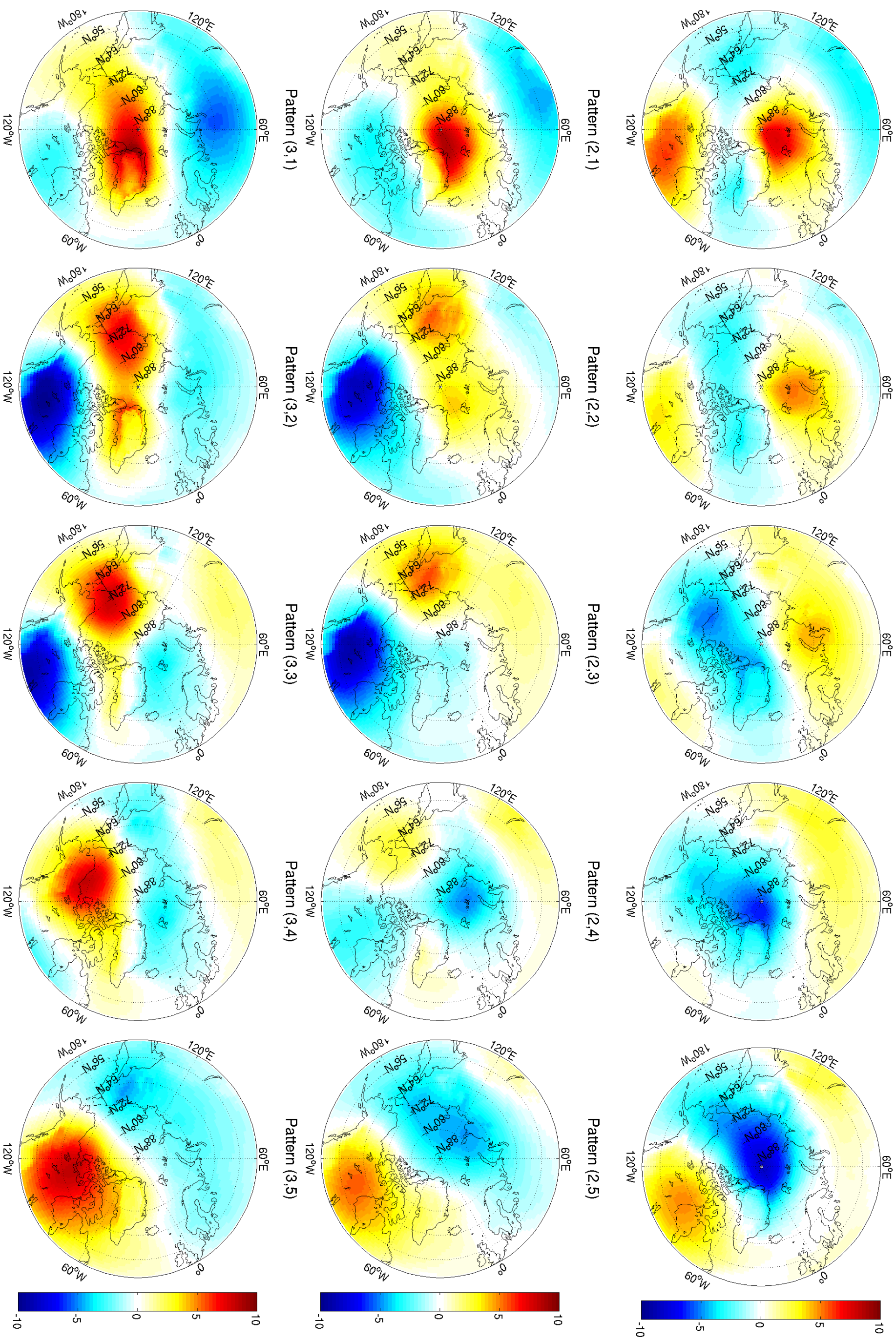

FIGURE 4.1: Map nodes patterns for Master SOM of daily θ_{e850} at 850hPa anomalies with respect to annual JF ensemble mean (K, color).

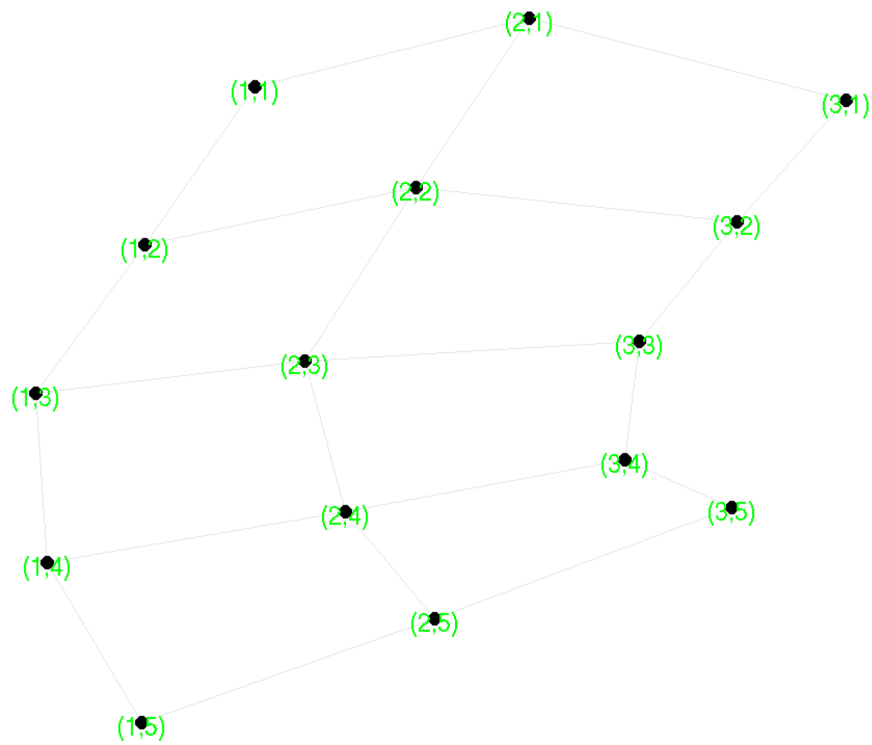

FIGURE 4.2: Sammon map representing the relative euclidean distances between the map nodes for the SOM shown in figure 4.1.

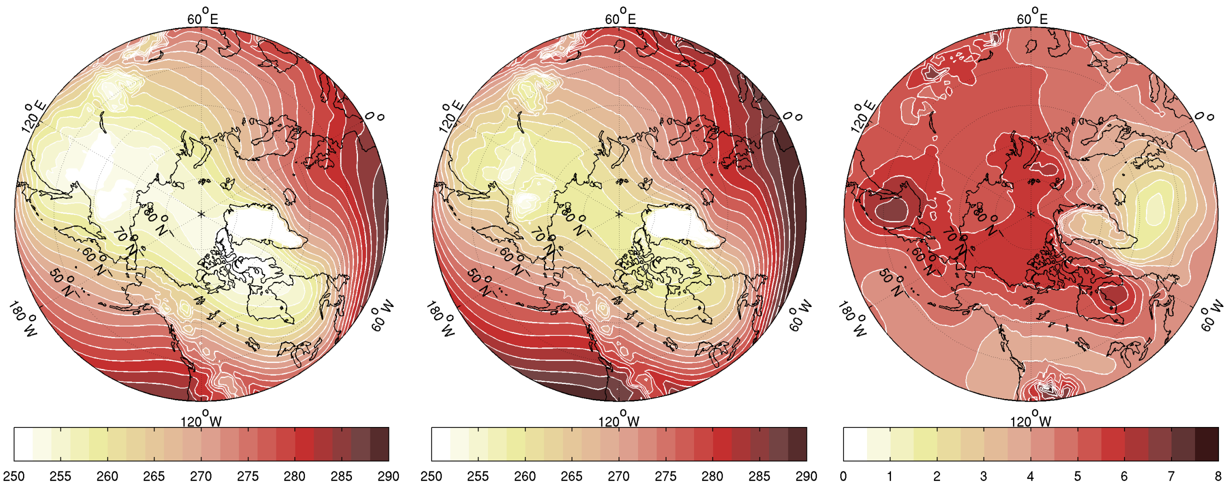

Figure 4.3: Decadal JF ensemble mean θ_{e850} (K) for a) 2010-2020, b) 2070-2080, and c) difference (2070-2080) - (2010-2020).

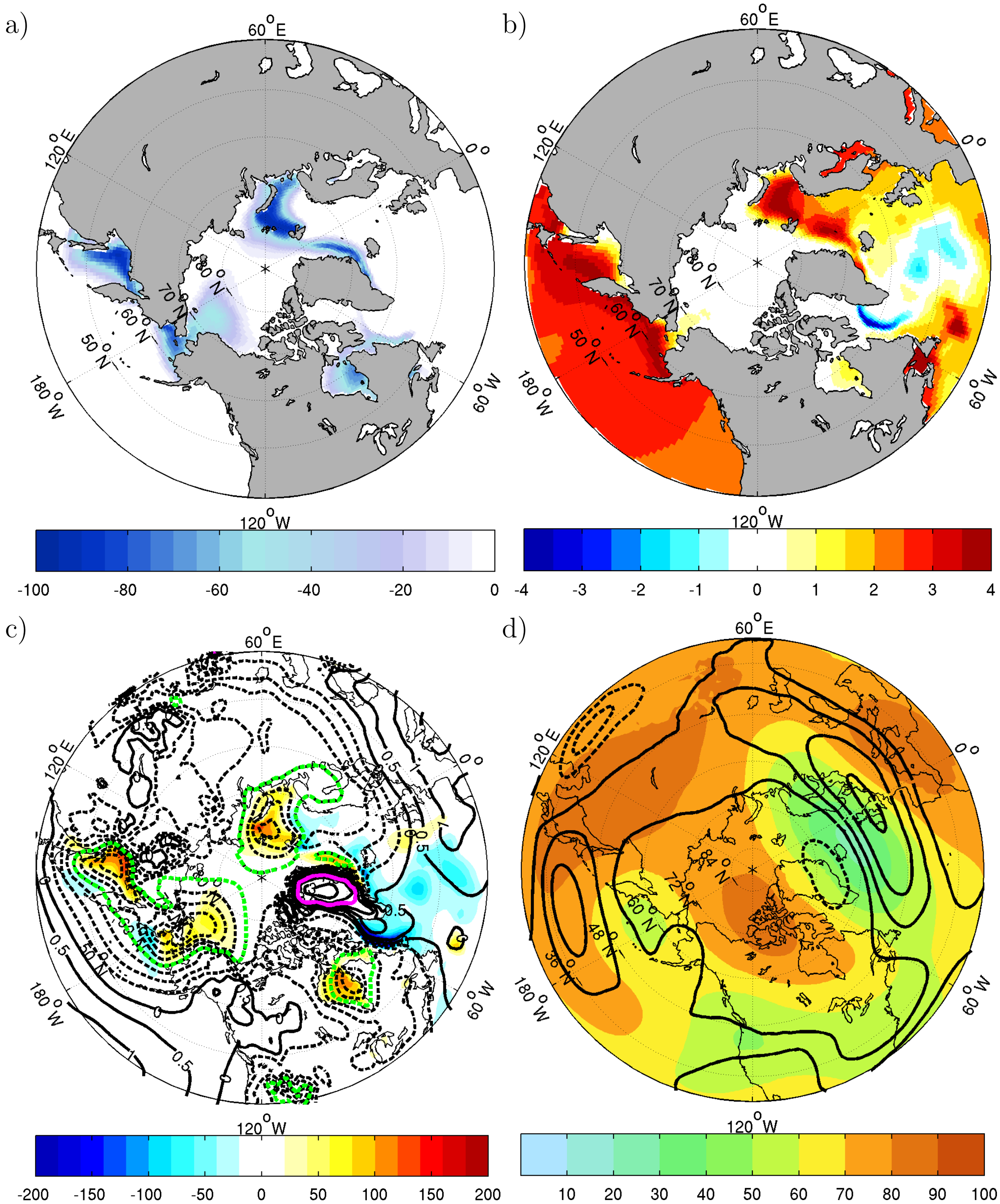

FIGURE 4.4: Decadal JF ensemble mean difference (2070-2080) - (2010-2020) for a) SIC (%), b) SST (K), c) turbulent heat flux (W/m^2, color) and SLP (hPa, contoured every 0.5hPa, dashed negative, -2hPa in green, and $+2$hPa in magenta), d) 500hPa geopotential height (m, color) and 200hPa wind speed (contours every $1m/s$, dashed negative).

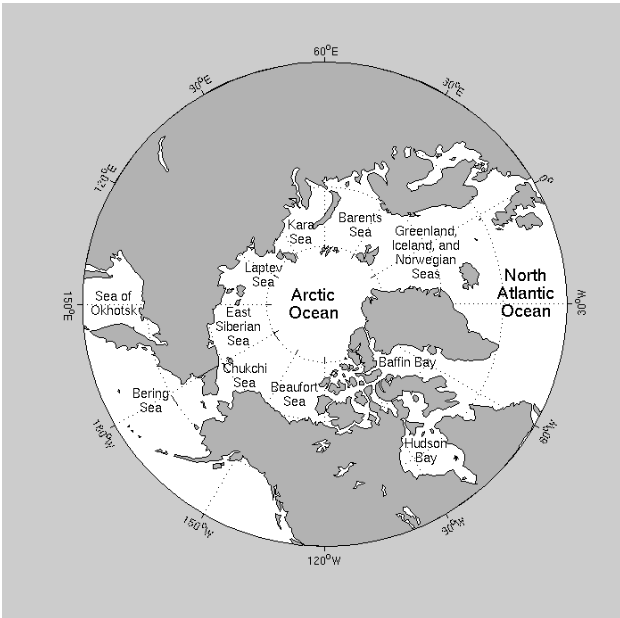

Figure 4.5: Map of the Arctic Ocean indicating location of peripheral seas.

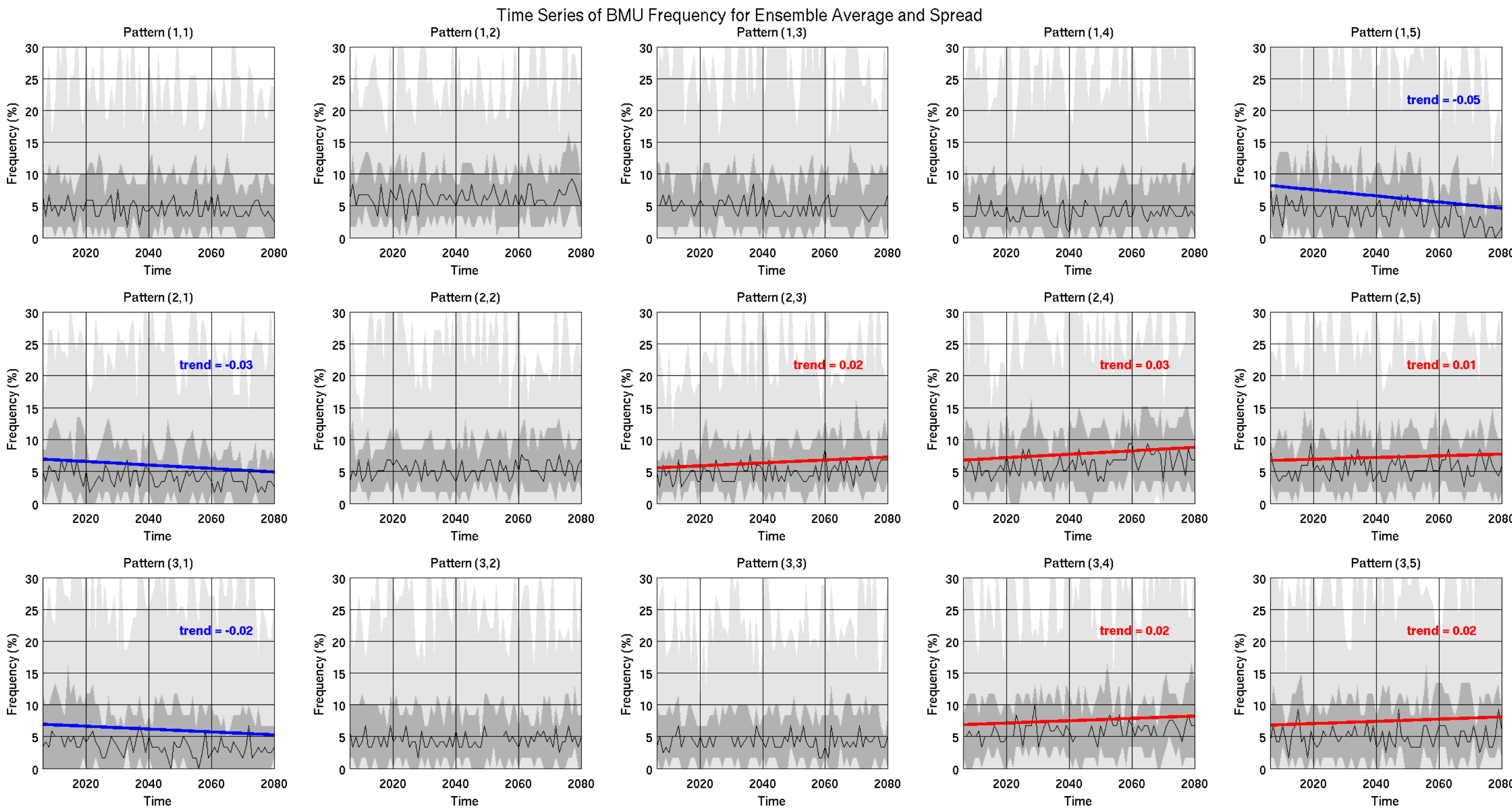

FIGURE 4.6: Ensemble spread in average JF best match unit frequency over time. Ensemble median (solid black line), 25th to 75th percentiles (dark grey shading), and maximum to minimum (light grey shading). Statistically significant multiple linear regressions of the best match unit frequencies (at the 95th confidence level) are shown as red (positive) and blue (negative) trend lines with given trend value in %/year.

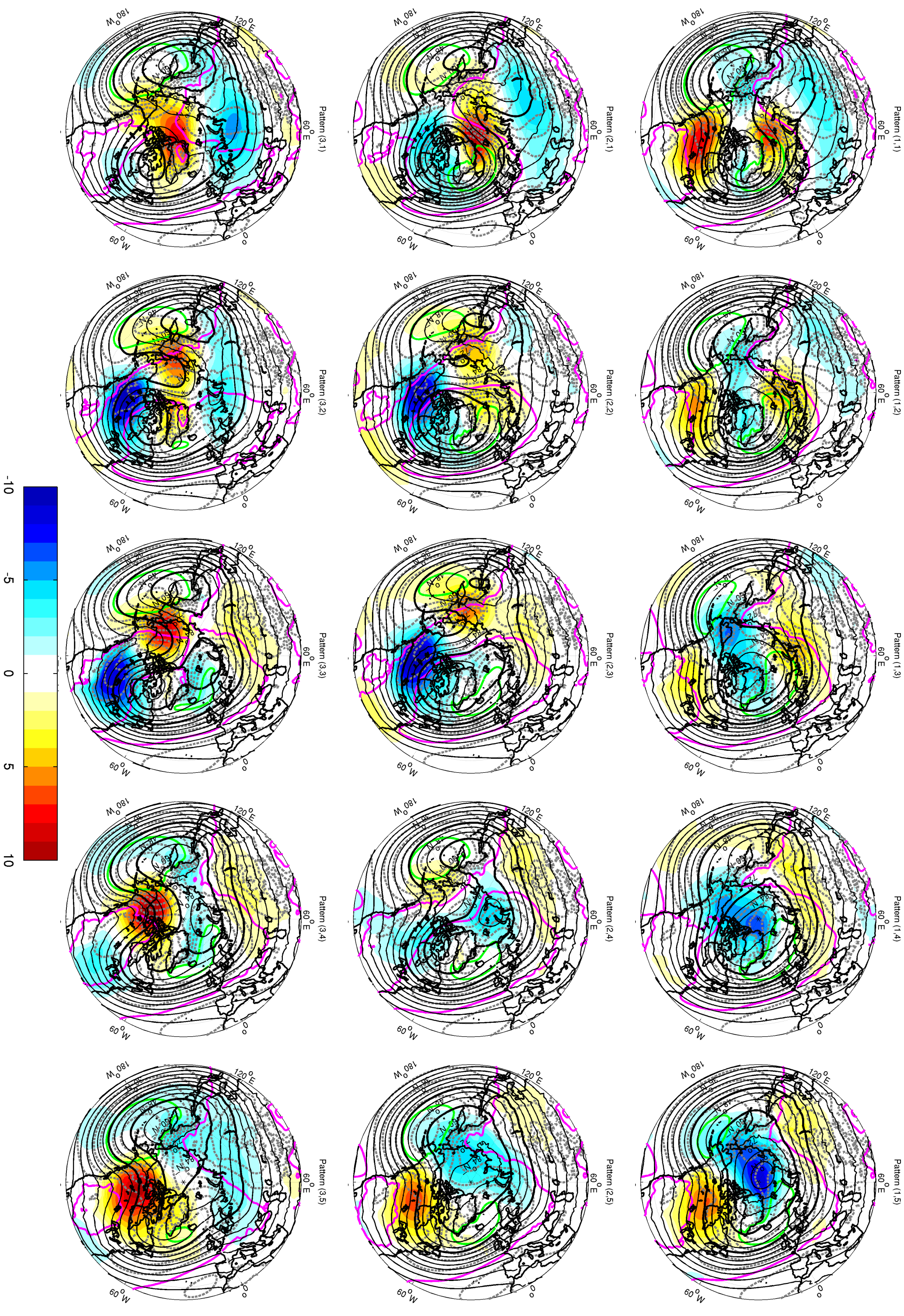

Figure 4.7: SOM node (2070-2080) equivalent potential temperature anomalies relative to decadal average (K, color), SLP (hPa, grey contours with 1020hPa in magenta and 1000hPa in green), and geopotential height at 500hPa (m, black contours with 5220m and 5400m in thick black lines).

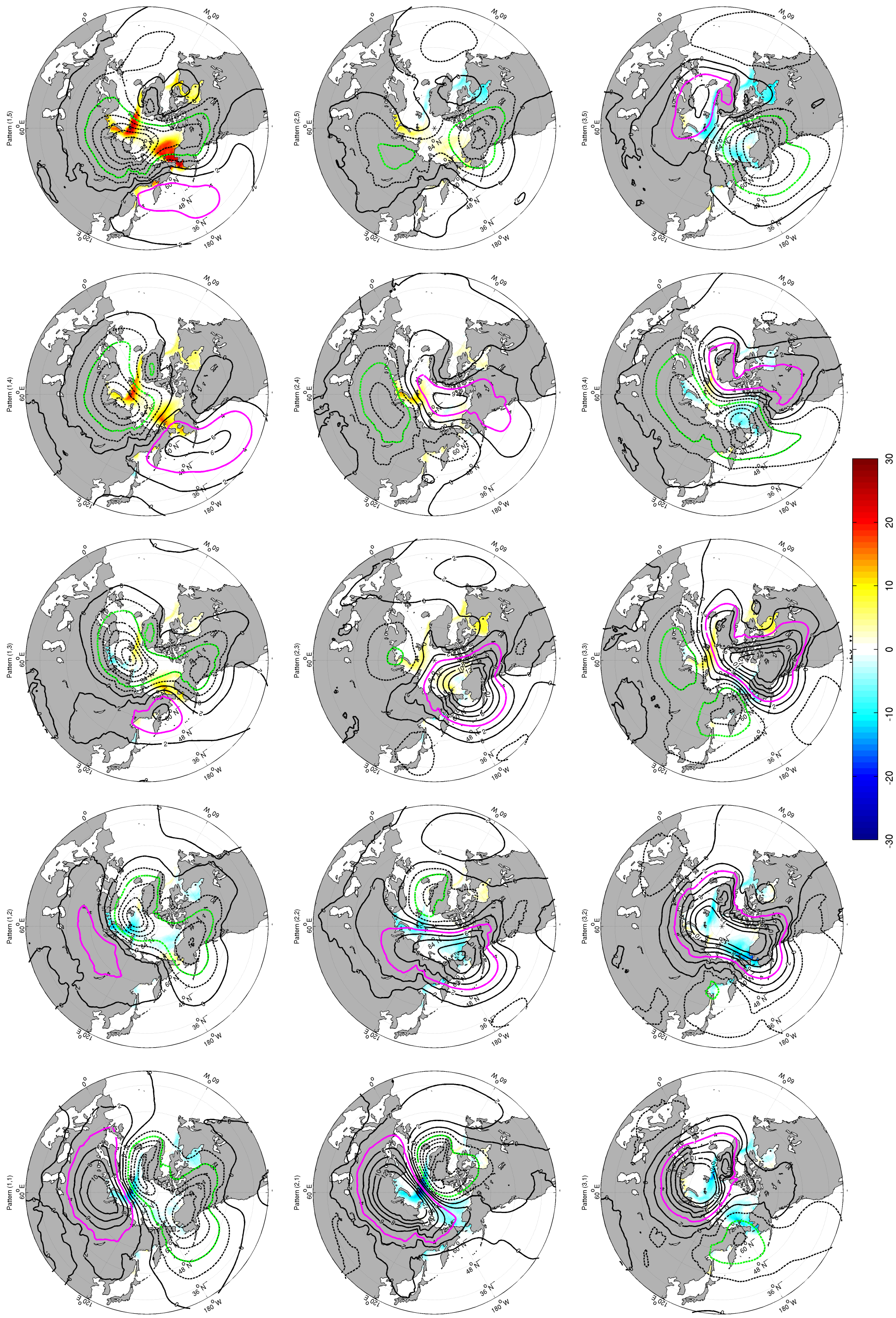

FIGURE 4.8: SOM node anomaly relative to the decadal ensemble average (2070-2080) of SIC (%) and SLP (hPa) contoured solid black for positive, dashed black for negative, magenta for +4 hPa, and green for -4 hPa.

Chapter 5

Summary and discussion

The goal of this thesis is to examine climate as a function of sensible weather, for the fundamental purpose of understanding the impact of climate change on society. I focus on precipitation and air masses, which are two fundamental quantities in the definition of daily weather. For each of these, important issues related to climate analysis and the prediction of future change are identified and studied, with an emphasis on higher-order frequency variability and spatial patterns.

Chapter 2 is concerned with precipitation observations as they are applied for comparison to climate models. Taking the position that precipitation in a global climate model (GCM) represents an area-average over a grid box, there is an inherent mis-match of scales between station precipitation observations and precipitation produced by a GCM. The station data must be upscaled for comparison to GCM output. I show that differences in extreme precipitation over the United States can be as large as 30mm day^{-1} between the original station value and the same data remapped to the model grid resolution. Implicit in this observation is that GCM predictions are produced as an average over a wide region, however the society experiences sensible weather at the scale of a point location. This is an important consideration for communication of the actual impact of climate change predicted by the GCM. In the general, the magnitude of extreme precipitation predicted by a model would be larger at point location.

The upscaling methodology recommended and employed in Chapter 2, is to first produce an objective analysis of station data onto a high-resolution grid, and subsequently conduct an area-weighted remapping procedure to produce a gridded product at the resolution of the climate model. Errors that are incurred during this process are called representativeness errors. In the event that this last step of gridding to the model resolution is conducted through interpolation instead of the remapping method suggested, I found the median and extremes can be up to 30% higher. This is a significant departure and thus it is imperative that such observation be treated appropriately. This however, is not always the case in the literature.

A further complication to the issue of representativeness errors is the impact of station density. I designed a station density experiment and quantified a range of errors for a given station density. The shapes of the error ranges were dependent on the region and season in question. I proposed two conceptual frameworks through which the error structures could be understood.

The first framework applies when the distribution of precipitation is homogeneous, such that the median and extreme values are spatially uniform. This is typical of the eastern United States. In this case, as station density decreases there is a greater influence on the analysis of more distant stations with less shared variance. This reduces the magnitude of precipitation resulting in a small negative bias in the analysis. The representativeness errors in this case are higher when the length scale of precipitation systems are smaller, and thus during summer convection season.

The second framework applies when there are large spatial inhomogeneities in the climatological distribution of precipitation. Such situations occur for example in mountainous regions. As the station density decreases, there is a greater influence on the analysis point of stations that are further away and have very different precipitation distributions. This results in very high sensitivity to station density, resulting in large positive or negative errors. In this case, errors are greatest when the inhomogeneity is greatest. For the western United States this is true in winter when a great deal of orographic precipitation occurs, creating large discontinuities in precipitation in the mountains compared to the valleys or plains.

The subject of Chapter 3 is understanding and quantifying errors in GCM representation of precipitation in the fully coupled Community Climate System Model (CCSM4) and two versions of its atmospheric component model Community Atmosphere Model (CAM), CAM4 and CAM5. To accomplish this, several observational and reanalysis products are used to constrain the distribution of precipitation. The study region in this chapter is over North America.

I create an amalgamated gridded precipitation analysis using the Unified Precipitation Dataset (UPD) over the contiguous United States and the Daily 10km Gridded Climate Dataset for Canada (GCDC) over Canada south of 60°N. An envelope of potential representativeness errors with station density, created in Chapter 2, is applied in Chapter 3 to quantify the representativeness errors in a gridded precipitation product used for GCM validation. Over northern Canada these errors reached a maximum of 50%. Comparisons are also made to a satellite product, the Global Precipitation Climatology Project 1 DD (GPCP), and a reanalysis product, the Climate Forecast System Reanalysis (CFSR). Since there are issues with all precipitation reference products it is important to examine GCM errors within the context of a variety of reference sources.

I find that the GCMs are able to represent the observed distribution of precipitation within the errors of the products used for the validation at many of the locations studied. Studies have shown that GCMs generally produce too little light and too much heavy precipitation. This study looks at the distribution of precipitation and finds this positive skewness anomaly to occur east of the Rocky Mountains. Within and to the west of the mountains, the model skewness relative to the station observations is the opposite with more heavy and less light daily precipitation values.

An analysis of bi-monthly intensity of extreme precipitation does find some striking issues with the model's ability to produce intense precipitation. In previous model versions, convection was triggered too early not allowing the build-up of convective available potential energy necessary for very intense events. This is investigated in Chapter 3 through an analysis of the diurnal timing of precipitation. The results show that the maximum precipitation east of the Rocky mountains occurs in the evening and overnight hours in the observations but in the mid-afternoon in the model. This issue is still prevalent even when the model is run at a higher 0.25° resolution. Although the improvements to the model convective parameterizations showed large improvements in the tropics (Gent et al., 2011), these results demonstate a lack of improvement over North America. There remain large issues with heavy precipitation, which cannot be resolved with increased resolution.

These results can inform users which predicted precipitation changes can be trusted. For example, if convection is generally not well represented, we should not expect models to accurately predicted changes in regions where convection is an important part of the climatology. On the other hand, large-scale precipitation does seem to be reasonably well represented and as such changes in precipitation owing to shifts in large-scale circulation patterns should be more credible. Across North America, this generalizes to extreme precipitation and its future changes being less trustworthy in the summer, especially over the great plains and the southeastern United States. Changes in the precipitation over the west coast, such as the predicted decrease in California precipitation, are more trustworthy.

Chapter 4 is concerned with air masses and, since they are a less difficult quantity to represent, we move directly to how they will change in the future. With Arctic amplification, the greatest temperature changes are occurring in the Arctic and during the winter. I am thus particularly interested in winter Arctic air masses and how their internal variability might change in the future.

The National Center for Atmospheric Research recently released a large ensemble set of predictions using the Community Earth System Model (CESM). The purpose of the experiment was to enable users to study present and future climate with the wide range of internal variability therein. In Chapter 4, I leverage this ensemble set to produce daily anomalies with respect to a changing climate of equivalent potential temperature (θ_e), used to represent air masses. I then apply self-organizing maps to these anomalies to produce a set of archetypal anomaly patterns along with their changing frequency throughout time.

I find that in addition to the climatological changes in air masses, there are also changes in the internal variability. Patterns with anomalously low θ_e over the central Arctic are projected to occur less frequently in the future. Composites of days assigned to these patterns reveal their association with zonal 500hPa flow and surface low pressure, both typical of the Arctic Oscillation. This results in an apparent contradiction as the AO is projected to increase in the future. However, I present the argument that the increase in the AO may instead be a function of the declining SLP related to sea ice loss, which would project onto the empirical orthogonal function (EOF) used to define the AO. EOF analysis is also predicated on the assumption that the underlying data is stationary, which is not true in climate change situations.

Patterns with high θ_e over the Barents/Kara Seas and low θ_e over Europe are predicted to decline in the future. These patterns resemble the cold European winter of 2012-13, with ridging over the North Atlantic. I propose that a warming deficit in SSTs over the North Atlantic induces a relative decrease in upper level heights and increased cyclonic circulation. This results in a strengthening and extension of the North Atlantic jet, shifting the poleward jet exit region over the Barents/Kara Seas. The upper-level cyclonic forcing of the poleward jet exit region would act to inhibit the large anticyclones typical of this pattern with high θ_e over the Barents/Kara Seas.

There is a final set of patterns of interest in Chapter 4 that are experiencing significant increases in frequency in the future. These patterns exhibit large positive and negative θ_e anomalies over North America. All of these patterns have an amplified planetary wave over North America with locations of the wave axes defining the regions with positive and negative θ_e anomalies. The set of patterns with cold θ_e anomalies over North America are reminiscent of the winters of 2013-14 and 2014-15. Such high-impact cold weather events are thus expected to continue in the future, but relative to a higher mean winter temperature.

I hypothesize that the increase in the frequency of these patterns may be related to climatological sea ice loss in the Sea of Okhotsk, Bering Sea, and Chukchi Sea. Associated with these regions of sea ice loss are climatological increases in turbulent heat flux and decreases in sea level pressure. These localize heating anomalies may act to enhance upstream upper-level baroclinic waves when the troughs is located upstream of the anomaly. The manifestation of the resulting enhancement of baroclinic waves would be an increase in frequency of these patterns associated with amplified planetary waves over North America.

This thesis has demonstrated that within the mean climate lies a great deal of interesting sensible weather, in terms of both precipitation and air masses. Adopting new methodologies and datasets will be a key aspect of studying these changes in sensible weather in the future. As part of societies adaptation to climate change, it is imperative to have accurate predictions of the average change, but also how this will be manifested in terms of changes in variability. Understanding the underlying causes of these changes in sensible weather will be of the utmost importance for their prediction.

5.1 Ideas for Future Work

Chapter 4 introduces a perspective that changes in future surface boundary conditions could impact the probability of occurrence of certain patterns in sensible weather. Hypotheses are put forth in this chapter for how western Arctic sea ice and the North Atlantic warming hole might impact patterns of Arctic air mass variability. These ideas can form the basis for several future research projects. The basic question would be: how will changes in the surface boundary conditions, resulting from climatic change, impact sensible weather?

For the impact of the North Atlantic warming hole, an atmosphere only modeling study with prescribed surface boundary conditions, could be conducted to address the relative impacts of Barents/Kara sea ice loss and the North Atlantic warming hole on patterns of atmospheric circulation. A set of experiments could be designed with the warming hole present or filled in and low or high sea ice concentrations in the eastern Arctic. Employing self-organizing maps to examine the output of such experiments would allow for the study of changes in the frequency of occurrence of circulation patterns associated with these surface boundary changes.

A similar set of experiments could be conducted to asses the impact of sea ice loss in the Sea of Okhotsk, Bering Sea, and Chukchi Sea. Sea ice in these regions also have large interannual variability. In addition to examining the impact of climatological mean change in sea ice, it would be interesting to investigate the possibility of coupled variability between the ocean and the atmosphere on interannual time scales. Part of answering this question is understanding the causes of the interannual variability of sea ice and assessing its predictability.

Bibliography

Accadia, C., S. Mariani, M. Casaioli, and A. Lavagnini, 2003: Sensitivity of Precipitation Forecast Skill Scores to Bilinear Interpolation and a Simple Nearest-Neighbor Average Method on High-Resolution Verification Grids. *Weather and Forecasting*, **18**, 918–932.

Adam, J. C. and D. P. Lettenmaier, 2003: Adjustment of global gridded precipitation for systematic bias. *Journal of Geophysical Research*, **108 (D9)**, 1–15, doi: 10.1029/2002JD002499.

Alexander, M., U. S. Bhatt, J. Walsh, M. Timlin, J. Milller, and J. Scott, 2004: The Atmospheric Response to Realistic Arctic Sea Ice Anomalies in an AGCM during Winter. *Journal of Climate*, **17**, 890–905.

Alexander, M. A., K. Halimeda Kilbourne, and J. A. Nye, 2014: Climate variability during warm and cold phases of the Atlantic Multidecadal Oscillation (AMO) 1871-2008. *Journal of Marine Systems*, **133**, 14–26, doi: 10.1016/j.jmarsys.2013.07.017.

Ambaum, M. H. P., B. J. Hoskins, and D. B. Stephenson, 2001: Arctic Oscillation or North Atlantic Oscillation? *Journal of Climate*, **14**, 3495–3507, doi: 10.1175/1520-0442(2001)014<3495:AOONAO>2.0.CO;2.

Anderson, T. W., 1962: On the distribution of the two-sample cramer-von mises criterion. *The Annals of Mathematical Statistics*, **33 (3)**, 1148–1159.

Anderson, T. W. and D. A. Darling, 1952: Asymptotic Theory of Certain "Goodness of Fit" Criteria Based on Stochastic Processes. *Annals of Mathematical Statistics*, **23 (2)**, 192–212.

Bacmeister, J. T., M. F. Wehner, R. B. Neale, A. Gettelman, C. Hannay, P. H. Lauritzen, J. M. Caron, and J. E. Truesdale, 2014: Exploratory high-resolution climate simulations using the community atmosphere model (CAM). *Journal of Climate*, **27**, 3073–3099, doi: 10.1175/JCLI-D-13-00387.1.

Bader, J., M. D. S. Mesquita, K. I. Hodges, N. Keenlyside, S. Ø sterhus, and M. Miles, 2011: A review on Northern Hemisphere sea-ice, storminess and the North Atlantic Oscillation: Observations and projected changes. *Atmospheric Research*, **101 (4)**, 809–834, doi: 10.1016/j.atmosres.2011.04.007.

Barnes, E. A., 2013: Revisiting the evidence linking Arctic amplification to extreme weather in midlatitudes. *Geophysical Research Letters*, **40**, 4734–4739, doi: 10.1002/grl.50880.

Barton, N. P., S. A. Klein, J. S. Boyle, and Y. Y. Zhang, 2012: Arctic synoptic regimes: Comparing domain-wide Arctic cloud observations with CAM4 and CAM5 during similar dynamics. *Journal of Geophysical Research: Atmospheres*, **117 (15)**, 1–19, doi: 10.1029/2012JD017589.

Bluestein, H. B., 1993: *Synoptic-Dynamic Meteorology in Midlatitudes: Volume II Observation and Theory of Weather Systems*. Oxford University Press, New York.

Budikova, D., 2009: Role of Arctic sea ice in global atmospheric circulation: A review. *Global and Planetary Change*, **68 (3)**, 149–163, doi: 10.1016/j.gloplacha.2009.04.001.

Bussières, N. and W. Hogg, 1989: The objective analysis of daily rainfall by distance weighting schemes on a Mesoscale grid. *Atmosphere-Ocean*, **27 (3)**, 521–541.

Cassano, E. N., A. H. Lynch, J. J. Cassano, and M. R. Koslow, 2006a: Classification of synoptic patterns in the western Arctic associated with extreme events at Barrow , Alaska , USA. *Climate Research*, **30 (2)**, 83–97.

Cassano, J. J., P. Uotila, and A. Lynch, 2006b: Changes in synoptic weather patterns in the polar regions in the twentieth and twenty-first centuries, part 1: Arctic. *International Journal of Climatology*, **26 (8)**, 1027–1049, doi: 10.1002/joc.1306.

Cavazos, T., 2000: Using Self-Organizing Maps to Investigate Extreme Climate Events : An Application to Wintertime Precipitation in the Balkans. *Journal of Climate*, **13**, 1718–1732.

Chen, C.-T. and T. Knutson, 2008a: On the Verification and Comparison of Extreme Rainfall Indices from Climate Models. *Journal of Climate*, **21 (7)**, 1605–1621, doi: 10.1175/2007JCLI1494.1.

Chen, C.-T. and T. Knutson, 2008b: On the Verification and Comparison of Extreme Rainfall Indices from Climate Models. *Journal of Climate*, **21 (7)**, 1605–1621, doi: 10.1175/2007JCLI1494.1.

Chen, M., R. Dickinson, Z. Xubin, and A. Hahmann, 1996: Comparison of Precipitation Observed over the Continental United States to That Simulated by a Climate Model. *Journal of Climate*, **9**, 2233–2249.

Chen, M., W. Shi, P. Xie, V. B. S. Silva, V. E. Kousky, R. Wayne Higgins, and J. E. Janowiak, 2008: Assessing objective techniques for gauge-based analyses of global daily precipitation. *Journal of Geophysical Research*, **113 (D4)**, doi: 10.1029/2007JD009132.

Cherry, J. E., L.-B. Tremblay, M. Stieglitz, G. Gong, and S. J. Déry, 2007: Development of the Pan-Arctic Snowfall Reconstruction: New Land-Based Solid Precipitation Estimates for 1940–99. *Journal of Hydrometeorology*, **8 (6)**, 1243–1263, doi: 10.1175/2007JHM765.1.

Cohen, J., et al., 2014: Recent Arctic amplification and extreme mid-latitude weather. *Nature Geoscience*, **7 (9)**, 627–637, doi: 10.1038/ngeo2234.

Collins, M., et al., 2013: Long-term Climate Change: Projections, Commitments and Irreversibility. *Climate Change 2013: The Physical Science Basis. Contribution of Working Group I to the Fifth Assessment Report of the Intergovernmental Panel on Climate Change*, 1029–1136.

Collins, W., et al., 2006: The Community Climate System Model Version 3 (CCSM3). *Journal of Climate*, **19**, 2122–2143.

Cressman, G., 1959: An Operational Objective Analysis System. *Monthly Weather Review*, **87 (10)**, 367–374, doi: 10.1126/science.27.693.594.

Curry, J., 1983: On the Formation of Continental Polar Air. *Journal of the Atmospheric Sciences*, **40**, 2278–2292, doi: 10.1175/1520-0469(1983)040<2278:OTFOCP>2.0.CO;2.

Dai, A., 2006: Precipitation Characteristics in Eighteen Coupled Climate Models. *Journal of Climate*, **19**, 4605–4630.

Dai, A., F. Giorgi, and K. E. Trenberth, 1999: Observed and model-simulated diurnal cycles of precipitation over the contiguous United States. *Journal of Geophysical Research*, **104**, 6377–6402.

Dai, A. and K. E. Trenberth, 2004: The Diurnal Cycle and Its Depiction in the Community Climate System Model. *Journal of Climate*, **17**, 930–951.

Daly, C., 2006: Guidelines for assessing the suitability of spatial climate data sets. *International Journal of Climatology*, **26 (6)**, 707–721, doi: 10.1002/joc.1322.

Daly, C., W. P. Gibson, G. H. Taylor, G. L. Johnson, and P. Pasteris, 2002: A knowledge-based approach to the statistical mapping of climate. *Climate Research*, **22**, 99–113.

De Boer, G., W. Chapman, J. E. Kay, B. Medeiros, M. D. Shupe, S. Vavrus, and J. Walsh, 2012: A characterization of the present-day arctic atmosphere in CCSM4. *Journal of Climate*, **25 (2005)**, 2676–2695, doi: 10.1175/JCLI-D-11-00228.1.

DeMott, C. A., D. A. Randall, and M. Khairoutdinov, 2007: Convective Precipitation Variability as a Tool for General Circulation Model Analysis. *Journal of Climate*, **20 (1)**, 91–112, doi: 10.1175/JCLI3991.1.

Deser, C., G. Magnusdottir, R. Saravanan, and A. Phillips, 2004: The Effects of North Atlantic SST and Sea Ice Anomalies on the Winter Circulation in CCM3. Part II: Direct and Indirect Components of the Response. *Journal of Climate*, **17 (5)**, 877–889, doi: 10.1175/1520-0442(2004)017<0877:TEONAS>2.0.CO;2.

Deser, C., R. Tomas, M. Alexander, and D. Lawrence, 2010: The Seasonal Atmospheric Response to Projected Arctic Sea Ice Loss in the Late Twenty-First Century. *Journal of Climate*, **23 (2)**, 333–351, doi: 10.1175/2009JCLI3053.1.

Deser, C., R. A. Tomas, and L. Sun, 2014: The role of ocean-atmosphere coupling in the zonal mean atmospheric response to Arctic sea ice loss. *Journal of Climate*, **3**, 141231092609 003, doi: 10.1175/JCLI-D-14-00325.1.

Deser, C., J. Walsh, and M. Timlin, 2000: Arctic Sea Ice Variability in the Context of Recent Atmospheric Circulation Trends. *journal of Climate*, **13**, 617–633.

Dirmeyer, P. A., et al., 2012: Simulating the diurnal cycle of rainfall in global climate models: resolution versus parameterization. *Climate Dynamics*, **39 (1-2)**, 399–418, doi: 10.1007/s00382-011-1127-9.

Drijfhout, S., G. J. van Oldenborgh, and A. Cimatoribus, 2012: Is a decline of AMOC causing the warming hole above the North Atlantic in observed and modeled warming patterns? *Journal of Climate*, **25**, 8373–8379, doi: 10.1175/JCLI-D-12-00490.1.

Emori, S., A. Hasegawa, R. Suzuki, and K. Dairaku, 2005: Validation, parameterization dependence, and future projection of daily precipitation simulated with a high-resolution atmospheric GCM. *Geophysical Research Letters*, **32 (6)**, doi: 10.1029/2004GL022306.

Ensor, L. A. and S. M. Robeson, 2008: Statistical Characteristics of Daily Precipitation: Comparisons of Gridded and Point Datasets. *Journal of Applied Meteorology and Climatology*, **47 (9)**, 2468–2476, doi: 10.1175/2008JAMC1757.1.

Francis, J. and S. Vavrus, 2012: Evidence linking Arctic amplification to extreme weather in mid-latitudes. *Geophysical Research Letters*, **39 (6)**, 1–6, doi: 10.1029/2012GL051000.

Fritsch, J. M., R. J. Kane, and C. R. Chelius, 1986: The Contribution of Mesoscale Convective Weather System to the Warm-Season Precipitation in the United States. *Journal of Climate and Applied Meteorology*, **25**, 1333–1345.

Fyfe, J. C., G. J. Boer, and G. M. Flato, 1999: The Arctic and Antarctic Oscillations and their Projected Changes Under Global Warming. *Geophysical Research Letters*, **26 (11)**, 1601–1604.

Gandin, L., 1965: Objective analysis of meteorological fields. *Israel Program for Scientific Translations*, 242pp.

Gent, P. R., S. G. Yeager, R. B. Neale, S. Levis, and D. a. Bailey, 2010: Improvements in a half degree atmosphere/land version of the CCSM. *Climate Dynamics*, **34 (6)**, 819–833, doi: 10.1007/s00382-009-0614-8.

Gent, P. R., et al., 2011: The Community Climate System Model Version 4. *Journal of Climate*, **24 (19)**, 4973–4991, doi: 10.1175/2011JCLI4083.1.

Gervais, M., J. R. Gyakum, E. Atallah, L. B. Tremblay, and R. B. Neale, 2014a: How Well Are the Distribution and Extreme Values of Daily Precipitation over North America Represented in the Community Climate System Model? A Comparison to Reanalysis, Satellite, and Gridded Station Data. *Journal of Climate*, **27 (14)**, 5219–5239, doi: 10.1175/JCLI-D-13-00320.1.

Gervais, M., L. B. Tremblay, J. R. Gyakum, and E. Atallah, 2014b: Representing Extremes in a Daily Gridded Precipitation Analysis over the United States: Impacts of Station Density, Resolution, and Gridding Methods. *Journal of Climate*, **27 (14)**, 5201–5218, doi: 10.1175/JCLI-D-13-00319.1.

Gillett, N. P., 2002: How linear is the Arctic Oscillation response to greenhouse gases? *Journal of Geophysical Research*, **107**, 1–7, doi: 10.1029/2001JD000589.

Gober, M., E. Zsoter, and D. Richardson, 2008: Could a perfect model ever satisfy a naive forecaster? On grid box mean versus point verification. *Meteorological Application*, **15**, 359–365, doi: 10.1002/met.

Goodison, B., P. Louis, and D. Yang, 1998: Report No. 67 WMO Solide Precipitation Measurement Intercomparison. Tech. Rep. 67, World Meteorological Association.

Gornall, J., R. Betts, E. Burke, R. Clark, J. Camp, K. Willett, and A. Wiltshire, 2010: Implications of climate change for agricultural productivity in the early twenty-first century. *Philosophical transactions of the Royal Society of London. Series B, Biological sciences*, **365 (1554)**, 2973–89, doi: 10.1098/rstb.2010.0158.

Graversen, R., P. Langen, and T. Mauritsen, 2014: Polar Amplification in CCSM4: Contributions from the Lapse Rate and Surface Albedo Feedbacks. *Journal of Climate*, 4433–4450, doi: 10.1175/JCLI-D-13-00551.1.

Groisman, P., R. Knight, D. Easterling, T. Karl, G. Hegerl, and V. Razuvaev, 2005: Trends in Intense Precipitation in the Climate Record. *Journal of Climate*, **18**, 1326–1350.

Hewitson, B. and R. Crane, 2005: Gridded Area-Averaged Daily Precipitation via Conditional Interpolation. *Journal of Climate*, **41**, 41–57.

Hewitson, B. C. and R. G. Crane, 2002: Self-organizing maps: applications to synoptic climatology. *Climate Research*, **22**, 13–26.

Hofstra, N. and M. New, 2009: Spatial variability in correlation decay distance and influence on angular-distance weighting interpolation of daily precipitation over Europe. *International Journal of Climatology*, **29**, 1872–1880, doi: 10.1002/joc.

Hofstra, N., M. New, and C. McSweeney, 2010: The influence of interpolation and station network density on the distributions and trends of climate variables in gridded daily data. *Climate Dynamics*, **35 (5)**, 841–858, doi: 10.1007/s00382-009-0698-1.

Holland, M. M. and C. M. Bitz, 2003: Polar amplification of climate change in coupled models. *Climate Dynamics*, **21 (March)**, 221–232, doi: 10.1007/s00382-003-0332-6.

Holton, J., 2004: *An Introduction to Dynamic Meteorology*. 4th ed., Elsevier Inc., San Diego.

Honda, M., K. Yamazaki, H. Nakamura, and K. Takeuchi, 1999: Dynamic and Thermodynamic Characteristics of Atmospheric Response to Anomalous Sea-Ice Extent in the Sea of Okhotsk. *Journal of Climate*, **12**, 3347–3358.

Huffman, G., R. Adler, M. Morrisey, D. Bolvin, S. Curtis, R. Joyce, B. McGavock, and J. Susskind, 2001: Global Precipitation at One-Degree Daily Resolution from Multisatellite Observations. *Journal of Hydrometeorology*, **37**, 36–50.

Huffman, G., et al., 1997: The Global Precipitation Climatology Project (GPCP) Combined Precipitation Dataset. *Bulletin of the American Meteorological Society*, **78 (1)**, 5–20.

Huffman, G. J., et al., 2007: The TRMM Multisatellite Precipitation Analysis (TMPA): Quasi-Global, Multiyear, Combined-Sensor Precipitation Estimates at Fine Scales. *Journal of Hydrometeorology*, **8 (1)**, 38–55, doi: 10.1175/JHM560.1.

Hurrell, J. W., et al., 2013: The community earth system model: A framework for collaborative research. *Bulletin of the American Meteorological Society*, **94 (November 2012)**, 1339–1360, doi: 10.1175/BAMS-D-12-00121.1.

Hutchinson, M. F., 1995: Interpolating mean rainfall using thin plate smoothing splines. *International journal of geographical information systems*, **9 (4)**, 385–403, doi: 10.1080/02693799508902045.

Hutchinson, M. F., D. W. McKenney, K. Lawrence, J. H. Pedlar, R. F. Hopkinson, E. Milewska, and P. Papadopol, 2009: Development and Testing of Canada-Wide Interpolated Spatial Models of Daily Minimum–Maximum Temperature and Precipitation for 1961–2003. *Journal of Applied Meteorology and Climatology*, **48 (4)**, 725–741, doi: 10.1175/2008JAMC1979.1.

Huth, R., C. Beck, A. Philipp, M. Demuzere, Z. Ustrnul, M. Cahynová, J. Kyselý, and O. E. Tveito, 2008: Classifications of atmospheric circulation patterns: recent advances and applications. *Annals of the New York Academy of Sciences*, **1146**, 105–52, doi: 10.1196/annals.1446.019.

Iorio, J., P. Duffy, B. Govindasamy, S. Thompson, M. Khairoutdinov, and D. Randall, 2004: Effects of model resolution and subgrid-scale physics on the simulation of precipitation in the continental United States. *Climate Dynamics*, **23 (3-4)**, 243–258, doi: 10.1007/s00382-004-0440-y.

Jahn, A., et al., 2012: Late-Twentieth-Century Simulation of Arctic Sea Ice and Ocean Properties in the CCSM4. *Journal of Climate*, **25 (5)**, 1431–1452, doi: 10.1175/JCLI-D-11-00201.1.

John, S., 1969: A Nonlinear Mapping for Data Structure Analysis. *IEEE Transactions on Computers*, **C-18 (5)**, 401–409.

Johnson, N. C., S. B. Feldstein, and B. Tremblay, 2008: The Continuum of Northern Hemisphere Teleconnection Patterns and a Description of the NAO Shift with the Use of Self-Organizing Maps. *Journal of Climate*, **21 (23)**, 6354–6371, doi: 10.1175/2008JCLI2380.1.

Jones, P., 1999: First- and Second-Order Conservative Remapping Schemes for Grids in Spherical Coordinates. *Monthly Weather Review*, **127**, 2204–2210.

Kay, J. E., M. M. Holland, C. M. Bitz, E. Blanchard-Wrigglesworth, A. Gettelman, A. Conley, and D. Bailey, 2012: The Influence of Local Feedbacks and Northward Heat Transport on the Equilibrium Arctic Climate Response to Increased Greenhouse Gas Forcing. *Journal of Climate*, **25 (16)**, 5433–5450, doi: 10.1175/JCLI-D-11-00622.1.

Kay, J. E., et al., 2014: The Community Earth System Model (CESM) Large Ensemble Project: A Community Research for Studying Climate Change in the Presence of Internal Climate Variability. *Bulletin of the American Meteorological Society*, **Early Online Release**, doi: doi: 10.1175/ BAMS-D-13-00255.

Knight, D. B. and R. E. Davis, 2007: Climatology of tropical cyclone rainfall in the southeastern united states. *Physical Geography*, **28 (2)**, 126–147.

Kohonen, T., 1982: Self-organized formation of topologically correct feature maps. *Biological Cybernetics*, **43**, 59–69, doi: 10.1007/BF00337288.

Kohonen, T., 2001: *Self-Organizing Maps Third Edition*. Springer.

Kursinski, A. L. and X. Zeng, 2006: Areal estimation of intensity and frequency of summertime precipitation over a midlatitude region. *Geophysical Research Letters*, **33 (22)**, 1–5, doi: 10.1029/2006GL027393.

Kvamstø, N. G., P. Skeie, and D. B. Stephenson, 2004: Impact of Labrador sea-ice extent on the North Atlantic oscillation. *International Journal of Climatology*, **24 (5)**, 603–612, doi: 10.1002/joc.1015.

Liu, J., J. A. Curry, H. Wang, M. Song, and R. M. Horton, 2012: Impact of declining Arctic sea ice on winter snowfall. *Proceedings of the National Academy of Sciences of the United States of America*, **109 (11)**, 4047–4079, doi: 10.1073/pnas.1114910109/-/DCSupplemental.www.pnas.org/cgi/doi/10.1073/pnas.1114910109.

Liu, Y., R. H. Weisberg, and C. N. K. Mooers, 2006: Performance evaluation of the self-organizing map for feature extraction. *Journal of Geophysical Research*, **111 (C5)**, C05 018, doi: 10.1029/2005JC003117.

Magnusdottir, G., C. Deser, and R. Saravanan, 2004: The Effects of North Atlantic SST and Sea Ice Anomalies on the Winter Circulation in CCM3. Part I: Main Features and Storm Track Characteristics of the Response. *Journal of Climate*, **17 (5)**, 857–876, doi: 10.1175/1520-0442(2004)017<0857:TEONAS>2.0.CO;2.

Manabe, S. and R. Wetherald, 1975: The effects of doubling the CO2 concentration on the climate of a general circulation model. *Journal of Atmospheric Sciences*, **32 (1)**, 3–15, doi: 10.1175/1520-0469(1975)032<0003:TEODTC>2.0.CO;2.

Massey, F., 1951: The Kolmogorov-Smirnov Test for Goodness of Fit. *Journal of American Statistical Association*, **46 (253)**, 68–78.

Menne, M. J., I. Durre, R. S. Vose, B. E. Gleason, and T. G. Houston, 2012: An Overview of the Global Historical Climatology Network-Daily Database. *Journal of Atmospheric and Oceanic Technology*, 120326124007003, doi: 10.1175/JTECH-D-11-00103.1.

Murtagh, F. and M. Hernández-Pajares, 1995: The Kohonen self-organizing map method: An assessment. *Journal of Classification*, **12 (2)**, 165–190, doi: 10.1007/BF03040854.

Neale, R. B., C.-c. Chen, P. H. Lauritzen, D. L. Williamson, A. J. Conley, A. K. Smith, M. Mills, and H. Morrison, 2010: Description of the NCAR Community Atmosphere Model (CAM 5 . 0). Tech. rep., National Center for Atmospheric Research, 283 pp.

Neale, R. B., J. Richter, S. Park, P. H. Lauritzen, S. Vavrus, P. J. Rasch, and M. Zhang, 2013: The Mean Climate of the Community Atmosphere Model (CAM4) in Forced SST and Fully Coupled Experiments. *Journal of Climate*, **26 (14)**, 5150–5168, doi: 10.1175/JCLI-D-12-00236.1.

Osborn, T. J. and M. Hulme, 1997: Development of a Relationship between Station and Grid-Box Rainday Frequencies for Climate Model Evaluation. *Journal of Climate*, **10**, 1885–1908.

Petoukhov, V. and V. A. Semenov, 2010: A link between reduced Barents-Kara sea ice and cold winter extremes over northern continents. *Journal of Geophysical Research*, **115 (D21)**, D21 111, doi: 10.1029/2009JD013568.

Pithan, F. and T. Mauritsen, 2014: Arctic amplification dominated by temperature feedbacks in contemporary climate models. *Nature Geoscience*, **7 (February)**, 181–184, doi: 10.1038/NGEO2071.

Pritchard, M. S., M. W. Moncrieff, and R. C. J. Somerville, 2011: Orogenic Propagating Precipitation Systems over the United States in a Global Climate Model with Embedded Explicit Convection. *Journal of the Atmospheric Sciences*, **68 (8)**, 1821–1840, doi: 10.1175/2011JAS3699.1.

Rahmstorf, S., J. E. Box, G. Feulner, M. E. Mann, A. Robinson, S. Rutherford, and E. J. Schaffernicht, 2015: Exceptional twentieth-century slowdown in Atlantic Ocean overturning circulation. *Nature Climate Change*, **5 (May)**, 1–6, doi: 10.1038/nclimate2554.

Reusch, D. B., R. B. Alley, and B. C. Hewitson, 2005: Relative Performance of Self-Organizing Maps and Principal Component Analysis in Pattern Extraction from Synthetic Climatological Data. *Polar Geography*, **29 (3)**, 188–212, doi: 10.1080/789610199.

Reusch, D. B., R. B. Alley, and B. C. Hewitson, 2007: North Atlantic climate variability from a self-organizing map perspective. *Journal of Geophysical Research*, **112 (D2)**, D02 104, doi: 10.1029/2006JD007460.

Rosenzweig, C., F. N. Tubiello, R. Goldberg, E. Mills, and J. Bloomfield, 2002: Increased crop damage in the US from excess precipitation under climate change. *Global Environmental Change*, **12 (3)**, 197–202, doi: 10.1016/S0959-3780(02)00008-0.

Saha, S., et al., 2010: The NCEP Climate Forecast System Reanalysis. *Bulletin of the American Meteorological Society*, **91 (8)**, 1015–1057, doi: 10.1175/2010Bams3001.1.

Schuenemann, K. C. and J. J. Cassano, 2009: Changes in synoptic weather patterns and Greenland precipitation in the 20th and 21st centuries: 1. Evaluation of late 20th century simulations from IPCC models. *Journal of Geophysical Research*, **114 (D20)**, D20 113, doi: 10.1029/2009JD011705.

Schuenemann, K. C. and J. J. Cassano, 2010: Changes in synoptic weather patterns and Greenland precipitation in the 20th and 21st centuries: 2. Analysis of 21st century atmospheric changes using self-organizing maps. *Journal of Geophysical Research*, **115 (D5)**, D05 108, doi: 10.1029/2009JD011706.

Scoccimarro, E., S. Gualdi, A. Bellucci, M. Zampieri, and A. Navarra, 2013: Heavy precipitation events in a warmer climate: results from CMIP5 models. *Journal of Climate*, 130626130626007, doi: 10.1175/JCLI-D-12-00850.1.

Screen, J. and I. Simmonds, 2010: The central role of diminishing sea ice in recent Arctic temperature amplification. *Nature*, **464 (7293)**, 1334–1337, doi: 10.1038/nature09051.

Screen, J., I. Simmonds, C. Deser, and R. Tomas, 2013: The Atmospheric Response to Three Decades of Observed Arctic Sea Ice Loss. *Journal of Climate*, **26 (4)**, 1230–1248, doi: 10.1175/JCLI-D-12-00063.1.

Seierstad, I. A. and J. Bader, 2008: Impact of a projected future Arctic Sea Ice reduction on extratropical storminess and the NAO. *Climate Dynamics*, **33 (7-8)**, 937–943, doi: 10.1007/s00382-008-0463-x.

Serreze, M. C., A. P. Barrett, J. C. Stroeve, D. N. Kindig, and M. M. Holland, 2009: The emergence of surface-based Arctic amplification. *The Cryosphere Discussions*, **2**, 601–622, doi: 10.5194/tcd-2-601-2008.

Shepard, D., 1968: A two-dimensional interpolation function for irregularly-spaced data. *Proceedings of the 1968 23rd ACM national conference*, 517–524, doi: 10.1145/800186.810616.

Shiu, C.-J., S. C. Liu, C. Fu, A. Dai, and Y. Sun, 2012: How much do precipitation extremes change in a warming climate? *Geophysical Research Letters*, **39 (17)**, L17 707, doi: 10.1029/2012GL052762.

Sillmann, J., V. V. Kharin, X. Zhang, F. W. Zwiers, and D. Bronaugh, 2013: Climate extremes indices in the CMIP5 multimodel ensemble: Part 1. Model evaluation in the present climate. *Journal of Geophysical Research: Atmospheres*, **118 (4)**, 1716–1733, doi: 10.1002/jgrd.50203.

Singarayer, J., J. Bambier, and P. Valdes, 2006: Twenty-First-Century Climate Impacts from a Declining Arctic Sea Ice Cover. *Journal of Climate*, **19**, 1109–1125.

Stephens, M. A., 1970: Use of the Kolmogorov-Smirnov, Cramer-Von Mises and Related Statistics Without Extensive Tables. *Journal of the Royal Statistical Society. Series B. (Methodological)*, **32 (1)**, 115–122.

Sun, X. and A. P. Barros, 2010: An Evaluation of the Statistics of Rainfall Extremes in Rain Gauge Observations, and Satellite-Based and Reanalysis Products Using Universal Multifractals. *Journal of Hydrometeorology*, **11 (2)**, 388–404, doi: 10.1175/2009JHM1142.1.

Sun, Y., S. Solomon, A. Dai, and R. Portmann, 2006: How Often Does It Rain? *Journal of Climate*, **19 (1996)**, 916–934.

Sun, Y., S. Solomon, A. Dai, and R. W. Portmann, 2007: How Often Will It Rain? *Journal of Climate*, **20 (19)**, 4801–4818, doi: 10.1175/JCLI4263.1.

Susskind, J., P. Piraino, L. Rokke, L. Iredell, and A. Mehta, 1997: Characteristics of the TOVS Pathfinder Path A Dataset. *Bulletin of the American Meteorological Society*, **78 (7)**, 1449–1472.

Thompson, D. W. J. and J. M. Wallace, 1998: The Arctic oscillation signature in the wintertime geopotential height and temperature fields. *Geophysical Research Letters*, **25 (9)**, 1297, doi: 10.1029/98GL00950.

Ting, M., Y. Kushnir, and C. Li, 2014: North Atlantic Multidecadal SST Oscillation: External forcing versus internal variability. *Journal of Marine Systems*, **133**, 27–38, doi: 10.1016/j.jmarsys.2013.07.006.

Tremblay, L., 2001: Can we consider the Arctic Oscillation independently from the Barents Oscillation? *Geophysical Research Letters*, **0 (0)**, 0–0.

Trenberth, K. E., A. Dai, R. M. Rasmussen, and D. B. Parsons, 2003: The Changing Character of Precipitation. *Bulletin of the American Meteorological Society*, **84 (9)**, 1205–1217, doi: 10.1175/BAMS-84-9-1205.

Tustison, B., D. Harris, and E. Foufoula-Georgiou, 2001: Scale Issues in Verification of Precipitation Forecasts. *Journal of Geophysical Research*, **106 (Dll)**, 11 775–11 784.

Vesanto, J., J. Himberg, E. Alhoniemi, and J. Parhankangas, 2000: SOM Toolbox for Matlab 5. Tech. Rep. 0, Helsinki Univiversity of Technology, Helsinki, Finland.

Walsh, J. E., A. S. Phillips, D. H. Portis, and W. L. Chapman, 2001: Extreme cold outbreaks in the United States and Europe, 1948-99. *Journal of Climate*, **14 (1987)**, 2642–2658, doi: 10.1175/1520-0442(2001)014<2642:ECOITU>2.0.CO;2.

Wang, M. and J. E. Overland, 2012: A sea ice free summer Arctic within 30 years: An update from CMIP5 models. *Geophysical Research Letters*, **39 (18)**, n/a–n/a, doi: 10.1029/2012GL052868.

Wilks, D., 2006: *Statistical Methods in the Atmospheric Sciences*. 2d ed., Academic Press, 56 pp.

Woollings, T., J. Gregory, J. Pinto, M. Reyers, and D. Brayshaw, 2012: Response of the North Atlantic storm track to climate change shaped by ocean–atmosphere coupling. *Nature Geoscience*, **5 (5)**, 313–317, doi: 10.1038/ngeo1438.

Xie, P., M. Chen, S. Yang, A. Yatagai, T. Hayasaka, Y. Fukushima, and C. Liu, 2007: A Gauge-Based Analysis of Daily Precipitation over East Asia. *Journal of Hydrometeorology*, **8 (3)**, 607–626, doi: 10.1175/JHM583.1.

Xie, P., J. Janowiak, P. Arkin, R. Adler, A. Gruber, R. Ferraro, G. J. Huffman, and S. Curtis, 2003: GPCP Pentad Precipitation Analyses : An Experimental Dataset Based on Gauge Observations and Satellite Estimates. *Journal of Climate*, **16**, 2197–2214.

Zhang, G. J. and N. A. Mcfarlane, 1995: Sensitivity of climate simulations to the parameterization of cumulus convection in the Canadian climate centre general circulation model. *Atmosphere-Ocean*, **33 (3)**, 407–446.